

Alma Mater Studiorum – Università di Bologna

DOTTORATO DI RICERCA IN
MECCANICA E SCIENZE AVANZATE DELL'INGEGNERIA

Ciclo XXXIII

Settore Concorsuale: 09/A1 Ingegneria Aeronautica, Aerospaziale e Navale

Settore Scientifico Disciplinare: ING-IND/05 Impianti e Sistemi Aerospaziali

Development of a ground testing facility and attitude control for magnetically actuated nanosatellites

Presentata da: Anton Bahu

Coordinatore Dottorato

Prof. Marco Carricato

Supervisore

Prof. Paolo Tortora

Co-Supervisore

Prof. Dario Modenini

Esame finale anno 2021

Abstract

Growing popularity of the highly capable small- and nano-satellites, driven by components miniaturization, face new technological challenges and at the same time provides new opportunities for the whole space sector. Low cost of nanosatellites launches make them accessible. Reliability is an exigency: especially challenging is design and testing of Attitude and Determination Control Systems (ADCS). Demand for nanosatellites-dedicated attitude control algorithms and careful performance assessment of the spacecrafts motivates the research work presented in this thesis.

In the first part of the manuscript, development and assessment of the three degrees-of-freedom ADCS testbed for nanosatellites testing is described. The facility was developed within the Microsatellites and Space Microsystems Lab at University of Bologna, and designed to meet strict low-cost requirements. The facility includes several integrated subsystems to simulate the on-orbit environment: i) an air-bearing based, three degree of freedom platform with automatic balancing system, ii) a Helmholtz , iii) a Sun simulator, and iv) a metrology vision system . Experimental assessment of the subsystems guarantee necessary level of performance.

Control law design for smallsats is addressed in the second part. Limited power availability and reliability makes magnetic actuation particularly suited for ADCS design, but, the control system faces inherent underactuation. To overcome the intrinsic limits of existing control designs, a novel approach to the three-axis attitude control of a magnetically actuated spacecrafts is proposed, based on hybrid systems theory. A local H-inf regulator with guaranteed performance and a global nonlinear controller used for ensuring global stability and robustness, are combined. Hybrid control theory is employed to develop a mixed continuous-discrete controller able to switch between different feedbacks. Analytical results are verified by means of realistic numerical simulations: errors on the state comply with the computed bounds and stability is guaranteed.

Acknowledgments

I express my sincere thanks to professor Paolo Tortora for his support and the possibility he gave me three years ago. Without him the work described in this thesis would never be possible.

I would like to express my sincere gratitude to professor Dario Modenini, for his constant support and teaching. Countless hours spent to guide me through the research challenges, encouragement and mentorship provided in last three years, made me a better engineer and person.

Grazie ai colleghi e amici, soprattutto ad Alessandro per le sue consultazioni, che mi hanno supportato e mi sono stati vicini.

Grazie a te Eleonora, per esserci, per credere in me e in quello che faccio.

Большое спасибо семье - маме, папе и сестре - за вашу поддержку и любовь.

Contents

Abstract	iii
Acknowledgements	iv
Contents	vi
List of Tables	x
List of Figures	xii
List of Acronyms	xv
List of Symbols	xvi
I Introduction	1
1 Introduction	3
1.1 ADCS ground testing	6
1.1.1 Dynamic simulators	7
1.1.2 Nanosatellites testing facilities	8
1.1.3 Facility verification	12
1.1.4 The Dynamic Testbed for CubeSats facility at University of Bologna	13
1.1.5 Objectives and contributions	15
1.2 Nanosatellites attitude control	16
1.2.1 Magnetic attitude control techniques	17
1.2.2 Uniting control problem	18
1.2.3 Objectives and contributions	19
1.3 Outline	20
2 Preliminaries	21
2.1 Notation and reference frames	22

2.1.1	Coordinate reference frames	22
2.2	Rigid body kinematics and dynamics	23
2.2.1	Attitude representation	23
2.2.2	Rotational kinematics	25
2.2.3	Rigid body dynamics	26
2.3	Model of a rotating platform with integrated balancing system	27
2.4	Dynamical model of the magnetically actuated spacecraft	29
2.4.1	Linearized model	29
2.4.2	Controllability of the nonlinear dynamics and of the linearized dynamics	30
2.5	Control theory preliminaries	31
2.5.1	Stability notions	31
2.5.2	LTP systems and Floquet Stability Theory	33
2.6	Modeling hybrid systems	34
2.7	On-orbit environment	36
2.7.1	Magnetic field model	37
2.7.2	Disturbance torques	37
II	Ground testing facility	41
3	Facility design and overview	43
3.1	Helmholtz cage	47
3.1.1	Verification process	47
3.2	Sun simulator	47
3.2.1	Optimization and verification process	49
3.3	Ground truth vision system	49
3.4	Testbed platform	50
3.4.1	Platform and mass balancing system sizing	51
3.4.2	3U Platform design	53
3.4.3	1U Platform design	55
3.4.4	Automatic mass Balancing System hardware	56
3.5	Discussion	58
4	Automatic mass balancing	59
4.1	Dynamic model and simulations environment	60

4.2	In-plane balancing	61
4.2.1	Decoupled dynamics and linear control law	62
4.2.2	Nonlinear control law for planar balancing	63
4.2.3	Numerical simulations	65
4.3	Estimation of vertical offset and system inertia	73
4.3.1	Batch estimation	73
4.3.2	Numerical simulations	75
4.4	Disturbance estimation	79
4.5	Experimental verification	81
4.5.1	Platform balancing	81
4.5.2	Experimental residual disturbance estimation	84
4.6	Magnetic detumbling	86
4.7	Discussion	87
 III Nanosatellites attitude control		89
 5 Attitude stabilization of a magnetically actuated spacecraft		91
5.1	Magnetically actuated spacecraft model in a hybrid framework	92
5.2	Attitude stabilization control problem	93
5.3	Local linear control law	94
5.4	Global nonlinear control law	96
5.4.1	Averaging of the nonlinear systems	96
5.4.2	Nonlinear averaged controller	98
5.4.3	Hybrid nonlinear averaged controller	99
5.4.4	ISS of the averaged non-linear dynamics	101
5.5	Hybrid supervisor design	102
5.6	Simulations of hybrid magnetic attitude control law	105
5.7	Discussion	110
 6 Conclusions and Perspectives		113
 Bibliography		116

List of Tables

1.1	ADCS testing facilities overview	14
3.1	Disturbance torques in ground testing facilities	46
3.2	3U platform ABS design parameters	55
3.3	1U platform ABS design parameters	56
3.4	IMU characteristics	57
4.1	Controllers gains	67
4.2	Convergence history of the parameters identification step.	84
5.1	Simulation parameters	107

List of Figures

1.1	UWE-4 CubeSat exploded view (Kramer et al., 2020)	5
1.2	Share of small sats by use (Bok et al., 2020)	6
1.3	From top to bottom: tabletop, umbrella and dumbbell air bearing platform setup (Schwartz et al., 2003).	9
1.4	Nanosatellites testing facilities.	11
3.1	DTC Facility.	44
3.2	Theia ESAT : 1U educational CubeSat (Space, 2020).	45
3.3	Detailed view of Sun simulator with collimation device.	49
3.4	Balancing system reference frame (Bahu and Modenini, 2020).	52
3.5	3U Platform.	54
3.6	1U Platform.	56
4.1	Step response of the closed loop linear system.	66
4.2	Plane balancing simulations with ideal measurements	69
4.3	Mechanical nonlinearities.	70
4.4	Simulations of plane balancing for 3U platform	71
4.5	Plane balancing of 3U platform with high gains.	72
4.6	3U parameters LSQ estimation comparison.	77
4.7	1U parameters estimation by LSQ-SGF	77
4.8	Numerical simulation of the $r_{CM,z}$ estimation by constrained LSQ.	79
4.9	Numerical simulation of the residual disturbance estimation after balancing (Bahu and Modenini, 2020).	80
4.10	3U parameters experimental estimation.	82
4.11	1U parameters experimental estimation.	83
4.12	Iterative balancing procedure (Bahu and Modenini, 2020).	84
4.13	Kinetic energy variation of the balanced platform Bahu and Modenini (2020);	85
4.14	Balancing effectiveness evaluation.	86
4.15	Experimental detumbling.	88

5.1	Logical hysteresis switching	100
5.2	Supervisory control closed loop system.	103
5.3	Disturbance-free case (a) attitude (b) reduced state norm	108
5.4	Attitude evolution of the spacecraft in case of disturbances	108
5.5	Comparison of reduced state norm of the spacecraft in case of distur- bances for different controllers	109
5.6	Control dipole moments	109
5.7	Pointing errors with random aerodynamic center and solar pressure center	111

List of Acronyms

ADCS	Attitude and Determination Control System
ACS	Attitude Control System
ISS	International Space Station
SOC	Socket on the Chip
COTS	Component of the Shelf
IMU	Inertial Measurement Unit
MEMS	Micro Electro-Mechanical Systems
SIL	Software in the Loop
HIL	Hardware in the Loop
CM	Center of Mass
CR	Center of Rotation
DoF	Degrees of Freedom
ABS	Automatic Balancing System
DTC	Dynamic Testbed for CubeSats
ECI	Earth-Centered Inertial
IGRF	International Geomagnetic Reference Field
LTI	Linear Time Invariant
LTV	Linear Time Variant
LTP	Linear Time Periodic
LQR	Linear Quadratic Regulator
PID	Proportional Integral Derivative
EMP	Exponentially Modulated Periodic
HTF	Harmonic Transfer Function
GAS	Global Asymptotic Stability

List of Symbols

\mathbb{R}	set of real numbers
\mathbb{R}_+	set of non negative real numbers
\mathbb{R}_+^*	set of strictly positive real numbers
\mathbb{N}	set of natural numbers zero included
\mathbb{Z}	set of integer numbers
\emptyset	the empty set
$\mathbf{0}_{n \times m}$	matrix of dimension $n \times m$ whose entries are all zeros
\mathbb{I}_n	n -dimensional identity matrix.
$SO(3)$	the special orthogonal group of order three $A \in SO(3) \equiv A \in \mathbb{R}^{3 \times 3}, \det(A) = 1, A^T A = A A^T = \mathbb{I}_3$
$\text{blkdiag}(A_1, \dots, A_n)$	block-diagonal matrix block diagonal elements the square matrices A_1, \dots, A_n
$f : A \rightarrow B$	a function from A to B
$f : A \rightrightarrows B$	a set-valued function from A to B
$f \in \mathcal{K}$	f is a class- \mathcal{K} function, i.e. $f : [0, a) \rightarrow \mathbb{R}_+$ ($a \in \mathbb{R}_+^*$) is continuous, strictly increasing and $f(0) = 0$
$f \in \mathcal{K}_\infty$	f is a class- \mathcal{K}_∞ function, i.e. $f \in \mathcal{K}$ and $f(x) \rightarrow_{x \rightarrow a} \infty$
$f \in \mathcal{L}$	f is a class- \mathcal{L} function, i.e. $f : \mathbb{R}_+ \rightarrow \mathbb{R}_+$ is continuous, strictly decreasing and $f(x) \rightarrow_{x \rightarrow \infty} = 0$
$\beta \in \mathcal{KL}$	β is a class- \mathcal{KL} function, i.e. $\beta(\cdot, t) \in \mathcal{K}$ for each t and $\beta(s, \cdot) \in \mathcal{L}$ for each s
m_{tot}	Total satellite mass [kg]
$m_{payload}$	Payload mass [kg]
m_{ABS}	Automatic mass balancing system mass [kg]
m_{st}	Platform mass [kg]
m_b	Mass of the counterweight [kg]
J	Body inertia matrix [kg/m^2]
\mathbf{r}_{CM}	Center of mass position vector [m]
\mathbf{r}_{CR}	Center of rotation position vector [m]

\mathbf{r}_{off}	CM to CR distance [m]
\mathbf{r}_b	Balance mass position vector [m]
\mathbf{g}	Gravity vector [m/s^2]
\mathbf{b}	Magnetic field [T]
R_{gb}	Distance from earth center [m]
ρ	Atmospheric air density [$\frac{kg}{m^3}$]
μ	Gravitational constant $6.67 \cdot 10^{-11} Nm^2/kg^2$
T_{orb}	Orbital period [s]
\mathbf{m}_{res}	Residual magnetic dipole [Am^2]
\mathbf{F}_{aero}	Aerodynamic force vector [N]
A_{sf}	Surface of area facing the flow [m^2]
C_D	Drag coefficient
v_0	Satellite orbital speed [m/s^2]
P_{sol}	Solar radiation [N/m^2]
C_{RP}	Coefficient of reflectivity
\mathcal{F}_i	Inertial reference frame
\mathcal{F}_b	Body reference frame
$\boldsymbol{\theta} = [\phi \ \theta \ \psi]^T$	Vector of RPY euler angles [rad]
R	DCM matrix between \mathcal{F}_i and \mathcal{F}_b
\mathbf{q}	Vector of euler parameters
$\boldsymbol{\omega}$	Vector of angular speed [rad/s]
$\boldsymbol{\tau}$	Torque vector [Nm]
\mathbf{m}_c	Control magnetic dipole [Am^2]
c_{aero}	Aerodynamic center [m]
c_{srp}	Solar radiation pressure center [m]

Part I

Introduction

1

Introduction

The twenty-first century saw the opening of a new era of the space race thanks to commercial rocket launches, substantial reduction of the cost to LEO (Jones, 2018) and renewed interest of industry companies such as SpaceX, OneWeb, Telesat, Amazon, Boeing in providing broadband satellite internet, disaster prevention services, earth monitoring, disaster prevention services. The sector growth is driven by new technological developments: perhaps the most notable is the miniaturization of electronic devices.

Dimension reduction of satellite hardware components, such as thrusters, attitude control systems, batteries, antennas, sensors and payloads, paved the way to highly capable small satellites. With size and weight being only a fraction of conventional satellites, the growing success of small satellites is due primary to low deployment cost and short development time (Gregorio and Alimenti, 2019). Smallsats first became popular in the academia, where keeping their development, launch, and operation costs as low as possible was the main requirement. This was achieved mainly through components standardization (Villela et al., 2019). Popularity of small satellites led to the development of standard launchers and platforms, further reducing the costs (Crisp et al., 2015): space became closer and more accessible to smaller companies and institutions.

Small satellites can be classified according to their weight:

- femto-satellites: less than 0.1 kg

-
- pico-satellites: 0.1-1 kg
 - nano-satellites: 1 - 10 kg
 - micro-satellites: 10-100 kg
 - mini-satellites: 100-1000 kg

as well as by form-factor. CubeSat standard, proposed in 1999 by Jordi Puig-Suari and Bob Twiggs for educational purposes (Puig-suari et al., 2001), emerged as the most popular one: more than 65% of all launched small satellites belong to this class (Bok et al., 2020); the share is 90% if only nano-satellites are considered (Kulu, 2020). 1U is the basic unit for the CubeSat satellite, defined as 10 cm × 10 cm × 10 cm cube of 1.33 kg: see Figure 1.1 for the exploded view of a 1U CubeSat. The cubic form was chosen to guarantee easy integration and sufficient surface area for solar power generation, while providing better space-thermal stability. Designed to cost less than 1000 \$ (Saeed et al., 2020), now it can be build by using entirely off-the-shelf commercial components (Davoli et al., 2019). Due to the small dimensions and standardized deployers (originally proposed P-POD and equivalent interfaces such as ISIPOD, NLAS, T-POD, see Swartwout (2013)), large number of satellites can be placed on the same launcher. Moreover, International Space Station (ISS) is intensively used for CubeSats launches.

Starting from the 1U design, CubeSats of different sizes have been proposed (from 0.25U to 16U). Thanks to the low cost, CubeSats became popular for both commercial and scientific tasks. Choosing a CubeSat as target platform shorten the sketch to prototype time, hence developers can focus on payload integration and scientific mission. The number of launches is growing even faster than expected (Villela et al., 2019), with more than 1200 CubeSats launched over past 20 years (Kulu, 2020; Villela et al., 2019; Bok et al., 2020). Multi-satellite mission are of growing importance, with ongoing investigation on the use of CubeSat constellations to provide global connectivity, see surveys in Gregorio and Alimenti (2019) and Saeed et al. (2020). Meanwhile, formation-flying missions, where the satellites are controlled by a common control law, are employed mainly for earth observation and technological demonstration (Bandyopadhyay et al., 2015).

Socket-on-the-chip (SoC) approach allows extreme miniaturization at relatively low price thanks to adoption of up-to-date COTS components, but have a drawback: no or limited flight heritage. In fact, CubeSats missions have a high failure rate of 25 % (Villela et al., 2019), with even higher failure rate for technology demonstration missions with 46 % (as provided by Polat et al. in 2016, the statistics are continuously updating).

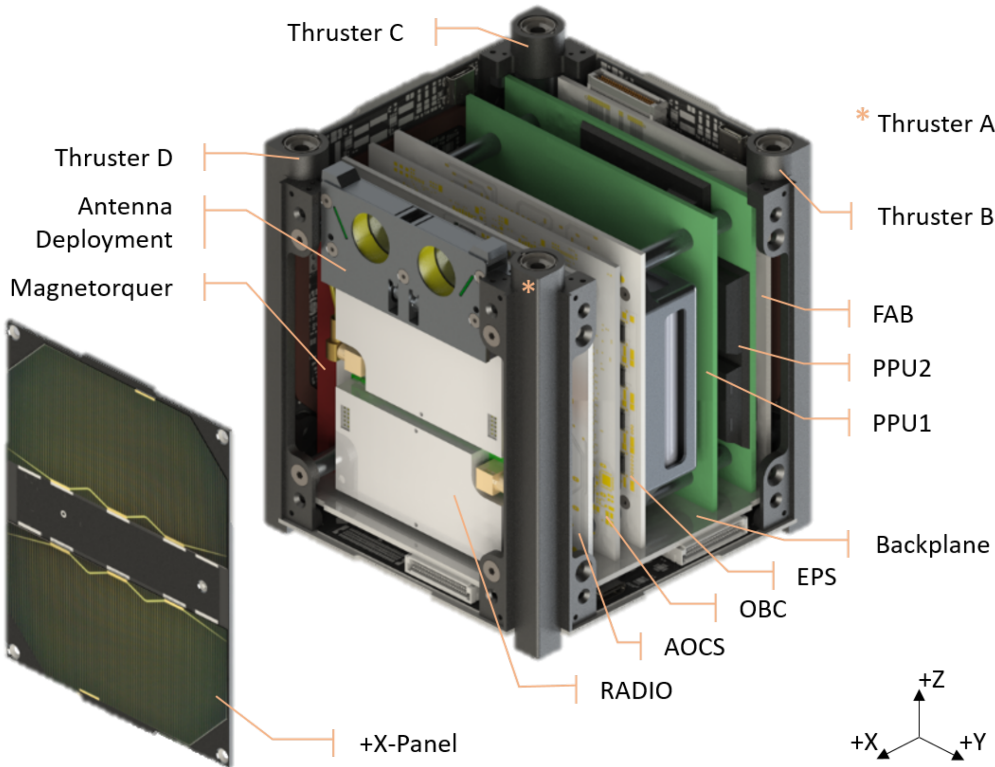


Figure 1.1: UWE-4 CubeSat exploded view (Kramer et al., 2020)

As the smallsats becomes more complex, the risks of failure is growing. Along with the performance, reliability of small satellites must be increased to make nanosatellites an accepted platform for scientific payloads and commercial applications (Langer and Bouwmeester, 2016). On-orbit repair is almost impossible, since the costs would vastly exceed that of the total satellite production and launch, especially for smallsats. Successful on-orbit repairs have been made only to inhabited orbital stations, the Solar Maximum Mission and the Hubble Space Telescope. It is therefore essential to the potential satellite malfunctions be identified before their launch.

Attitude Determination and Control System (ADCS) is one of the most complex and sensitive subsystems of a satellite as it controls its orientation and provides pointing and maneuvers capabilities. ADCS ensures safety at the most critical initial mission stages and is responsible for correct operations of the satellite (Gavrilovich, 2018). Increasing complexity of ADCS hardware and control algorithms (Xia, 2017; Xie et al., 2016), along with the extensive use of COTS components and reduced development time, makes the ADCS careful pre-flight assessment of paramount importance (Martin, 2018). Its dy-

1.1. ADCS ground testing

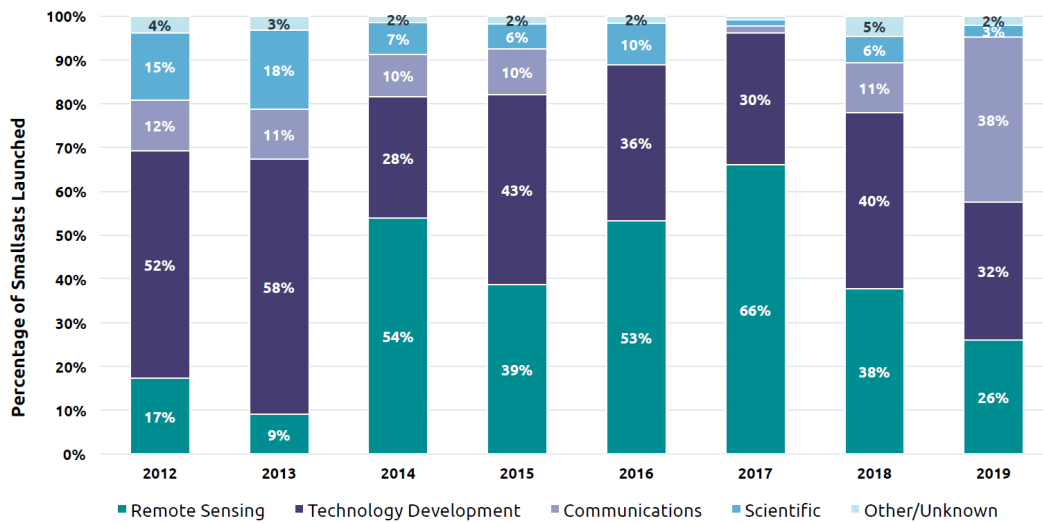


Figure 1.2: Share of small sats by use (Bok et al., 2020)

dynamic and static performances is potentially limiting and risk factors for future nanosatellite missions.

1.1 ADCS ground testing

Software and hardware pre-flight ground verification aims at demonstrating and certifying satellites components, systems and safety functions operability. For a reliable testing the satellite shall be placed in conditions close to the on-orbit one. Small organizations, like academic institutions, seldom have access to specialized and expensive testing facilities, and often underestimate the importance of ground testing. Insufficient testing is one of the reasons of nanosatellites high failure rate. To provide smallsats developers with appropriate testing guidelines, several test requirements have been developed in past two decades (Cho et al., 2012). Only recently an ISO standard have been approved (ISO 19683:2017 : Space systems — Design qualification and acceptance tests of small spacecraft and units).

In this thesis, we will focus on ADCS related facilities, which can be classified as simulators and testbeds: the first ones are used mainly for studying control laws, meanwhile the second ones for assessing integrated hardware equipment, i.e Hardware-in-The-Loop testing. Several on-orbit environment aspects needs to be simulated, as ADCS can possibly rely on magnetic field, sunlight and stars position.

- Sunlight: sun simulators spans from correctly sized lamp to precisely calibrated light sources and specific optical systems, and are designed in function of the ADCS sun sensor. Specifications for sun simulators are provided by [ASTM \(2010\)](#) standard. The classification is done by spectral content, spatial uniformity and temporal stability.
- Stars position: starry sky simulations is a challenging task, as the latest generations of star trackers (a device that measures the positions of stars) feature widened range of functionality: reliable simulations need for complex hardware and software solutions ([Rufino et al., 2013](#)).
- Magnetic field: since both attitude determination and control are likely to rely on magnetic field, it's highly desirable the simulator to be equipped with system capable to cancel the local Earth and provide an arbitrary magnetic field. A common device, used in the wide range of applications were controlled magnetic field is necessary, is the Helmholtz cage ([Trout, 1988](#)). Made of Helmholtz coils, these can be easily constructed as basically consist of two identical circular coils of wire with identical electrical currents flowing in the same direction, with a common axis and placed at a distance approximately equal to the radii of the coil. To provide three-axis control, three couples of coils are employed. The generated magnetic field can be computed analytically and sized so as to guarantee certain level of uniformity in the volume of interest ([Da Silva et al., 2019](#)).
- Microgravity: disturbance-free rotational and/or planar dynamics are necessary for HIL testing, but are challenging to achieve in laboratory environment. Microgravity simulator is the core subsystem of the testing facility, necessary for dynamic attitude simulations.

1.1.1 Dynamic simulators

Simulators providing microgravity environment have been developed since the beginning of the space race: there are several open documentary references from early 60s ([Bachofer and Seaman, 1964](#); [Smith, 1964](#); [Fornoff, 1967](#)). Perhaps the simplest way to provide low torque environment is based on wire suspension: the prototype is suspended on cable attached to a low friction joint, so as to provide 1-DOF. Large assemblies can be tested on gravity offload systems : counter-weights are used to offload weight and compensate the gravity by applying tension force ([Han et al., 2010](#)). Differences between

1.1. ADCS ground testing

on-orbit and terrestrial environments calls for more complex systems, especially for critical operations, such as docking and rendezvous: see [Wilde et al. \(2019\)](#) for historical and recent developments in this field.

Since large rotational and planar freedom is needed for the ADCS HIL tests, the simpler and most common solution adopted are air bearings ([Schwartz et al., 2003](#)). Flowing pressurized air through several orifices or a porous surfaces, air film is formed. The air operates as a lubricant and provides very small friction between two contact surfaces. If contact surfaces are flat, two translation and one rotational (around the yaw axis) degree-of-freedom are provided(see [Rybus and Seweryn](#) for more examples and details on this type of simulators).

The same principles applies to spherical air bearings, employed to provide frictionless rotational dynamics with unconstrained rotation over one, two or even three axes. Most facilitates where disturbance-free rotational dynamics are required relies on this solutions, with main examples described in [Schwartz et al. \(2003\)](#) survey. Unconstrained motion over three axes can be achieved by placing under test a floating sphere (see [Wang et al.](#); [Jovanovic and Pearce](#); [Prado-Molina et al.](#); [Culton et al.](#) for some of solutions available in the literature) or more sophisticated designs, for example involving robotic arm ([Gavrilovich et al., 2015](#)). Most common setups can be categorized in three broad configurations, namely table-top , dumbbell and umbrella, shown in Figure 1.3. While dumbbell layout provides unconstrained rotational motion about two axes, table-top is the simplest and lightest design choice, coming at the cost of limited tilt angles.

Planar and rotational air bearings can be combined to achieve all 6-DOF. To provide motion on vertical direction, complex solution may be necessary, as a matched variable-mass counterbalance system proposed in [Saulnier et al. \(2014\)](#). See [Nakka et al. \(2018\)](#) for more examples of 6-DOF simulators.

1.1.2 Nanosatellites testing facilities

Despite ADCS simulators are certainly not a new concept, legacy solutions developed for larger satellites testing cannot be employed for smallsats mainly due to the unacceptably high level of residual perturbations. As the number of nanosatellites developers increases, the need for dedicated ADCS testbeds is growing. Almost all existing implementations integrates spherical air-bearings, as the most cost-effective solution.

As the hosted satellite getting smaller, the target residual environmental disturbance torque drops and the facility characterization clearly becomes of great importance. The

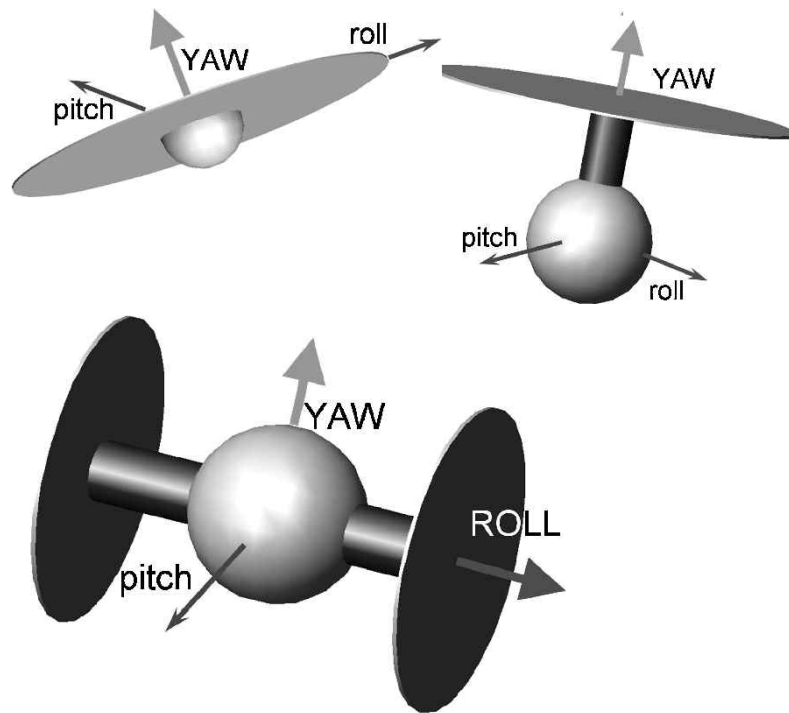


Figure 1.3: From top to bottom: tabletop, umbrella and dumbbell air bearing platform setup (Schwartz et al., 2003).

largest disturbance torque affecting spherical air-bearing test benches is the one due to gravity (Kwan et al., 2015; Prado et al., 1998; Thomas et al., 2018): to reduce the gravitational torque, the unbalance vector, defined as the distance between the center of mass (CM) and the center of rotation (CR), must be minimized. Static balancing can be achieved by weighting masses, but the deformation of the platform due to temperature change (Prado et al., 1998) and anisotropy (Kim and Agrawal, 2009; Xiang et al., 2015) could be source of dynamic disturbance. Careful design and material choice are crucial, but not sufficient (Xiang et al., 2015).

Gravitational torque must be specifically addressed to guarantee reliable simulations (Gavrilovich et al., 2015), as it can be canceled only partially by design, and manual balancing does not guarantee a priori performance level (Prado et al., 1998; Young, 1998). Stiffening of the floating platform and dedicated balancing systems lead to further weight growth, which in turn is proportional to the residual gravitational disturbance torque. The outcome are contrasting simulator design requirements:

- moments of inertia must be similar to that of the simulated/tested spacecraft;
- weight have to be limited;

1.1. ADCS ground testing

- platform and system design must be robust to reduce sagging;
- dumb masses for fine balancing have to be provided;
- dedicated balancing system is highly desirable.

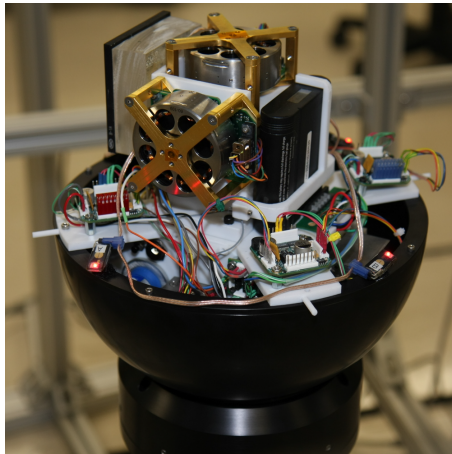
The trade-off is particularly challenging for smallsats as the target disturbance torque and moments of inertia are scaled down. For such facilities, only few attempts to show ground-to-flight simulations traceability are reported (Sternberg et al., 2018), highlighting the difficulty to achieve reliable on-ground simulations. Indeed, the external torque acting on a nanosatellite in Low Earth Orbit can be as low as 10^{-6} Nm (Cortiella et al., 2016; Sutherland et al., 2017).

A remarkable example of nanosatellites testing facilities is the CubeSat three axes simulator (CubeTAS) developed by the Naval Postgraduate School (NPS) with collaborations from UC Santa Cruz Chesi et al. (2015). The CubeSat-scale air bearing incorporates an automatic mass balancing system that aligns the composite system CM with the air bearing's CR (Chesi et al., 2014). Experimental results demonstrated capabilities of the testbed to successfully simulate CubeSat rotational dynamics, as well as perform three-axis stabilization maneuvers (Lee et al., 2018). The system also includes a Helmholtz cage for three-axis magnetic field simulation, and experimental magnetic detumbling was presented in Cervettini et al. (2020).

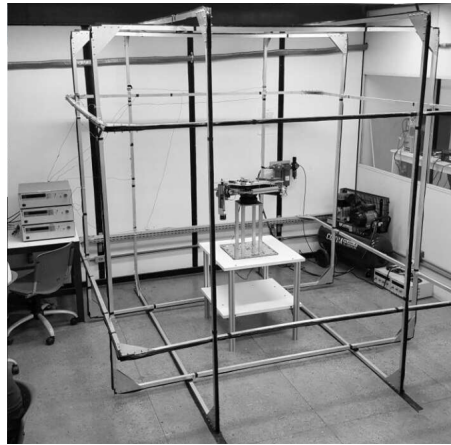
At the Laboratory of Application and Innovation in Aerospace Science (LAICA), University of Brasilia, a tabletop-style air bearing facility have been designed (Silva et al., 2019). A Helmholtz cage provides controlled magnetic field, and despite the use of COTS and self-developed components, good system performance was reached.

Another tabletop-style air bearing platform for CubeSat HIL testing have been proposed by York University in Toronto (Ustrzycki et al., 2011). Manual balancing system cause large gravitational torques evident from testing; however, control algorithms were successfully tested. A Helmholtz cage is foreseen, but no results on experiments employing controlled magnetic field are available. Similar solution including an automatic balancing system have been proposed by Virginia Tech Space Simulations Laboratory in Wolosik (2018), and by Air Force Institute of technology Tibbs (2015).

To overcome rotational constraints of tabletop air-bearing, an original design have been developed at the Laboratory of Informatics, Robotics and Microelectronics at the University of Montpellier (Gavrilovich et al., 2015). Unconstrained motion about three axis is provided by a peculiar design. Four air bearings with the rotors distributed on a



(a) CubeTAS simulator (Chesi et al., 2015);



(b) LAICA facility (Da Silva et al., 2019);



(c) Testbed developed at the University of Montpellier (Gavrilovich, 2018);

Figure 1.4: Nanosatellites testing facilities.

spherical envelope that surrounds the model spacecraft, which is intended to be a Cube-Sat. The stators are distributed on an external sphere attached to a robotic arm, which must ensure the facing between the stator and its rotor during spacecraft rotational motion. The concept requires a robotic arm to adjust its orientation depending on the spacecraft attitude determined by attitude sensors.

1.1.3 Facility verification

Especially for in-house developments, the verification of each environmental feature simulated within an ADCS facility is fundamental, yet often overlooked. In particular:

- For the magnetic field, accuracy and homogeneity in the operative volume should be verified.
- For the sunlight, spectral content, temporal stability and spatial uniformity, which can be subdivided in divergence and intensity uniformity, have to be measured.
- Disturbances affecting the rotational dynamics shall be characterized. As the sources of disturbances could be very different in static and dynamic setting, and depend on time/temperature/simulation scenario, they have to be evaluated separately. In spherical air-bearings, unbalance torque is the largest and most addressed in the literature.
- A ground truth attitude shall be provided by a system with known performance, which most of the time consists of an external vision system.
- Star simulators are still very uncommon: verification process depends on the specific implementation.

Solutions reported in the literature are characterized by partial verification of the system performance. Among the performance indexes, one of the most challenging to estimate and to comply with is the disturbance torque. Facilities with verified performance suited for nanosatellites testing are mentioned hereafter:

- for the NPS facility, results of the balancing and rated accuracy of the vision system are provided. Balancing is evaluated by kinetic energy variance reduction (Chesi et al., 2014). However, the 71 % variance reduction cannot be used to estimate the residual disturbance torque; nevertheless, the facility have been successfully employed for attitude control law testings (Lee et al., 2018).
- for the LAICA facility, results on the magnetic field homogeneity and balancing system performance are presented. However, the residual gravitational disturbance is estimated to be more than 20 mNm (Da Silva et al., 2019).

- In [Kato et al. \(2014\)](#), FACE facility at DLR, Germany, is described. Helmholtz cage accuracy is evaluated. The balancing procedure guarantee high performance, however the total weight is too high for reliable nanosatellites testing.
- The simulator developed at Virginia university ([Thomas et al., 2018](#)) implements an offline balancing procedure. No experimental results are provided, but the residual disturbance torque is expected to be higher than 7.6 mNm ([Wolosik, 2018](#)).
- The balancing procedure proposed in [Young \(1998\)](#) and tested on a smallsat simulator provides residual torque in the order of 4.9 mNm.
- The procedure proposed by [Young](#) have been further developed by [Prado et al. \(1998\)](#). Thanks to a feedback law and robustified carbon-fiber platform, a residual static disturbance torque of 2 mNm has been achieved.
- The CM estimation algorithm proposed in [Gavrilovich et al. \(2015\)](#) shows high performance in simulations, providing residual unbalance torque in the order of $5 \cdot 10^{-5}$ Nm. However, high friction torque of 0.02 Nm, owed to the simulator structure, precluded experimental verification of the system performance.
- In [Wu et al. \(2014\)](#), accuracy data for the vision system of an air bearing testbed for spinning satellites developed at the Surrey Space Center are provided, with attitude and angular speed determination accuracy respectively of 0.06° and $0.15^\circ/s$. No information on other environmental aspects are provided.

The facilities characteristics are summarized in Table 1.1. As it possible to see, subsystems verification is mostly incomplete and none of them reached the $\approx 10^{-6}$ Nm residual disturbance target.

1.1.4 The Dynamic Testbed for CubeSats facility at University of Bologna

During the past four years, a Three-Degrees of Freedom Dynamic Testbed for CubeSats (DTC) facility have been developed at the Microsatellites and Space Microsystems (μ 3S) laboratory of the Department of Industrial Engineering at the University of Bologna. Due to the large variety of nanosatellite missions, e.g., Earth observation, in-orbit demonstration (IOD), remote sensing, astronomical observation, wherever on or beyond Earth orbit, a single facility could hardly fit the needs of the entire range of ADCS

1.1. ADCS ground testing

Table 1.1: ADCS testing facilities overview

Facility	Environment aspect			Metrology System
	Controlled Magnetic Field	Sun simulator	Residual disturbance torque	
Chesi et al. (2014)	✓	✓	Not enough info	Stereo VS
Young (1998)	-	-	$> 4.9 \cdot 10^{-3} Nm$	-
Prado et al. (1998)	-	-	$> 2 \cdot 10^{-3} Nm$	-
Da Silva et al. (2019)	✓	-	Est.: $> 2 \cdot 10^{-4} Nm$	-
Gavrilovich et al. (2015)	-	-	$> 0.02 Nm$	-
Wolosik (2018)	✓	-	Est.: $> 7.6 \cdot 10^{-3} Nm$	-
Kato et al. (2014)	✓	✓	Not enough info	IMU
Wu et al. (2014)	-	-	-	Stereo VS

hardware combinations testing. Through DTC development, we considered as the target application scenario the one of nanosatellite missions in Low Earth Orbit (LEO) for remote sensing, IOD, or Earth observation, whose pointing requirements often fall in the range from tens of arcminutes to one degree (Werner et al., 2018; Gerhardt et al., 2016; Mero et al., 2015).

The 1U and 3U CubeSat sizes were used as reference, as the most common (Bok et al., 2020); nevertheless the facility can host nanosatellites of size up to 6U, or not necessarily compliant to the CubeSat standard. The core of the testbed is a table-top air bearing platform with custom design, whose function is to hold the nanosatellite mock-up under test; it includes an automatic balancing system with shifting masses actuated by linear motors. A programmable CubeSat mockup is available for simulations and control laws testing. Other subsystems includes a Helmholtz cage for geomagnetic field simulation, a Sun simulator, and a metrology vision system for ground-truth attitude measurement.

1.1.5 Objectives and contributions

Several aspects of DTC have been designed and implemented by the author as part of work presented in this thesis. Development of the table-top platform, the automatic mass balancing system, the overall facility commissioning and experimental verification will be presented in this thesis work. Strict budget constraints led the design choices towards reduced complexity, making extensive use of low-end off-the-shelf hardware.

Similar facilities, described in Section 1.1.3, miss any performance verification or focuses on testing of one or two specific subsystems at most. To the best of author's knowledge, none of the existing works approaches the testbed integration with systematic performance verification for all its subsystems, see Table 1.1. When available, residual disturbance torque is estimated indirectly and most of the time is larger than the target one.

The automatic balancing system developed for DTC relies on three sliding masses, actuated independently by three electric motors, to create a three-dimensional mass displacement for fine balancing. A microcontroller and an IMU complete the setup.

A novel feedback control algorithm was designed to achieve high-precision balancing in two steps: the first part of the procedure automatically adjusts the location of the sliding masses to eliminate the unknown offset between the center of rotation and the center of mass in the plane orthogonal to the gravity vector. Then, the inertia parameters and the remaining offset component are estimated by collecting free oscillating platform data. Sampled data are processed offline through a batch least squares (LSQ) algorithm, implemented in MATLAB environment. The entire procedure is then iterated to incrementally refine the unbalance compensation, assuming the inertia known from the first iteration estimate.

To reduce anisoelasticity torques, efficient structural design is a key approach. A mechanical structure for supporting the satellite and all the components necessary for the testbed operations was designed to guarantee minimal deformation torque. The choice of platform material and design are a trade-off between elasticity and reduced inertia values. Amagnetic material have been employed whenever possible, and high-end COTS air-bearing by Physikal Instruments guarantee limited disturbance torque.

To estimate the design and balancing system effectiveness, the disturbance torque acting on the free oscillating platform after balancing is estimated by inspection of the angular momentum variation. The testing procedure guarantees a reduction of the residual torque down to less than $5 \cdot 10^{-5} \text{Nm}$. This objective is reached by comparing, through

extensive numerical and experimental testing, alternative control techniques and data processing strategies, and by combining them to maximize the performances.

Throughout the facility commissioning, a user-friendly software interface was also developed, which allows setting of the desired magnetic field, control gains for the automatic balancing algorithm, and other system parameters.

Eventually, a COTS CubeSat mockup was integrated in the facility: the platform with the installed mockup was used as a simulator for experimental testing of attitude control laws.

1.2 Nanosatellites attitude control

Whereas nanosatellites places a whole set of new challenges on the ADCS design, the choice of actuators is limited by strict system requirements. Among the actuators which are suited for smallsats, magnetorquers are particularly attractive due to low weight, energy efficiency, long lifetime, and high reliability.

Magnetorquers, or magnetic rods, creates a magnetic dipole that interacts with the external magnetic field, thus are suited for Earth orbiting missions. The magnetic actuation is cheap and suitable for a smooth modulation of the control torque. These actuators do not induce unwanted coupling with the flexible modes, differently from thrusters and mechanical actuators (Silani and Lovera, 2005; Avanzini and Giulietti, 2012). Widely used for the detumbling (Desouky and Abdelkhalik, 2020), or in combination with different types of actuation (De Angelis et al., 2016), they became increasingly popular: about 40 % of flown nanosatellites have magnetic rods for active magnetic attitude control (Bouwmeester and Guo, 2010). However, due to the time variation of magnetic field and instantaneous underactuation of a magnetically actuated spacecraft, attitude control is hindered by several limitations, addressed in many publications in the last decades, categorized and reviewed in detail in Silani and Lovera (2005) and Ovchinnikov and Roldugin (2019).

Despite the large number of publications, magnetic attitude control is still an open field since low pointing errors and robustness are difficult to achieve at the same time: engineers and researchers seek for novel approaches to overcome the intrinsic limitations.

1.2.1 Magnetic attitude control techniques

Magnetic actuators can be used for variety of control tasks: detumbling (Avanzini and Giulietti, 2012), momentum damping (Stickler and Alfried, 1974) and spin-axis pointing (Avanzini et al., 2014). However, robust global asymptotic attitude stabilization of a satellite actuated by solely magnetorquers is hindered by several obstructions, related to the inherent underactuation. Rigid body attitude topology precludes the existence of a globally stabilizing continuous feedback (Mayhew et al., 2011), and even local asymptotic stabilization by continuous feedback is impossible in case of underactuation (Bhat and Bernstein, 2000).

Magnetic field variation due to the orbital motion provides controllability under some non-restrictive assumptions (Bhat, 2005). If controllability necessary assumptions are satisfied, a straightforward way to address underactuation is by analyzing the averaged linear dynamics (Stickler and Alfried, 1974). The time-varying model of the magnetically actuated spacecraft is replaced with an approximate time invariant one. However, the stability has to be verified a-posteriori, and closed-loop performance is limited. Alternatively, since the Earth magnetic field is essentially that of a magnetic dipole, the quasi-periodic variability of the geomagnetic field along the orbit can be exploited, and the system approximated to be time periodic (Lovera, 2000). Local dynamics were studied through the optimal periodic control theory in Wiśniewski (2000) and Lovera et al. (2002), among others. The resulting feedback system is locally asymptotically stable but requires burdensome solution of a periodic Riccati equation. For satellites with open-loop stable configurations, such solution is shown to converge to a constant value and onboard computation and storage can be avoided (Wiśniewski, 2000; Psiaki, 2000). However, stability must be checked a-posteriori by Floquet theorem. Despite the above challenges, flight results proved the feasibility of 3-axis magnetic control for mini- and micro-satellites (Chasset et al., 2013). More recently, nonlinear control design for magnetically actuated spacecrafts was considered assuming a not necessarily periodic variation of the geomagnetic field. Averaging theory for nonlinear systems was used in (Lovera and Astolfi, 2004) to show that a PD-like controller is almost globally stable for sufficiently small gains. Global stability comes at the cost of gains limited by design, as a consequence of averaging, which leads to large convergence time. A projected PD controller with state dependent time-variant gains has been proposed in (Invernizzi and Lovera, 2019), with improved performances in comparison to constant gains.

Nevertheless, system uncertainties and external disturbances severely degrade the

performance of projected PD controllers, motivating the quest for robust controllers. Inertia uncertainties alone were addressed in [Celani \(2015\)](#). Joint the magnetic field and inertia parameters uncertainties have been addressed in an optimal way in [Rodríguez-Vázquez et al. \(2015\)](#) by solving a sequence of finite horizon problems, but no external torque have been considered.

In the assumption of linearized dynamics, robustness to disturbances can be achieved through the H-inf approach. A H-inf controller is proposed in [Lovera \(2000\)](#) to guarantee matched disturbances rejection. In [Zanchettin and Lovera \(2011\)](#), an H-inf locally robust, asymptotically stabilizing controller is designed through the tuning of a structured constant-gain controller. However, global stability is not provided.

1.2.2 Uniting control problem

In the existing works on magnetic attitude control, local optimal solutions are opposed to global controllers. In this respect, uniting of local and global controllers may be pursued to achieve precise control nearby an operating point while maintaining desirable global stability properties. In general, the uniting control problem cannot be solved by considering only continuous feedbacks ([Prieur, 2001](#)), and switching between control laws is not straightforward, since the union of two stable laws can be unstable or non-robust ([Liberzon, 2003](#)). Robustness can be addressed by adding hysteresis to the switching laws ([Prieur, 2001](#)), taking advantage of regions where both controllers are appropriate. The uniting control problem with hysteresis can be cast into the more general framework of hybrid systems, i.e. systems with mixed continuous—discontinuous dynamics ([Goebel et al., 2012](#)). In this case each controller, possibly hybrid itself, is designed to operate in appropriately designed regions of the state space and a mechanism acting as a “supervisor” switches between them through a logic variable, so that the state is driven to the desired set ([Sanfelice et al., 2008](#)). Such an approach was followed in [Mayhew et al. \(2011\)](#), to develop a hybrid PD controller for a fully actuated spacecraft, which provides global attitude stabilization and overcome attitude state space parametrization topological obstruction. This type of control has been shown to be robust with respect to external disturbances, thanks to a memory variable and a hysteresis region.

1.2.3 Objectives and contributions

Inspired by the idea of uniting two controllers, the author proposed a novel approach to the three-axis attitude control of a magnetically actuated spacecraft based on hybrid systems theory. The approach envisaged seeks to mitigate the limitations of existing solutions to the attitude control of a magnetically actuated spacecraft, by designing a hybrid controller which matches exactly a locally optimal one in a neighborhood of the origin, ensuring at the same time global stability and robustness. This is achieved by designing a supervisor which selects, as function of the state, the most appropriate between two controllers and embedding a hysteresis region which prevents multiple switching to occur. The controllers' domains are designed according to appropriate input–output functions, with disturbance being the input. For the local controller, the input/output function is chosen as the H-inf norm of the frequency response operator, as proposed in [Zanchettin et al. \(2013\)](#). Far from the origin, a projected, PD hybrid controller derived from the one in [Hu and Zhang \(2018\)](#) is instead employed, whose input–output gain function is computed after analyzing its Input-to-State stability (ISS) properties.

The resulting hybrid controller is shown to be global, robust and optimal in the neighbourhood of the origin. Hybrid control theory is employed to develop a mixed continuous-discrete controller able to switch between different feedbacks. Controllers' domains are designed according to appropriate input–output functions and to the magnitude of disturbances affecting the system. As a result, global attitude stability is ensured, while achieving local optimality and robustness against bounded disturbances, both matched and unmatched by the control action, and measurement noise. Analytical results are verified by means of realistic numerical simulations: the state errors comply with the computed bounds and stability is guaranteed for conservative assumptions on the magnitude of the unmatched disturbances.

Even though the bare pointing accuracy is not improved with respect to the one of the local controller alone, the proposed approach provides some remarkable advantages, such as guaranteed level of performance in case of peak disturbances and stability for any initial condition. This work presents, to the best of the authors' knowledge, the first control law satisfying these characteristics for a magnetically actuated spacecraft. As such, it is also intended to bring deserved visibility to hybrid control within the space engineering community.

1.3 Outline

In the Chapter 2 mathematical models, rigid body dynamics/kinematics and control theory are presented. In Part 2, development of the ground testing facility is addressed. Whole facility design and each subsystem are described in Chapter 3. In Chapter 4, novel automatic mass balancing subsystem design is presented, together with numerical simulations and experimental testing results. In the last part of the thesis, we focus on attitude control of smallsats. Novel attitude control algorithm is developed in Chapter 5. In Chapter 6, research results and achievements are summarized.

2

Preliminaries

In this chapter, the mathematical models and control theory concepts that provides the necessary background to the topics presented in the following chapters are briefly discusses. Basic notions and the description of the attitude control problem are introduced.

Notation and frames of reference used throughout the work are introduced in Section 2.1. In Section 2.2, the kinematic and dynamic models of a rigid body are presented along with attitude representations. The attitude dynamics of a rigid body equipped with moving shifting masses is described in Sections 2.3. In Sections 2.4 model of magnetically actuated spacecraft is described in case linearized and nonlinear models are considered.

Control fundamentals and definitions the reader should be familiar with are summarized in Section 2.5. These includes tools for the analysis of Linear Time Periodic (LTP) systems and definitions of stability. Section 2.6 is dedicated to mixed continuous/discontinuous (hybrid) systems and to the extended stability concept for those.

In the last Section 2.7, environmental models are discussed and formulas for the computation of disturbances torques are presented.

2.1 Notation and reference frames

In this work, bold symbols, such as \mathbf{v} , indicate vectors, and plain lower case symbols "v" indicate scalars. Given $\mathbf{v} \in \mathbb{R}^3$, we define the skew-symmetric operator operator $[\mathbf{v}]^\times$, which acts on \mathbf{v} as follows:

$$[\mathbf{v}]^\times = \begin{bmatrix} 0 & -v_3 & v_2 \\ v_3 & 0 & -v_1 \\ -v_2 & v_1 & 0 \end{bmatrix}, \quad (2.1)$$

and $[\mathbf{v}]^\times \mathbf{a}$ represents the cross product of vectors \mathbf{v} and \mathbf{a} . $\hat{\mathbf{v}}$ represents the unit vector in the direction of \mathbf{v} . We denote \mathbf{v}_i and \mathbf{v}_b a generic vector $\mathbf{v} \in \mathbb{R}^3$ defined, respectively, in the inertial reference frame \mathcal{F}_i and body reference frame \mathcal{F}_b . R_i^b indicates a rotation matrix from inertial to body reference frame. If not otherwise specified, all vectors are indicated in body reference frame for simplicity.

2.1.1 Coordinate reference frames

In this work, following coordinate reference frames are used:

- Earth-Centered Inertial frame (ECI): the origin of this frame is in the center of the Earth. This reference frame is denoted by i : $\hat{\mathbf{e}}_{i,x}$ axis is parallel to the vernal equinox direction, $\hat{\mathbf{e}}_{i,z}$ axis coincides with Earth rotation axis and it is northward directed, and $\hat{\mathbf{e}}_{i,y}$ completes an orthogonal right-handed frame. For Earth orbiting spacecraft, \mathcal{F}_i is an inertial frame.
- Principal axes body frame: body frame is centered at the body center of mass. Principal axes frame is a specific body-fixed reference frame whose axes are coincident with the principal axes of inertia. We denote the coordinate axes of body reference frame by $\hat{\mathbf{e}}_{b,x}$, $\hat{\mathbf{e}}_{b,y}$ and $\hat{\mathbf{e}}_{b,z}$.

2.2 Rigid body kinematics and dynamics

In this section well known fundamentals about rigid body motion are briefly recalled. The presented material is taken from [Hughes \(1986\)](#); [Schaub and Junkis \(2009\)](#); [Wie \(2008\)](#).

2.2.1 Attitude representation

There are several possible ways, each with its own advantages and disadvantages, of representing attitude of a reference frame with respect to another. Three possible representation will be briefly discussed: Direction Cosine Matrix (DCM), Euler angles, and Euler parameters (quaternions).

Direction Cosine Matrix

Suppose we have a vector $\mathbf{v} \in \mathbb{R}^3$ with known components in body reference frame $\mathcal{F}_b = [\hat{\mathbf{e}}_{b,x}^T \ \hat{\mathbf{e}}_{b,y}^T \ \hat{\mathbf{e}}_{b,z}^T]$, denoted as $\mathbf{v}_b \in \mathbb{R}^3$. To determine its representation \mathbf{v}_i in $\mathcal{F}_i = [\hat{\mathbf{e}}_{i,x}^T \ \hat{\mathbf{e}}_{i,y}^T \ \hat{\mathbf{e}}_{i,z}^T]$, we have to use rotations. Since:

$$\mathbf{v} = \mathbf{v}_b^T \mathcal{F}_b = \mathbf{v}_i^T \mathcal{F}_i, \quad (2.2)$$

we need a way to express \mathcal{F}_i in terms of \mathcal{F}_b . It can be done by a 3×3 rotation matrix $R_i^b \in SO(3)$:

$$\mathcal{F}_b = R_i^b \mathcal{F}_i. \quad (2.3)$$

Thus, to compute \mathbf{v}_i , we just need to determine R_i^b :

$$\mathbf{v}_b = R_i^b \mathbf{v}_i. \quad (2.4)$$

The rotation matrix R_i^b , referred to simply as R in the following, is named DCM or *Direction Cosine Matrix*, as the components of the rotation matrix are the direction cosines between the two sets of reference axes, and is given by:

$$R_i^b = \begin{bmatrix} C_{\theta_{xx}} & C_{\theta_{xy}} & C_{\theta_{xz}} \\ C_{\theta_{yx}} & C_{\theta_{yy}} & C_{\theta_{yz}} \\ C_{\theta_{zx}} & C_{\theta_{zy}} & C_{s\theta_{zz}} \end{bmatrix} \quad (2.5)$$

2.2. Rigid body kinematics and dynamics

where $C_{\theta_{xy}}$ is the cosine of the angle between the x-axis of the body frame and the y-axis of the inertial frame.

Euler Angles

The *Euler angles* is a class of minimal sets of parameters for representation of the angular orientation. Each Euler angle describes a rotation about one axis of the reference frame, which leads to an intuitive geometric interpretation. Three principal rotations can fully describe three-dimensional rotations (Hughes, 1986):

$$R(\boldsymbol{\theta}) \equiv R_{c''}(\theta_3)R_{b'}(\theta_2)R_a(\theta_1). \quad (2.6)$$

$R_a(\theta_1)$ indicates a θ_1 rotation about the a -axis of the reference frame, $R_{b'}(\theta_2)$ indicates a rotation of θ_2 about the axis b' of the new frame resulting from the previous rotation, and $R_{c''}(\theta_3)$ is the rotation about c'' axis of last intermediate frame. The choice and order of the axes 'a/b/c' of each elementary rotation are arbitrary as their corresponding principal axes, as long as none of the two successive rotations are about the same axis. $\boldsymbol{\theta} = [\theta_1 \ \theta_2 \ \theta_3]^T$ is the vector of Euler angles.

In this work, the 1-2-3 sequence of rotation is employed:

- The first rotation is a roll of angle ϕ around the inertial \hat{e}_x^i axis;
- The next rotation is a pitch around the intermediate y' -axis of angle θ ;
- The last rotation , yaw, is of angle ψ around the z'' -axis.

Starting from the vector $\boldsymbol{\theta} = [\phi \ \theta \ \psi]^T$, it is possible to define the corresponding DCM in the following way:

$$R(\boldsymbol{\theta}) = \begin{bmatrix} C_\psi C_\theta & C_\psi S_\theta S_\phi + S_\psi C_\phi & -C_\psi S_\theta C_\phi + S_\psi S_\phi \\ -S_\psi C_\theta & -S_\psi S_\theta S_\phi + C_\psi C_\phi & S_\psi S_\theta C_\phi + C_\psi S_\phi \\ S_\theta & -C_\theta S_\phi & C_\theta C_\phi \end{bmatrix}, \quad (2.7)$$

with C indicating a cosine function and S a sine function.

Euler parameters

As it is well known, the Euler angles representation suffers from singularities, and it is not suited for numerical implementations of the spacecraft dynamics. Based on the Euler

Theorem, stating that the most general motion of a rigid body with fixed point is a rotation about a fixed axis \hat{e} by an angle Φ , a four variable, singularities-free representation of the attitude is defined, named *Euler parameters* or *quaternions*. Euler parameters are defined as follows:

$$\mathbf{q} = \begin{bmatrix} q_1 \\ q_2 \\ q_3 \\ q_4 \end{bmatrix} = \begin{bmatrix} \mathbf{q}_e \\ q_4 \end{bmatrix} = \begin{bmatrix} \hat{e} \sin \frac{\Phi}{2} \\ \cos \frac{\Phi}{2} \end{bmatrix} \quad (2.8)$$

where \mathbf{q}_e is the vector part that includes three of the parameters, and q_4 is the auxiliary scalar parameter, and must satisfy the following constraint:

$$q_1^2 + q_2^2 + q_3^2 + q_4^2 = 1. \quad (2.9)$$

Using the quaternion, DCM matrix can be defined as follow:

$$R(\mathbf{q}) = \begin{bmatrix} q_1^2 - q_2^2 - q_3^2 + q_4^2 & 2(q_1q_2 + q_3q_4) & 2(q_1q_3 - q_2q_4) \\ 2(q_1q_2 - q_3q_4) & -q_1^2 + q_2^2 - q_3^2 + q_4^2 & 2(q_2q_3 + q_1q_4) \\ 2(q_1q_3 + q_2q_4) & 2(q_2q_3 - q_1q_4) & -q_1^2 - q_2^2 + q_3^2 + q_4^2 \end{bmatrix}. \quad (2.10)$$

If Euler parameters/DCM attitude representation is known, roll, pitch, and yaw angle can be directly computed as follows:

$$\begin{aligned} \phi &= \arctan \frac{-R_{32}}{R_{33}} \\ \theta &= \arcsin R_{31} \\ \psi &= \arctan \frac{-R_{21}}{R_{11}}. \end{aligned} \quad (2.11)$$

2.2.2 Rotational kinematics

Rotational kinematics is the description of the orientation of a body that is in a rotational motion, and it does not involve any force associated with motion. We call

2.2. Rigid body kinematics and dynamics

$\boldsymbol{\omega} = [\omega_1 \ \omega_2 \ \omega_3]^T$ the absolute angular velocity vector. By deriving Eq.2.8, the rotational kinematics of a body with fixed center of rotation are given by:

$$\dot{\mathbf{q}} = \frac{1}{2}\boldsymbol{\Omega}\mathbf{q} = \frac{1}{2} \begin{bmatrix} 0 & \omega_3 & -\omega_2 & \omega_1 \\ -\omega_3 & 0 & \omega_1 & \omega_2 \\ \omega_2 & -\omega_1 & 0 & \omega_3 \\ -\omega_1 & -\omega_2 & -\omega_3 & 0 \end{bmatrix} \mathbf{q}. \quad (2.12)$$

The Eq. 2.12 can be rearranged as follows:

$$\begin{aligned} \dot{\mathbf{q}}_e &= -\frac{1}{2}(\boldsymbol{\omega} \times \mathbf{q}_e) + \frac{1}{2}q_4\boldsymbol{\omega} \\ \dot{q}_4 &= -\frac{1}{2}\boldsymbol{\omega}^T \mathbf{q}_e \end{aligned} \quad (2.13)$$

2.2.3 Rigid body dynamics

Rotational dynamics in an inertial frame are considered in the following. Let us define the total angular momentum \mathbf{h} , computed as:

$$\mathbf{h} = J\boldsymbol{\omega} \quad (2.14)$$

where J is the inertia matrix. It's always possible to define a rigid body reference frame such as the resulting J matrix is diagonal. The angular momentum dynamic equation of a rigid body about its center of mass is given by:

$$\dot{\mathbf{h}} = \left\{ \frac{d\mathbf{h}}{dt} \right\}_i = \left\{ \frac{d\mathbf{h}}{dt} \right\}_b + \boldsymbol{\omega} \times \mathbf{h} = \boldsymbol{\tau}_{tot} \quad (2.15)$$

where $\boldsymbol{\tau}_{tot}$ is the vector of all external torque acting on the body. Substituting the Eq. 2.14 into Eq. 2.15 and assuming a rigid body, we get dynamics equation:

$$J\dot{\boldsymbol{\omega}} + \boldsymbol{\omega} \times J\boldsymbol{\omega} = \boldsymbol{\tau}_{tot}. \quad (2.16)$$

2.3 Model of a rotating platform with integrated balancing system

In this section we outline the mathematical model for the system dynamics of an air-bearing platform with automatic balancing system, common to several other works, see for example [Chesi et al. \(2014\)](#) and [Gavrilovich et al. \(2015\)](#). The plane-balancing control problem is equivalent to stabilizing the hanging equilibrium point of a 3D pendulum ([Chaturvedi et al., 2005](#)), where the rotating platform is assimilated to a rigid body equipped with linearly moving point masses. The CR is fixed to a point in the inertial coordinate system \mathcal{F}_i , whose z axis is taken parallel to the local vertical. The IMU is aligned with the platform reference frame \mathcal{F}_b , centered at CR, and the balance masses can move only along a set of mutually orthogonal unit axes defined by \mathcal{F}_a , fixed with respect to the platform body reference one.

The relative orientation between frames is described by quaternion \mathbf{q} or equivalently by a rotation matrix R , and the rotational kinematics of the platform are function of the absolute angular velocity $\boldsymbol{\omega}$. The rotation matrix R can be expressed as a function of the quaternion following the equation 2.10. The gravity vector \mathbf{g} is expressed in body reference frame as:

$$\mathbf{g} = g\hat{\mathbf{g}} = gR(\mathbf{q})\hat{\mathbf{e}}_{i,z} \quad (2.17)$$

where g is the gravity vector magnitude and $\hat{\mathbf{e}}_{i,z} = [0 \ 0 \ 1]^T$. In spherical air bearing design we have to take into account the offset vector \mathbf{r}_{off} , computed as follows:

$$\mathbf{r}_{off} = \mathbf{r}_{CM} - \mathbf{r}_{CR} \quad (2.18)$$

where \mathbf{r}_{CR} is the position vector of the center of rotation and \mathbf{r}_{CM} indicates the center of mass. Since CR is inertially fixed, from now on it will be used as the origin of the reference system, hence $\mathbf{r}_{off} = \mathbf{r}_{CM}$. The offset vector produces a gravitational torque:

$$\boldsymbol{\tau}_{CM} = m_{tot}\mathbf{g} \times \mathbf{r}_{CM} \quad (2.19)$$

where m_{tot} is the total mass of free-to-rotate body. The torque produced by \mathbf{r}_{CM} can be compensated by placing a balance mass $m_{b,tot}$ at distance \mathbf{r}_b :

2.3. Model of a rotating platform with integrated balancing system

$$\boldsymbol{\tau}_u = m_{b,tot} \mathbf{g} \times \mathbf{r}_b, \quad (2.20)$$

where \mathbf{r}_b is set so as to provide $\boldsymbol{\tau}_u = \boldsymbol{\tau}_{CM}$.

Let us rewrite the dynamic equations Eq. 2.14 and Eq. 2.15 considering the action of $\boldsymbol{\tau}_{CM}$ and $\boldsymbol{\tau}_u$. The total angular momentum of the platform with moving masses is:

$$\mathbf{h} = J\boldsymbol{\omega} + \sum_{i=1}^3 \mathbf{r}_{b,i} \times m_{b,i} \dot{\mathbf{r}}_{b,i} \quad (2.21)$$

where the inertia matrix J is the sum of the platform inertia in body reference frame without balance masses J_S , plus the contribution due to the masses themselves, assumed to be punctiform:

$$J = J_S + \sum_{i=1}^3 (-m_{b,i} [\mathbf{r}_{b,i} \times] [\mathbf{r}_{b,i} \times]). \quad (2.22)$$

The angular momentum derivative is equal to:

$$\dot{\mathbf{h}} + \boldsymbol{\omega} \times \mathbf{h} = \mathbf{r}_{CR} \times m_{tot} \mathbf{g}^b + \boldsymbol{\tau}_u, \quad (2.23)$$

The rightmost term of Eq. 2.21 can be safely neglected if the dynamical contribution of the balancing masses is small enough. Following [Chesi et al. \(2014\)](#), the rotational dynamics of the simulator about CR, subject to gravity torque can be expressed as follows:

$$J\dot{\boldsymbol{\omega}} = -\boldsymbol{\omega} \times J\boldsymbol{\omega} + m_{tot} g \mathbf{r}_{CM} \times R^T \hat{\mathbf{e}}_3 + \boldsymbol{\tau}_u. \quad (2.24)$$

Note that Eq. 2.24 does not account for the angular momentum variation due to the temporal derivative of J , which is assumed to be negligible, due to the small stepper motors displacement speed. The only control torque available is due to the balancing masses, which is clearly constrained to lie in the direction normal to both the masses position vector and to the gravitational field direction. Once a control law is designed which provides a stabilizing $\boldsymbol{\tau}_u$, the control mass displacement components \mathbf{r}_b required to generate the desired torque can be computed according to :

$$\mathbf{r}_b = \frac{\mathbf{g} \times \boldsymbol{\tau}_u}{\|\mathbf{g}\|^2 m_b}. \quad (2.25)$$

2.4 Dynamical model of the magnetically actuated spacecraft

Consider an inertially pointing rigid spacecraft, aimed at aligning a principal body axes frame (BF) to the Earth-centered inertial (ECI) frame. In here, \mathbf{q} or, equivalently rotation matrix $R_i^b \in SO(3)$, indicates the attitude of the BF with respect to the ECI frame. $\boldsymbol{\omega}$ is the absolute angular velocity of the spacecraft expressed in BF. The rigid body dynamics are governed by Eulers's equations 2.14 and 2.15:

$$J\dot{\boldsymbol{\omega}} = -\boldsymbol{\omega} \times J\boldsymbol{\omega} + \boldsymbol{\tau}_{mc} + \boldsymbol{\tau}_d \quad (2.26)$$

where J is the spacecraft inertia matrix, $\boldsymbol{\tau}_{mc}$ is the control torque, $\boldsymbol{\tau}_d$ is the sum of external disturbance torques. For a magnetically actuated spacecraft, the only control torque available is the one generated by interaction between the on-board control dipole moment \mathbf{m}_c and the Earth magnetic field $\mathbf{b}(t) = [b_1(t), b_2(t), b_3(t)]$ through:

$$\boldsymbol{\tau}_{mc} = \mathbf{m}_c \times \mathbf{b}(t) \quad (2.27)$$

where we highlight that magnetic field vector is time-dependent.

Clearly, no control torque can be generated along the geomagnetic field vector, thus leading to instantaneous underactuation of the system. Given a desired control input, \mathbf{u} , the magnetic dipole required to generate control torque projected on the plane perpendicular to the geomagnetic field can be computed from:

$$\mathbf{m}_c = \frac{\mathbf{b}(t) \times \mathbf{u}}{\|\mathbf{b}(t)\|^2}. \quad (2.28)$$

2.4.1 Linearized model

Considering a reduced order state $\mathbf{x}_r = [\mathbf{q}_e^T, \boldsymbol{\omega}^T]^T$, the equations of motion can be linearized around the target attitude $\mathbf{0}_{6 \times 1}$ as in [Yang \(2012\)](#):

$$\dot{\mathbf{x}}_r = A\mathbf{x}_r + \begin{bmatrix} \mathbf{0}_{3 \times 3} \\ B_1(t) \end{bmatrix} \mathbf{m}_c + \begin{bmatrix} \mathbf{0}_{3 \times 1} \\ \boldsymbol{\tau}_d \end{bmatrix} = A\mathbf{x}_r + B(t)\mathbf{m}_c + B_d\boldsymbol{\tau}_d \quad (2.29)$$

2.4. Dynamical model of the magnetically actuated spacecraft

where $B(t)$ is the control matrix, $B_d = [\mathbf{0}_{3 \times 1}^T \mathbb{I}_{3 \times 1}^T]^T$ is the disturbance input matrix and for a diagonal inertia matrix $J = \text{diag}(J_1, J_2, J_3)$, $A, B_1(t)$ are given by:

$$A = \begin{bmatrix} \mathbf{0}_{3 \times 3} & 0.5\mathbb{I}_{3 \times 3} \\ \mathbf{0}_{3 \times 3} & \mathbf{0}_{3 \times 3} \end{bmatrix}, \quad B_1(t) = \begin{bmatrix} 0 & \frac{b_3(t)}{J_1} & -\frac{b_2(t)}{J_1} \\ \frac{-b_3(t)}{J_2} & 0 & \frac{b_1(t)}{J_2} \\ \frac{b_2(t)}{J_3} & \frac{-b_1(t)}{J_3} & 0 \end{bmatrix}. \quad (2.30)$$

2.4.2 Controllability of the nonlinear dynamics and of the linearized dynamics

The underactuated direction continuously changes with respect to the body axes system when the spacecraft moves along the orbit. Derived the linearized EOMs, it's possible to compute analytically the condition necessary for the controllability.

Definition 2.4.1. For a system $\dot{\mathbf{x}} = f(\mathbf{x}, t) + h(\mathbf{x}, t)\mathbf{u}$, define the reachable set $\mathcal{R}(\mathbf{x}_0, t_0)$ as the set of all the states $\bar{\mathbf{x}} \in \mathbb{R}^n$ for which there exist an input $f: \mathbb{R} \rightarrow \mathbb{R}^n$, \mathbf{u} s.t. solution ϕ of the system exist for which $\phi(t) = \bar{\mathbf{x}}$ for some $t \geq t_0$

Definition 2.4.2. A dynamical system $\dot{\mathbf{x}} = f(\mathbf{x}, \mathbf{u}, t)$, with $f: \mathbb{R}^n \times \mathbb{R}^m \times \mathbb{R} \rightarrow \mathbb{R}^n$, is said to be accessible if, for all $\mathbf{x} \in \mathbb{R}^n, t_0 \in \mathbb{R}$, $\mathcal{R}(\mathbf{x}_0, t_0)$ has a nonempty interior and strongly accessible if it has a nonempty interior for every $t > t_0$. The system is controllable if $\mathcal{R}(\mathbf{x}_0, t_0) \neq \emptyset \forall \mathbf{x}_0$ and t_0 .

If the variation of the magnetic field is at least almost-periodic, the three-axis attitude control is achievable and purely magnetic control is possible (Wiśniewski, 2000). In Yang (2016), the necessary assumptions for the controllability of the linearized system are reduced to a small number of sufficient conditions, summarized in Lemma 2.4.1.

Lemma 2.4.1. Assume a magnetically controlled spacecraft with diagonal inertia matrix $J = \text{diag}(J_1, J_2, J_3)$. The linearized dynamics of the satellite are controllable if:

- The satellite is not located on the magnetic Equator;
- the following conditions hold: $J_2 \neq J_3, 6J_3(J_3 - J_1) \neq J_2(J_1 - J_2 + J_3)$.

The necessary conditions for the controllability of the nonlinear dynamics are defined in Theorem 2.4.2 (see Bhat (2005) for the proof).

Lemma 2.4.2. The attitude dynamics of a magnetically controlled spacecraft in a closed Keplerian orbit that does not lie in the geomagnetic equatorial plane are strongly accessible and controllable.

2.5 Control theory preliminaries

In this section, we briefly present stability notions, taken from Khalil (1996), and tools necessary for the analysis of the Linear Time Varying (LTV) and Linear Time Periodic (LTP) systems (Yakubovich and Starzhinskii, 1975) which will be used later in the text.

2.5.1 Stability notions

Among several notions of stability existing in the literature, Lyapunov stability is particularly popular. Instead of analyzing all the possible system trajectories, it concerns with the dynamical properties of the system and provides an upper bound within which the motion of a stable system must remain (Khalil, 1996). Floquet theory relies on Lyapunov theorem to provide stability necessary conditions for time-periodic systems.

Input-to-state and input-to-output stability concern with the boundedness respectively of the state and of the output of a system under the action of a bounded inputs. These concepts can be very useful for the analysis of systems under the action of disturbances. Both the above notions are used in the following chapters and are briefly recalled hereafter.

Lyapunov stability

We are going to look at general ordinary differential equations of the following type:

$$\dot{\boldsymbol{x}}(t) = f(t, \boldsymbol{x}(t)) \quad (2.31)$$

where t is the only independent variable. We denote the equilibrium points of the Eq. 2.31 all the $\bar{\boldsymbol{x}} \in \mathbb{R}^n$ such that $f(t, \bar{\boldsymbol{x}}) = 0$ for all $t \geq t_0$. We denote as periodic any solution \boldsymbol{x} to 2.31 for which there exists $T \geq 0$ such that $\boldsymbol{x}(t) = \boldsymbol{x}(t + T)$ for all $t \in [t_0, \infty]$. In the following we will assume $\bar{\boldsymbol{x}} = 0$, as it does not undermine generality. Stability in the sense of Lyapunov is defined as follows:

Definition 2.5.1. A solution $\boldsymbol{x}(t)$ is *Lyapunov stable* if $\forall \epsilon > 0, \exists \delta > 0$ such that if

$\|\mathbf{x}(t_0)\| < \delta$ then $\|\mathbf{x}(t)\| < \epsilon \forall t \geq t_0$, where $\mathbf{x}(t)$ is the solution to

$$\dot{\mathbf{x}}(t) = f(t, \mathbf{x}(t)).$$

Lyapunov's method allows us to determine whether a differential equation is stable without knowing anything about what the solutions looks like, so it is ideal for dealing with nonlinear systems. The method uses a supplementary function $V(t, \mathbf{x})$, called a Lyapunov function, to determine properties of the asymptotic behavior of solutions to a differential equation of the general form of Eq. 2.31.

Definition 2.5.2. A function $\gamma : \mathbb{R}_{\geq 0} \rightarrow \mathbb{R}_{\geq 0}$ is of class \mathcal{G} if it is continuous, zero at zero and non-decreasing.

Definition 2.5.3. A function V is *positive (negative) definite* if there exist a real-valued function $\rho(r)$ such that:

1. $\rho(r)$ is class \mathcal{G} function and
2. $V(t, \mathbf{x}) \geq \rho(\|\mathbf{x}\|)$ [$V(t, \mathbf{x}) \leq -\rho(\|\mathbf{x}\|)$] for all $(t, \mathbf{x}) \in \{(t, \mathbf{x}) : t_0 \leq t < \infty, \|\mathbf{x}\| \leq b < a\}$.

Definition 2.5.4. A real function $V(t, \mathbf{x})$ is said to admit an *infinitesimal upper bound* if $\exists h > 0$ and a continuous, real-valued, strictly increasing function ψ with $\psi(0) = 0$ such that

$$|V(t, \mathbf{x})| \leq \psi(\|\mathbf{x}\|) \text{ for } \|\mathbf{x}\| < h \text{ and } t \geq t_0.$$

Theorem 2.5.1. If a continuous function $V(t, \mathbf{x})$ exist, satisfying:

1. $V(t, \mathbf{x})$ is positive definite,
2. $V(t, \mathbf{x})$ admits an infinitesimal upper bound, and
3. $\frac{\delta V(t, \mathbf{x})}{\delta t}$ is negative (semidefinite) definite

then the solution $\mathbf{x}(t) \equiv 0$ of Eq. 2.31 is (stable) asymptotically stable.

If we can find a V satisfying the Theorem 2.5.1, then we can find stable solutions to the differential equation. Unfortunately, there is no general way to construct V from the differential equation Eq. 2.31. See [Khalil \(1996\)](#) for more details.

Input-Output-to-state stability

As the previous stability concept is defined for input-free system, new stability concept have been developed for input/output systems ([Sontag, 2014](#)).

Definition 2.5.5. A function $\beta(r, s) \in \mathcal{KL}$ if $\beta(0, s) = 0$, it is strictly increasing with respect r for fixed s , it is decreasing with respect s for fixed r , and $\lim_{s \rightarrow \infty} \beta(r, s) \rightarrow 0$.

Given a measurable function $\mathbf{d}(\cdot)$, we define its infinity norm $\|\mathbf{d}\|_\infty \equiv \text{ess sup}_{t \geq 0} \|\mathbf{d}(t)\|$. If $\|\mathbf{d}\|_\infty \leq \infty$, then $\mathbf{d} \in \mathcal{L}_\infty$. Consider a time varying system

$$\dot{\mathbf{x}}(t) = f(t, \mathbf{x}(t), \mathbf{d}(t)) \quad (2.32)$$

where \mathbf{x} is the state and \mathbf{d} is the disturbance. Input-to-state stability is defined as following:

Definition 2.5.6. System $\dot{\mathbf{x}}(t) = f(t, \mathbf{x}(t), \mathbf{d}(t))$ is said to be Input-to-State stable if there exists a function $\gamma_{iss} \in \mathcal{G}$ and a function $\beta_{iss} \in \mathcal{KL}$ such that, for each $\mathbf{d}(t) \in \mathcal{L}_\infty$ and $\mathbf{x}(0) \in \mathbb{R}^n$ the solution of the system satisfies:

$$\|\mathbf{x}(t)\| \leq \max\{\beta_{iss}(\|\mathbf{x}(t_0)\|, t - t_0), \gamma_{iss}(\|\mathbf{d}\|_\infty)\} \quad \forall t \geq t_0 \geq 0.$$

2.5.2 LTP systems and Floquet Stability Theory

Consider a homogeneous continuous-time LTV system represented by (Yakubovich and Starzhinskii, 1975):

$$\dot{\mathbf{x}}(t) = A(t)\mathbf{x}(t), \mathbf{x}(t_0) = \mathbf{x}_0 \quad (2.33)$$

where $\mathbf{x}(t)$ is the state vector. Consider, as a special case of LTV systems, a homogeneous T-periodic LTP system, s. t. $A(t + T) = A(t)$.

Then, the state transition matrix is defined as:

$$\Phi(t + T, t_0) = \Phi(t, t_0)\Phi(t_0 + T, t_0) \quad (2.34)$$

If the state transition matrix is evaluated at the end of a period, $\Phi(t_0 + T, t_0)$, is also called a Monodromy matrix. The theorem below is known as the Floquet-Lyapunov Theorem (or more commonly as Floquet's Theorem) Yakubovich and Starzhinskii (1975):

Theorem 2.5.2. Let $\Phi(t_0 + T, t_0)$ be the state transition matrix of the system in Eq. (2.15) with T-periodic $A_c(t)$. Then, there exist a constant Ψ and an invertible and continuous T-periodic $\Delta(t)$ with integrable piecewise continuous derivatives, such that $\Phi(t, t_0) = \Delta(t)e^{t\Gamma}$ and $\Delta(0) = \mathbb{I}^{n \times n}$.

The eigenvalues of the monodromy matrix, $\Phi(t_0 + T, t_0)$, are called the system's "characteristic multipliers", while those of Ψ in Theorem 2.5.2 are called the system's

“characteristic (Floquet) exponents”. Theorem 2.5.3 below, also adapted from [Yakubovich and Starzhinskii \(1975\)](#) and based on the convergence properties of a matrix exponential, provides a useful stability analysis tool for LTP systems.

Theorem 2.5.3. The solution $\boldsymbol{x}(t) \equiv 0$ of the homogeneous system in Eq. 2.33 with T-periodic $A(t)$ is stable if and only if its Floquet exponents have non-positive real parts, or equivalently, if its characteristic multipliers are within the unit circle.

2.6 Modeling hybrid systems

We briefly recall some fundamental concepts of hybrid systems, following the formalism in [Sanfelice et al. \(2008\)](#). The tools provided by hybrid system theory are employed to construct the controller in Chapter 5.

Hybrid systems are dynamical systems exhibiting both continuous and discrete behavior. By having states that can evolve continuously or discretely, hybrid dynamical systems permit modeling of wide range of systems, with applications in robotics, automotive systems, power systems, biological systems, to list a few. A key motivation for studying hybrid systems lies in their applicability to the robust stabilization of nonlinear systems.

Numerous frameworks for modeling and analyzing hybrid systems have appeared in literature. These includes the works of [Tavernini](#); [Lygeros et al.](#); [van der Schaft and Schumacher](#), among others. Herein, we consider the hybrid framework presented in [Goebel et al. \(2012\)](#), where the continuous dynamics (or flows) of a hybrid system are modeled using differential inclusions while the discrete dynamics (or jumps) are captured by difference inclusions.

A hybrid system \mathcal{H} is defined by the following objects:

- a set $C \in \mathbb{R}^n$ called the flow set;
- a set $D \in \mathbb{R}^n$ called the jump set;
- a flow map $F : \mathbb{R}^n \rightrightarrows \mathbb{R}^n$ (or $f : \mathbb{R}^n \rightarrow \mathbb{R}^n$) which governs the continuous evolution when the state falls in the flow set C ;
- a jump map $G : \mathbb{R}^n \rightrightarrows \mathbb{R}^n$ (or $g : \mathbb{R}^n \rightarrow \mathbb{R}^n$) which governs the evolution when the state falls in the jump set D .

A generic hybrid system $\mathcal{H} = (C, f, D, g)$, with single-valued mapping and differential or difference inclusions, is then defined as:

$$\mathcal{H} : \begin{cases} \dot{\mathbf{x}} = f(\mathbf{x}) & \mathbf{x} \in C \subset \mathbb{R}^n \\ \mathbf{x}^+ = g(\mathbf{x}) & \mathbf{x} \in D \subset \mathbb{R}^n \end{cases} \quad (2.35)$$

where \mathbf{x} is the state, $\dot{\mathbf{x}} = f(\mathbf{x})$ represents the continuous dynamics and $\mathbf{x}^+ = g(\mathbf{x})$ denotes discrete dynamics.

Trajectories of a hybrid system are, conveniently, functions of two parameters: an ordinary time parameter $t \in [0, +\infty)$, which is incremented continuously as flows occur, and a discrete time parameter $j \in \{0, 1, 2, \dots\}$, which is incremented at unitary steps when jumps occur. The conditions determining whether a trajectory of a hybrid system should flow or jump are captured by subsets C and D . The pairs (t, j) parameterize the solutions $\phi(t, j)$ of \mathcal{H} .

The solutions of a hybrid system are defined on an extended time domain set $E \subset \mathbb{R}_{\geq 0} \times \mathbb{Z}_{\geq 0}$, named *hybrid time domain*, by functions that satisfy the conditions suggested by Definition 2.6.2 and are called *hybrid arcs*:

Definition 2.6.1. A hybrid time domain $S \subset \mathbb{R}_{\geq 0} \times \mathbb{N}$ is the union of time intervals $[t_j, t_{j+1}] \times j$, where the sequence $\{t_j\}_{j \geq 0}$ is nondecreasing, with the last interval, if it exists, possibly in the form $[t, T)$, with T finite or $T = \infty$.

Definition 2.6.2. A function $\phi : \text{dom } \phi \rightarrow \mathbb{R}^n$ is a hybrid arc if $\text{dom } \phi$ is a hybrid time domain and, for each map $j \in \mathbb{N}$, $t \rightarrow \phi(t, j)$ is locally absolutely continuous.

Definition 2.6.3. A solution to \mathcal{H} with initial condition $\mathbf{x}(0, 0) \in C \cup D$ is a hybrid arc satisfying:

- For each $j \in \mathbb{N}$ and almost all t such that $(t, j) \in \text{dom}(\mathbf{x})$, of $\mathbf{x}(t, j) \in C$, than $\dot{\mathbf{x}}(t, j) \in F(\mathbf{x}(t, j))$.
- For each $(t, j) \in \text{dom } \mathbf{x}$ such that $(t, j + 1) \in \text{dom}(\mathbf{x})$, if $\mathbf{x}(t, j) \in D$, than $\mathbf{x}(t, j + 1) \in D(\mathbf{x}(t, j))$.

A solution $\phi(t, j)$ is said to be *nontrivial* if $\text{dom } \phi(t, j)$ contains at least one point different from $(0, 0)$, *complete* if $\text{dom } \phi(t, j)$ is unbounded, *Zeno* if it is complete but the

2.7. On-orbit environment

projection of $\text{dom } \phi(t, j)$ onto $\mathbb{R}_{\geq 0}$ is bounded, and *maximal* if it cannot be extended, i.e., it is not a truncated version of another solution.

A hybrid system is well posed if it satisfies the hybrid basic conditions:

Definition 2.6.4. A hybrid system satisfies the hybrid basic conditions if the sets C and D are closed, the mappings F and G are outer semicontinuous and locally bounded, $F(\mathbf{x})$ is nonempty and convex for all $\mathbf{x} \in C$, and $G(\mathbf{x})$ is nonempty for all $\mathbf{x} \in D$.

Definition 2.6.5. If the flow map and jump map are single valued, i.e. $\dot{\mathbf{x}} = f(\mathbf{x})$ and $\mathbf{x}^+ = g(\mathbf{x})$, the hybrid system satisfies a hybrid basic conditions if the sets C and D are closed, and mappings f and g are continuous.

If the hybrid system \mathcal{H} is well posed, it inherits several structural and robustness properties. These properties are necessary to guarantee the asymptotic stability of perturbed solutions and robustness with respect measurement noise.

Since the set $C \cup D$ often does not cover entire \mathbb{R}^n , completeness of solutions and local existence of solutions are sometimes not guaranteed, and a generalization of the standard stability concepts is necessary. Stability of a compact set is defined in the following definition.

Definition 2.6.6. • The set $A \subset \mathbb{R}^n$ is said to be stable if for each $\varepsilon > 0$, there exist $\delta > 0$ such that every to \mathcal{H} with $\|\mathbf{x}(0, 0)\|_{\mathcal{A}} \leq \delta$, $\|\mathbf{x}(0, 0)\|_{\mathcal{A}} \leq \varepsilon$ for all $\mathbf{x}(t, j) \in \text{dom } \mathbf{x}$.

- The set \mathcal{A} is said to be pre-attractive if there exist $\delta > 0$, such that any solution x to \mathcal{H} with initial condition $\|\mathbf{x}(0, 0)\|_{\mathcal{A}} \leq \delta$, is bounded, and, if complete, it satisfies $\lim_{t+j \rightarrow \infty} \|\mathbf{x}(t, j)\|_{\mathcal{A}} = 0$.
- The set \mathcal{A} is said to be Globally pre-Asymptotically Stable (GpreAS), if it is stable, pre-attractive and the attractivity property holds for every possible initial point.
- The set \mathcal{A} is said to be Globally Asymptotically Stable (GAS), if it Globally pre-Asymptotically Stable and every maximal solution is complete.

2.7 On-orbit environment

On-orbit environment model is necessary both for the numerical simulations and facility subsystems sizing. In this section we will discuss the main environmental aspects

affecting attitude dynamics of small satellite in LEO orbit, following the models in [Wertz \(1978\)](#); [Sofyal et al. \(2018\)](#); [Montenbruck et al. \(2002\)](#); [Vallado \(2000\)](#). These can be used to compute the resulting external disturbances torques, which will be assumed to be the only ones affecting the spacecraft, as for the nanosatellites the internal disturbance torques can be neglected ([Sofyal et al., 2018](#)).

The external disturbances torques, coming from the action of the aerodynamic drag, solar pressure and the magnetic field, depends not only on spacecraft position and time, but also on other factors such as sun activity. Hence, for the computation of disturbance torque magnitude, worst-case scenario will be considered.

2.7.1 Magnetic field model

Accurate geomagnetic field model is provided by the International Geomagnetic Reference Field (IGRF). The model consists of a set of coefficients defining the spherical expansion of magnetic scalar potential and it is periodically updated to account for the secular variations. For a rotating planet with a conductive fluid core, a dipole magnetic field is parallel (or antiparallel) to the rotation axis arises. In this way, the geomagnetic field can be approximated by a magnetic dipole currently tilted at an angle of about 11 degrees with respect to Earth's rotational axis.

For a spacecraft in LEO orbit in the neighborhood of the equilibrium point, the magnetic field can be approximated by a periodic signal. For better accuracy, this can be estimated by fitting the output from the IGRF model itself ([Psiaki, 2000](#); [Lovera, 2000](#)). Within the magnetic field periodicity assumption, the resulting state-space system described by Eq. 2.29 is Linear Time Periodic (LTP).

2.7.2 Disturbance torques

The main disturbances acting on an earth-orbiting spacecraft are:

- gravity-gradient torque, arising due to the action of the gravity field;
- aerodynamic drag, result of the interaction between the spacecraft surface and the atmosphere;
- residual magnetic dipole torque, due to the interaction between the spacecraft magnetic dipole and the earth magnetic field;

2.7. On-orbit environment

- solar radiation pressure, arising as a result of momentum exchange between the spacecraft and the electromagnetic radiation of the sunlight.

Gravity-gradient torque

The action of gravity differs across a rigid body: the resulting torque around the CM can be computed if the spacecraft mass distribution is known (Wertz, 1978):

$$\boldsymbol{\tau}_{gg} = 3\omega_o^2(\hat{\mathbf{e}}_{z,b} \times J\hat{\mathbf{e}}_{z,b}) = \frac{\mu}{R_{gd}^3}(\hat{\mathbf{e}}_{z,b} \times J\hat{\mathbf{e}}_{z,b}) \quad (2.36)$$

where $\omega_o = \frac{2\pi}{T_{orb}}$ is the orbital angular velocity, T_{orb} the orbital period, $\hat{\mathbf{e}}_{z,b} = R(q)[0 \ 0 \ 1]^T$, with μ being the gravitational parameter and R_{gd} the geocentric distance. The torque is null for a spherical object, as terms in Eq. 2.36 are parallel. The torque vanishes if the local vertical coincides with the direction of one of the principal axes of inertia.

The magnitude of the maximum torque the spacecraft could experience is computed by Sofyal et al. (2018):

$$\|\boldsymbol{\tau}_{gg}\|_{\infty} = \frac{3}{2}\omega_o^2 \max(\|J_3 - J_2\|, \|J_3 - J_1\|, \|J_1 - J_2\|). \quad (2.37)$$

Magnetic dipole torque

Dipole torque arises when a magnetic dipole \mathbf{m}_{res} exists on-board, which interacts with the geomagnetic field creating a disturbance moment. Dipoles may be generated by electronic instrumentation, especially when there are current loops, and must be accounted for through the design of control algorithm. Main source of on-board magnetic dipole are:

- permanent magnetism in the spacecraft;
- on-board current loops;
- magnetism or currents induced by external fields.

In practice, we can assume dipole magnitude to be proportional to the spacecraft mass (Wertz, 1978), and compute the corresponding torque as follows:

$$\boldsymbol{\tau}_{res} = \mathbf{m}_{res} \times \mathbf{b} \quad (2.38)$$

where \mathbf{b} is the earth magnetic field measured in the body reference frame. The maximum value of the disturbance torque depends on the magnitude of the residual dipole and of the earth magnetic field:

$$\|\boldsymbol{\tau}_{res}\|_{\infty} = \|\mathbf{m}_{res}\| \cdot \|\mathbf{b}_{res}\|. \quad (2.39)$$

Magnetic dipole can be generated on purpose so as to provide useful torque by magnetorquers, which are essentially electromagnets. The generated magnetic dipole depends on the number of coils n_m , vector are of the solenoid A_m and the current flowing through i_M :

$$\mathbf{m}_c = n_m A_m i_m \quad (2.40)$$

To control the current, often a Pulse Width Modulation (PWM) technique is employed.

Aerodynamic drag torque

For a spacecraft orbit altitude in the range 100km-1000km, an estimation of the aerodynamic drag acting upon the satellite is given by the classical fluid dynamics drag equations. The force acting on the spacecraft depends on the air density ρ , a drag coefficient C_D , the area of the surface facing the flow A_{sp} , and the velocity vector of the spacecraft v_0 (Wertz, 1978):

$$\|F_{aero}\| = \frac{1}{2} C_D \rho A_{sp} v_0^2. \quad (2.41)$$

For a circular orbit, $v_0 = \sqrt{\frac{\mu}{a}}$, where a the semi-major axis. The air-density model is inaccurate and can be highly variable due to the solar activity: especially in low orbits this disturbance can become critical for the performance and stability of the satellite. The density of the thermosphere can soar by a factor of 50 during solar maximum, with a corresponding increase in atmospheric drag.

The aerodynamic torque are modeled as the cross product between a force and the distance between the point the force is applied (typically the geometric center) and CM:

$$\boldsymbol{\tau}_{aero} = \mathbf{F}_{aero} \times \mathbf{c}_{aero}. \quad (2.42)$$

For a spacecraft with a shape of a rectangular prism, the infinity norm of the aerodynamic drag can be estimated by (Vallado, 2000):

$$\|\boldsymbol{\tau}_{aero}\|_{\infty} = \frac{1}{2} C_D \rho \frac{A_{sp} \|v_0\|^2 \min(X, Y, Z)}{5} \quad (2.43)$$

where a A_{sf} is 50% higher than the largest spacecraft surface and (X,Y,Z) are the lengths

of the prism sides.

Solar radiation pressure torque

Solar radiation pressure upon any satellite's surface arises due to the exchange of momentum between the object and any electromagnetic field. For a spacecraft in LEO, the torque due to solar radiation pressure has usually the smallest magnitude among the cited ones.

As the aerodynamic torque, solar radiation pressures torques depends on the distance between the force is applied and the center of mass:

$$\boldsymbol{\tau}_{srp} = \mathbf{F}_{srp} \times \mathbf{c}_{srp}. \quad (2.44)$$

The solar radiation torque norm can be computed as follows from [Montenbruck et al. \(2002\)](#):

$$\|\boldsymbol{\tau}_{srp}\| = C_{RP} A_{sf} P_{sol} \left(\frac{1.496}{1.470} \right)^2 \frac{\min(X, Y, Z)}{5} \quad (2.45)$$

where C_{RP} radiation pressure coefficient of the satellite and P_{sol} is the solar radiation momentum flux. The reference area is equal to the one used for the aerodynamic torque.

Part II

Ground testing facility

3

Facility design and overview

In this chapter ¹, Three-Degrees of Freedom Dynamic Testbed for CubeSats facility (see Figure 3.1), developed at University of Bologna, design is briefly described. In the following, key features are listed.

- Designed for nanosatellites: intended to grow in the near future, this platform class is appealing due both to the technological challenges and accessibility.
- Functional testing capabilities: a disturbance-free microgravity environment is provided for dynamical simulations. Design goal was to reduce the residual disturbances magnitude down to a value lower than that of the one acting on nanosatellites on orbit;
- ADCS HIL simulations: facility is equipped with features necessary to simulate on-orbit environment aspects (such as sunlight, magnetic field, ecc) for comprehensive hardware testing.
- Control laws testing: the facility integrates programmable hardware which can simulate ADCS functionality.
- Compliant with CubeSats standard: the proposed design makes possible testing of 3rd part developed CubeSats.

¹The content of this chapter is largely based on [Modenini, Bahu, Curzi, and Togni \(2020\)](#)

-
- Low cost: COTS components were employed, complaint with a cost-cap of 20k Euro.



Figure 3.1: DTC Facility.

To provide functional testing and HWIL simulations, the following subsystems have been developed and integrated:

1. a platform with automatic balancing system, to be installed on three-degrees of freedom air-bearing;
2. a Helmholtz cage for geomagnetic field simulation;
3. a Sun simulator;
4. a metrology vision system for ground-truth attitude generation.

Apart from the latest, the vision system, the other subsystems were developed and integrated as part of author's PhD research.

The facility was design to host CubeSats up to 6U. The satellites hardware and the balancing system are fixed to a platform mounted on the top of the air bearing. However, a single setup cannot be used for across the whole 1U - 6U range. The satellite/platform weight ratio must be maximize, and the balancing masses have to be sized correspondingly. Hence, two different platform for 1U and 3U CubeSats testing have been developed. Both platforms mounts very similar in concept and appropriately sized automatic balancing systems.

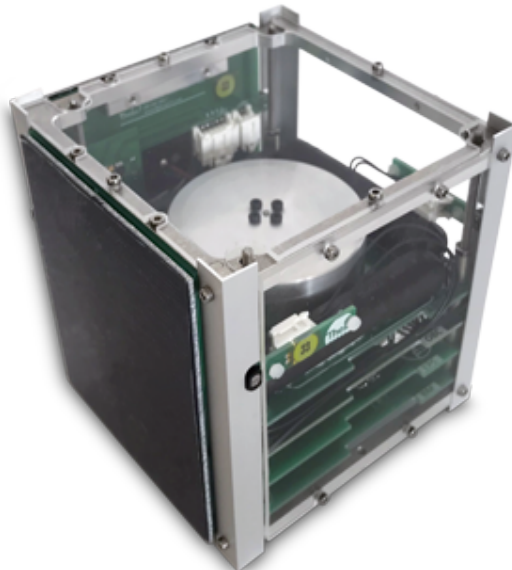


Figure 3.2: Theia ESAT : 1U educational CubeSat (Space, 2020).

Disturbance torques have to be evaluated throughout the whole facility design. The target value, given by the time-varying on-orbit environmental torques, can be estimated based on the satellite and orbit properties: for a CubeSat, it can be as low as 10^{-6} Nm . Models used to compute this target value and through the on-orbit attitude control simulations are described in detail in Section 2.7.

The main disturbance torques in air-bearing based simulators are categorized as in Table 3.1 (Smith, 1964). Though they have been accounted for by design thanks to analytically models, it is not possible to experimentally estimate the effect of the each torque source separately (at exception of the air bearing friction). Hence, the total disturbance

torque acting on the platform is the result of the sum of single contributions, making a disturbance reduction focused design of paramount importance.

Integration of the ESAT, a 1U COTS educational CubeSat by Theia Space (see Figure 3.2), is foreseen by design for the 1U platform. The platform is equipped with a custom triaxial magnetorquers system for magnetic attitude control simulations. The rest of ESAT hardware provides electrical power management, command and data handling and WiFi data communication with the server.

Table 3.1: Disturbance torques in ground testing facilities

From the Air Bearing			
Source	Effect	Mitigation strategy	Verification
Coupling due to air layer	Friction and turbine effect	High end COTS component with very low friction is used	Experimental
From the Environment			
Atmosphere	Aerodynamic Drag	Negligible due to small simulations angular speed	Analytical
Gravity	Gravity torque	Automatic balancing system for static balance	Experimental
	Gravity gradient	Negligible due to small dimension of the testbed	Analytical
From the Equipment			
Anisotropy	Dynamic unbalance	Robust platform design	FEM simulations
Magnetic field	Magnetic torque	Use of amagnetic materials	Experimental
Vibrations	Dynamic torque	Robust mounting	-
From the Test system			
Mass distribution change	Dynamic torques	Negligible in our design	-

All of the facility parts call for experimental verification. In the following sections, the main design choices, implementation details and verification steps undergone are described.

3.1 Helmholtz cage

Magnetic-based attitude control by torque-rods or coils is almost ubiquitously found on board nanosatellites in Earth orbit (Polat et al., 2016), so controlled geomagnetic field is often required for ADCS verification. The envelope of our facility is represented by a triaxial magnetic field simulator, housing a stand with air bearing on the top of it. The Helmholtz cage is a COTS model Ferronato® BH-1300-3-C, featuring three orthogonal pairs of coils with 1300 mm diameter. The cage can generate an arbitrary magnetic field in the range +/-10 Gauss. Magnetic field in-homogeneity is below 1% (5%) in a spherical volume of 404 (586) mm in diameter, concentric with the coil pairs. The nominal field-to-current ratio is $50.5 \mu\text{Tesla/A}$, +/-1%.

This COTS equipment was customized for tracking a time varying reference signal: this is indeed the main application scenario when testing a LEO satellite. The geomagnetic field experienced by the satellite is an almost periodic signal at the half-orbital period (see Section 2.7.1). To provide tracking capabilities, a closed loop system was implemented, making use of AP539, a high precision flux-gate magnetometer, placed inside the pedestal support of the articulated system, see Figure 3.1.

3.1.1 Verification process

To test the effectiveness of the closed loop control, we simulated the geomagnetic field profile experienced by a spacecraft traveling on a circular orbit having 550 km of altitude and 70° of inclination. The magnetic field profile commanded to the Helmholtz cage was computed using the IGRF model: the feedback control allowed us to achieve a matching between the measured and commanded magnetic field below 0.2 % (approx 0.5 mGauss) along the three components B_x , B_y , B_z . Furthermore, it also allowed to verify a-posteriori the homogeneity level stated by the manufacturer, which was indeed retrieved thorough a series of measurements gathered at random locations within the control volume.

3.2 Sun simulator

Most of LEO nanosatellites are equipped with Sun sensors. A Sun simulator was embedded in the facility for Sun sensors testing, aimed at delivering a collimated light-beam resembling the sunlight. Derived from a COTS LED Studio light (Radiante D300,

3.2. Sun simulator

from Photonica, Italy) with a 300W phosphor-coated led as luminous source, the simulator has been equipped with a custom collimating Fresnel lens with 400mm diameter. The distance of the Fresnel lens to the light source has been optimized for maximizing the beam collimation, through a dedicated test campaign.

Usually, a Sun simulator is classified according to three criteria:

- spectral matching
- spatial uniformity
- temporal stability.

For testing a Sun sensor, other parameters are have to be taken into account, such as the collimation of the light beam over a wide area, that shall be kept within 0.53° , i.e. the apparent angular diameter of the Sun at 1AU, and the power flux level ($\approx 1367 \text{ W/m}^2$ at 1 A.U.) at the nominal target distance (i.e. the distance from the LED source to the illuminated target, $\approx 0.75 \text{ m}$ in our case).

Most solar simulators make use of Xenon or metal halide discharge bulbs, which are known to deliver better spectral matching than LED sources. This is achieved, however, at the expense of a lower efficiency, lower lifetime, and a more complicated power supply needed to achieve a stable, flicker-free output. For our simulator, the choice of using a LED source was made, leveraging on its inherently flicker-free output, its high efficiency, and good matching in the visible part of the spectrum. The main drawback is the near absence of output in the IR and UV bands, so that spectral matching with the Sunlight is lost out of the visible band. This is not, however, considered a limiting factor in our application, as most existing nanosatellite Sun sensors are built upon CMOS, CCD, PSD, whose response is maximum within the visible band and falls-off rapidly in the IR and UV wavelengths. On the other hand, photocell-based coarse Sun sensors would be more affected by the lack of IR and UV bands simulation. Note that the response of these sensors is also altered by Earth albedo, which is anyway not modeled in the facility.

By using a LED source, one shall not aim at matching the overall solar irradiance, since a consistent amount of the this is found in the IR and UV bands. Rather, the LED power has been chosen to match the extra-atmospheric solar illuminance (i.e. the photometric, visible flux density), which amounts to about 130.000 lux at 1 A.U.

3.2.1 Optimization and verification process

The validation of the custom design was performed in two steps: first, a test campaign was carried out for adjusting the distance between the Fresnel lens and the LED source to obtain the desired collimation level of the light beam. Then, a second test campaign was performed to assess the temporal stability and spatial uniformity of the collimated beam. Both test campaigns employed as a sensing device a 1.3 MPx monochromatic CMOS camera.

The beam divergence is kept below the 0.53° threshold within a 0.35 m diameter beam. Spatial uniformity was found to be within 10% in a 0.25 m diameter region which is slightly smaller with respect to the target beam size of 0.3 m. Temporal fluctuations were found to be within 1% showing high stability, as expected for a led source. See [Modenini et al. \(2020\)](#) for detailed test campaign description.



Figure 3.3: Detailed view of Sun simulator with collimation device.

3.3 Ground truth vision system

To provide independent ground truth data through dynamic simulations, a vision system is employed. The metrology system based on monocular camera vision was entirely developed in-house. The working principle consists of placing a known visual pattern, a checkerboard, in our set-up, on top of the device under test, which is then imaged using a calibrated camera. Solving the camera pose with respect to the target is done through corner points correspondences: this provides the attitude, which is retrieved as part of the pose solution.

3.4. Testbed platform

The attitude accuracy was verified in dynamic conditions against an independent turntable facility for extremely accurate angular motion simulation, leading to a root mean square error below 0.16° (10 arcmin), one order of magnitude higher than a compact onboard MEMS IMU can provide. As the development of this subsystem was not part of author's work, the reader is invited to see [Modenini et al. \(2020\)](#) for further details.

3.4 Testbed platform

The air bearing platform is aimed at supporting the nanosatellite mock-up, allowing a nearly torque-free rotational motion. The main disturbances affecting such systems are the aerodynamic torques from bearing and from the environment, anisoelastic torques arising from the platform, static and dynamic unbalance torques, and torques due to vibrations and electromagnetic interaction. Such torques must be limited, by design or by active systems, down to a level possibly comparable to the level of disturbance torques expected on orbit. This, in turn, lies typically in the order of 10^{-6}Nm for a 3U CubeSat, which is an extremely low value to be matched in a ground-based facility.

Reduce the unbalance torque due the distance between the centre of mass (CM) and the centre of rotation (CR) is challenging: assuming a total rotating mass (platform with balancing mechanism plus a CubeSat) in the order of 10kg, a matching between the CR and CM shall be achieved up to 10nm level if we want a torque in the order of 10^{-6}Nm . Such a value is well below the reported performance of existing balancing systems. This suggests that substantial efforts must be devoted to platform balancing, and its effectiveness shall be verified a-posteriori by estimating the residual torque acting on the balanced platform.

Furthermore, even if the static unbalance torque is successfully reduced, anisoelasticity gives origin to deformation of the platform which may lead to a consistent disturbance torque. The structural deformation of the rotating platform due to its own weight is difficult to compensate, since making a structure stiffer requires more mass, leading to a vicious cycle. As a countermeasure, an active compensation system was proposed in [Xiang et al. \(2015\)](#); nevertheless, efficient structural design remains a key approach to the problem, and it is also the one followed for our facility.

In summary, platform design must account for three functional subsystems:

- the mechanical structure, supporting the satellite and all the components necessary for the testbed operations, designed to guarantee minimal deformation torque;

- the automatic balancing system (ABS);
- a satellite mock-up, necessary to provide simulator capabilities.

3.4.1 Platform and mass balancing system sizing

The preliminary platform sizing was driven by analytical tools, using available results from medium-thick axisymmetric plates theory (Timoshenko and Woinowsky-Krieger, 1959) to compute the plate deformation under the effect of its own weight. Results of such analysis indicated that a plate alone would get too thick and heavy before having enough stiffness, thus suggesting for a modified configuration. Nevertheless, plate theory also indicates that a plate with clamped edges, i.e. whose rotation is constrained, has a significantly lower bending than one with unconstrained edges (by a factor of about four), keeping all the rest equal. As a result, any structural element that prevents plate's edge rotation, such as lateral walls, would reduce the maximum deformation. Lateral walls were therefore incorporated in the 3U platform design, as discussed in Section 3.4.2.

An tabletop platform, made of aluminium, was designed so as to satisfy following requirements:

- accommodate a 1U/3U CubeSat while guaranteeing 3DoF with large rotations;
- limit the anisoelastic torque;
- minimize the mass and inertia tensor.

As discussed in Section 1.1.3, all the testbed components have to be appropriately sized so as to minimize the total weight. Choice of balancing mass is critical, as it provides gravitational disturbance torque compensation.

The weight on the top of the air bearing is due to various components:

- payload: hardware under testing or a complete satellite mock-up;
- Automatic Balancing System: motors and drives, batteries, inertial measurement unit (IMU), a controller board and balancing masses;
- the mechanical structure: is composed by platform, air bearing and all the parts necessary to the previously listed parts.

The CR position is fixed due to the structure of the air bearing, hence the CM displacement have to be taken into account. It's done in first place through the platform

3.4. Testbed platform

design by choosing components displacement such as to guarantee even mass distribution. Moreover, counterweights are foreseen to reduce larger part of unbalance vector.

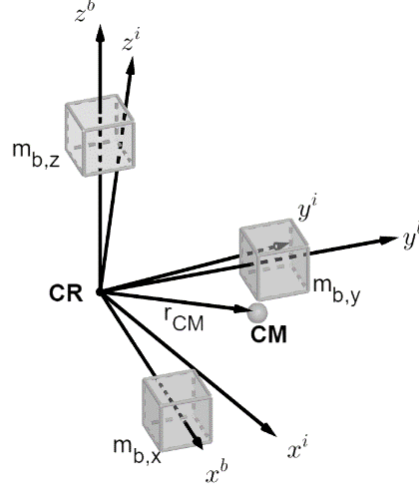


Figure 3.4: Balancing system reference frame (Bahu and Modenini, 2020).

The total mass can be computed by following equation:

$$m_{tot} = m_{payload} + m_{ABS} + m_{st} + m_{b,tot} \quad (3.1)$$

where $m_{payload}$ is the mass of the hardware under test, m_{ABS} is the mass of the electronic components of the balancing system, m_{st} is the mass of all mechanical parts and $m_{b,tot}$ is due to balancing masses. Here m_b accounts only for actuated balancing masses. Fixed one are taken in account by m_{st} term.

As \mathbf{r}_{CM} is a three dimensional vector, we need to provide three independently actuated balancing masses, controlled along non-parallel directions. Let's $\mathbf{r}_{b,i}$ be the position of i-th balancing mass (Kim and Agrawal, 2009):

$$\mathbf{r}_{b,i} = \mathbf{r}_{0b,i} + d_i \hat{\mathbf{u}}_i \quad (3.2)$$

where $\mathbf{r}_{0b,i}$ is initial position of the i-th balance mass actuated along three mutually orthogonal directions, $\hat{\mathbf{u}}_1$, $\hat{\mathbf{u}}_2$ and $\hat{\mathbf{u}}_3$. The amount of shifting balance masses $m_{b,tot} = m_{b,1} + m_{b,2} + m_{b,3}$ and their maximum displacement Δd_{max} determine the maximum CR to CM offset, $r_{CM,max}$, that can be compensated:

$$m_b \Delta d_{max} = r_{CM,max} m_{tot} \quad (3.3)$$

where we assume that the three shifting masses are equal $m_{b,1} = m_{b,2} = m_{b,3} = m_b$.

Conversely, the resolution of the balance masses displacement, Δd_{min} , defines the lower bound of the offset vector it's possible compensate:

$$\Delta r_{CM,i} = \frac{m_{b,i} \Delta d_{min}}{m_{tot}} \quad (3.4)$$

where Δd_{min} is the smallest displacement that \mathbf{r}_{CM} may undergo along the i-th mass shifting direction. The balance masses displacement directions are, in turn, assumed to be mutually orthogonal. Changing Δd_i of any of the three masses will induce a net shift of the overall platform CM equal to (Kim and Agrawal, 2009):

$$\Delta \mathbf{r}_{CM} = \frac{1}{m_{tot}} \sum_{i=1}^3 m_{b,i} \Delta d_i \hat{\mathbf{u}}_i = \frac{m_b}{m_{tot}} \Delta \mathbf{r}_b \quad (3.5)$$

where $\mathbf{r}_b = [\mathbf{r}_{b,1}^T \mathbf{r}_{b,2}^T \mathbf{r}_{b,3}^T]^T$, see Figure 3.4.

3.4.2 3U Platform design

The platform is designed to accommodate a 3U CubeSat. The dimensions are standard and equal to $100 \times 100 \times 340.5$ mm, while the mass cannot exceed 4 kg. Balance masses and their maximum travel determines the maximum CM to CR offset which can be compensated. In case of a 3U CubeSat, the design specifications limits \mathbf{r}_{off} to ± 20 mm on x/y axes and ± 70 m on z axis (Domain, 2009). The larger part of the unbalance vector is compensated by a coarse balancing procedure:

- plane coarse balancing is done by positioning the payload on the top of the platform;
- spare counterweights can be fixed at the bottom of the platform to reduce the unbalance on the z-axis (see Figure 3.5c).

Starting from the guidelines defined in Section 3.4.1, the final design consists of a 12 mm thick octagonal plate with side walls featuring radial elements to enhance flexural stiffness (see Figure 3.5a). The rationale behind the shape choice is a trade-off: ideally, an axisymmetric structure has to be preferred, for having isotropic inertia and stiffness about any axis of inclination. On the other hand, we needed a shape whose lateral walls allow to fix firmly the equipment needed for the automatic balancing system (the top sur-

3.4. Testbed platform

face is occupied by the nanosatellite mock-up). Therefore, we opted for a shape allowing for flat lateral surfaces while not departing too much from an axisymmetric one.

The platform is made of aluminium and for balancing masses brass was used. The total platform mass is about 4.5 kg. The maximum tilt angle allowed without interference with the stand pedestal is $\approx 30^\circ$.

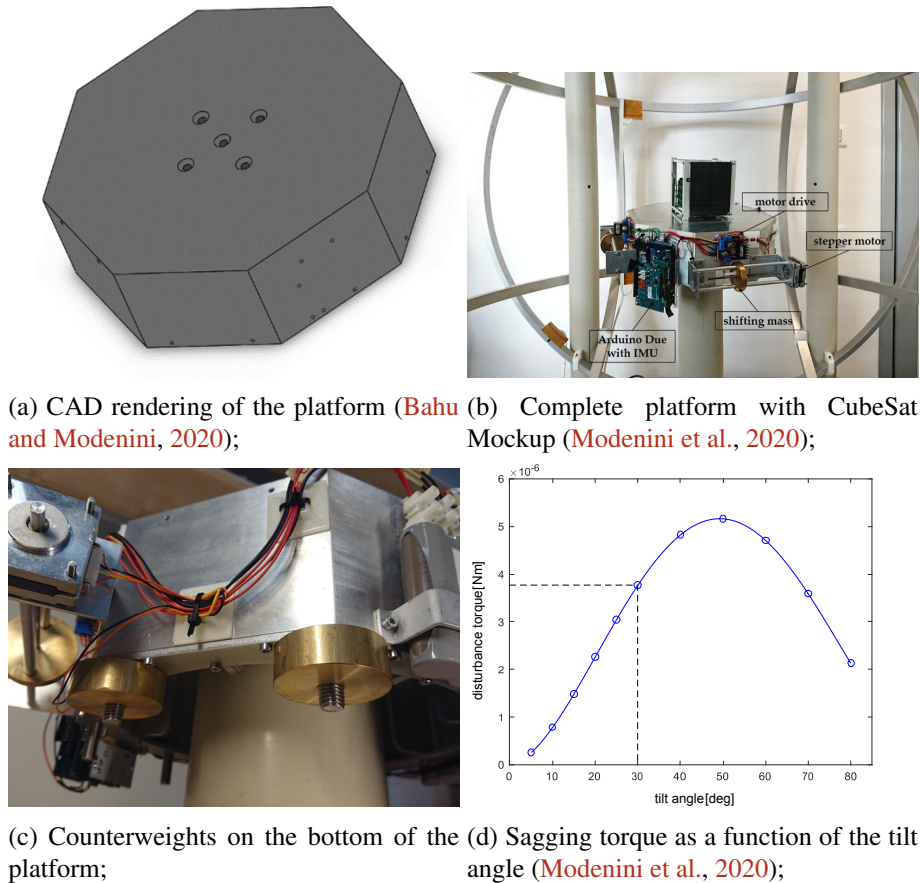


Figure 3.5: 3U Platform.

The final design was also verified through FEM analysis. Starting from the CAD model of the octagonal platform, the geometry was meshed using shell elements. Load condition was prescribed as a uniformly distributed load, simulating the platform own weight, plus concentrated point masses. These last aimed at accounting for the platform deformation due to the weight of the other equipment lying on it.

Simulations were repeated at various tilt angles, by rotating the direction of the load due to weight applied to the geometry. From the computed deformation, the new center of mass of the whole geometry can be located which, in turn, allows to estimate the gravity

torque. Figure 3.5d summarizes the outcome of this process, by displaying the deformation predicted for eleven different tilt angles from 5° to 80° , along with an interpolant curve.

The ABS system is sized to compensate a residual maximum unbalance $r_{CM,max}=2$ mm. Larger initial unbalances are compensated manually using the counterweights and payload manual positioning. Δd_{min} depends on the motors characteristics and actuation system. Since we look for high accuracy positioning, steppers motors of non-captive type were used. The design parameters are summarized in Table 3.2

Table 3.2: 3U platform ABS design parameters

Parameter	Value
m_{tot}	11 kg
m_b	0.11 kg
Δd_{min}	0.002 mm
$r_{CM,max}$	2 mm
$\ \tau_{d,min}\ $	$< 3.7 \cdot 10^{-6} Nm$

For the reported parameters, minimum residual static unbalance torque magnitude is $\|\tau_{d,min}\| = \|\mathbf{r}_{CM} \times m_{tot}\mathbf{g}\| < 3.7 \cdot 10^{-6} Nm$. This is, of course, an ideal lower limit: backlash in mechanical system, axes misalignment, and measurement errors unavoidably deteriorate the system performance.

3.4.3 1U Platform design

Design of the 1U CubeSat platform face slightly different challenges. As the dimension and weight in this case are smaller ($100mm \times 100mm \times 113.5$ mm and 1.33 kg), a more compact platform can be designed. In fact, as the diameter of the air bearing is 150mm and the payload fits within it, almost 45° of tilt is possible. The platform edge lean on the air bearing envelope, means the deformation torque is negligible and gravity torque due to sagging is of no concern in this case.

The ABS is still necessary, but the design is simpler in this case. Thanks to the large weight of the air-bearing hemisphere, equal to 1.475 kg, no counterweights are foreseen. Instead, coarse balancing is done by accurate platform mounting.

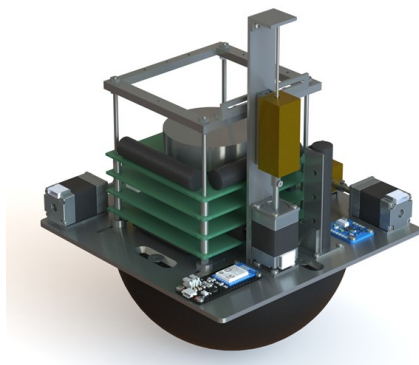
3.4. Testbed platform

The platform was sized to host ESAT CubeSat. Its weight is 0.439 kg; since two magnetorquers are provided only, an additional fastening for a third one have been foreseen.

The balancing system principle is the same as for the 3U platform, and the main design parameters are listed in Table 3.3. Batteries are placed inside the hemisphere, see Figure 3.6b.

Table 3.3: 1U platform ABS design parameters

Parameter	Value
m_{tot}	2.875 kg
m_b	0.1 kg
$r_{CM,max}$	1.33 mm
Δd_{min}	0.002 mm
$\ \boldsymbol{\tau}_{d,min}\ $	$< 3.7 \cdot 10^{-6} Nm$



(a) CAD rendering of the platform;



(b) Counterweights on the bottom of the hemisphere;

Figure 3.6: 1U Platform.

3.4.4 Automatic mass Balancing System hardware

The core of the balancing system hardware is made of Arduino components with the actuation done by three stepper motors. The on-board controller is an Arduino Due for the 3U platform and a smaller M0 Feather by Adafruit for the 1U platform, both capable to run the real-time balancing feedback algorithm. Angular velocities and orientation are provided by Bosch BNO055 Absolute Orientation Sensor. Communication with a server for data collection and control is granted by a Wi-Fi connection.

The motors are driven by dedicated drivers and power supply. The IMU embeds proprietary filtering algorithms whose output is the attitude represented whether through a Roll-Pitch-Yaw (RPY) rotation sequence or as a quaternion. In-plane balancing requires wherever the feedback of the tilt angles or the gravity vector in the body reference frame, as it will be discussed in the following chapter.

Table 3.4: IMU characteristics

Accelerometer	
Zero-g Offset Temperature Drift	3.5 mg/K
Zero-g Offset Supply Volt. Drift	2.5 mg/V
Output Noise Density	$190 \mu\text{g}/\sqrt{\text{Hz}}$
Sensitivity	1 mg
Cross axis sensitivity (max)	2 %
Gyroscope	
Zero- ω Offset Change over Temperature	0.03°/s per K
Zero- ω Offset Supply Volt. Drift	0.1°/s per V
Output Noise rms, BW=47Hz	0.3°/s
Sensitivity	0.0625 °/s
Cross axis sensitivity (max)	3%

The gravity vector is provided by filtered accelerometers measurements or, alternatively, can be computed from the estimated quaternion. Filtering accelerations measurements provides better accuracy in almost-static conditions, as the no angular and linear accelerations affects the measurements. According to the Table 3.4, there are several source of error affecting sensor measurements: even in case of perfect bias calibration a worst-case static measurement error is of 0.2g due to cross-axis sensitivity, which would provide almost 1.15 ° Roll-Pitch pointing errors. Therefore, the sensor was tested in static conditions to check the accuracy of the embedded filtering mechanism. The measurement error was found to be less than 0.025g, which leads to tilt angles estimation errors of about 0.15°.

Tilt angles measurements accuracy provided by attitude estimation algorithm is not stated at-all in the datasheet: an experimental assessment showed worst case static er-

ror of 0.7° RMS. The gravity vector and attitude are estimated jointly by the sensors: however, first one is preferable to be used as a feedback.

Inertia parameters estimation is greatly affected by gyroscope data measurements, which are also retrieved from the IMU. Main limit is the measurement noise, which is partially filtered out by digital filters implemented on-board.

3.5 Discussion

Despite complete turn-key solutions for ADCS functional testing do exist, in-house development may be preferred in some cases due to budget constraints. The drawback of such an approach is that known performance level is hard to be guaranteed. In this chapter, we outlined the design solutions, implementation steps, and verification strategy adopted during the development of one such a facility at the University of Bologna. To simulate various environmental aspects, dedicated subsystems have been developed and integrated.

To provide a guaranteed level of performance, extensive verification campaigns have been done. Results after the commissioning phase demonstrated that our testbed achieves:

1. divergence of the Sun simulator light beam of less than 0.5° , spatial stability under 10%, and temporal fluctuations below 1%;
2. dynamic matching of the magnetic field with error below 0.2%;
3. an attitude determination accuracy of the ground-truth, monocular metrology system less than 10 arcmin rms.

Residual disturbance torque, a fundamental parameter in the ADCS testing facilities, will be addressed in the following Chapter 4.

4

Automatic mass balancing

Reducing the overall torque acting on the testbed is perhaps the biggest challenge for a dynamic ADCS simulator targeted to nanosatellite class¹. In spherical air-bearing design, the large disturbance torque arising due to CM-CR offset have to be specifically addressed. As discussed in Section 1.1.2, an automatic balancing system is indispensable for nanosatellites testing facilities. However, it comes at the cost of greater system complexity, extra hardware, and larger mass of the testbed.

Whenever on-board payload or satellite mockup are equipped with torque-providing actuators, these can be used to feed the system with known control input, making possible estimation of the unbalance offset by input-output data processing. Least-squares formulations and Kalman filters for fully actuated designs have been proposed in [Kim and Agrawal \(2009\)](#); [Schwartz and Hall \(2004\)](#). Alternatively, as the actuated balance mass provides a control action, they can be used as actuators themselves ([Chesi et al., 2014](#); [Prado et al., 1998](#)), which is the approach followed in this work. Since the torque that can be generated by the balance masses is physically confined in the direction perpendicular to the gravity field, the disturbance torque acting on the same subspace can be compensated by a feedback law. This *plane balancing* step is followed by estimation of dynamics parameters and of the residual unbalance along the local vertical.

¹The content of this chapter is largely based on [Bahu and Modenini \(2020\)](#).

4.1. Dynamic model and simulations environment

Since the implementations and algorithms reported in the literature do not provide sufficient gravitational torque reduction for a nanosatellites testing facility (see Section 1.1), a novel balancing procedure has been developed, consisting of the following parts:

- a feedback control law for in-plane horizontal balancing of the platform, discussed in Section 4.2;
- an identification strategy for estimating the residual vertical offset plus system inertia, illustrated in Section 4.3;
- a verification procedure, aimed at estimating the disturbance torque acting on the free oscillating platform after balancing, from inspection of the angular momentum variation, see Section 4.4.

For the above operations, attitude and angular velocity measurements are required. These are greatly affected by errors such as white noise, drift, and random walk. Due to mass, size and budget constraints, a MEMS IMU was employed to provide such measurements (see Section 3.4.4). The limited performance of the sensors is one of the main challenges to overcome, calling for accurate algorithms design/tuning and an extensive verification process.

4.1 Dynamic model and simulations environment

As part of the air bearing testbed validation, a numerical model was implemented in Matlab/Simulink environment. The model allows the user to develop test scenarios for the air bearing testbed and simulate its rotational dynamics. Numerical simulations were performed for both platforms described in Chapter 3, conceived for 1U and 3U CubeSats, by setting the appropriate mass, inertia and geometric parameters.

For the 3U platform, a scenario without payload has been considered. In this setup, $m_{tot} = 6.870$ kg, with the a-priori inertia matrix computed from the CAD model of the platform:

$$J_{CR,3U} = \begin{bmatrix} 5.70 & 0 & 0.17 \\ 0 & 5.97 & 0.01 \\ 0.17 & 0.01 & 9.67 \end{bmatrix} \cdot 10^{-2} \text{ kg/m}^2. \quad (4.1)$$

For 1U platform setup with integrated satellite mockup, the total mass is 2.875 kg and the a-priori inertia matrix is:

$$J_{CR,1U} = \begin{bmatrix} 0.771 & 0 & 0.014 \\ 0 & 0.986 & 0 \\ 0.014 & 0 & 0.758 \end{bmatrix} \cdot 10^{-2} \text{ kg/m}^2. \quad (4.2)$$

The software includes models of sensors, actuators and disturbance torques. The stepper motors mechanical parameters can be found in Section 3.3 and Section 3.2. Saturation on r_{bal} is set to limit the maximum allowable travel, motor step resolution and backlash are set to 0.002 mm and motor dynamics are approximated by a first order system with $\tau=0.01$ s. Limits to the motors maximum speed and acceleration have been determined experimentally, resulting to 2000 *steps/s* and 1000 *steps/s*² respectively.

Sensors readings are corrupted by random measurement noise and bias according to the respective specifications, which proved to be consistent with the measurement variances retrieved from experimental data. The control loop sampling frequency is set equal to the update frequency of the slowest sensor in the IMU, namely 20 Hz.

Dissipative effects acting on the tabletop platform are also modeled. These are mainly of two kinds: the friction of the pressurized air bearing support mechanism, and the aerodynamic drag of the moving parts. The resulting torque dampens the air bearing's angular rate and will eventually return it to rest, unless control torques are applied. Following the model described in [Kwan et al. \(2015\)](#), in the simulation software the torque produced by air friction is computed as a function of the norm of the angular rate. The air bearing friction parameters were estimated by fitting the data of the platform forced to spin around a single body axis.

4.2 In-plane balancing

The goal of the in-plane balancing is to align the body axis \hat{e}_z to the local vertical \hat{g} . If the body axes dynamics are sufficiently slow, the dynamic equations can be decoupled through linearization near the origin, and a controller can be designed by classical control tools, using either gravity vector \mathbf{g} or the attitude estimate as feedback variables: this approach was used at first. To overcome the limits of the linearized model, a nonlinear controller is proposed in Section 4.2.2, which considers a projected control law on the

4.2. In-plane balancing

subspace orthogonal to the gravity direction, i.e. the reachable subspace by the control gravity torque.

4.2.1 Decoupled dynamics and linear control law

Starting from the mathematical model outlined in Section 2.3, and assuming the inertia matrix is diagonal with respect to the chosen body reference frame, $J = \text{diag}(J_x, J_y, J_z)$, the governing dynamics equations are (de Ruiter, Anton H.J.; Damaren and Forbes, 2013):

$$\begin{aligned}
 J_x \dot{\omega}_x + (J_z - J_y) \omega_y \omega_z &= m_{tot} (r_{CR,y} g_z - r_{CR,z} g_y) + \tau_{u,x} \\
 J_y \dot{\omega}_y + (J_x - J_z) \omega_x \omega_z &= m_{tot} (r_{CR,z} g_x - r_{CR,x} g_z) + \tau_{u,y} \\
 J_z \dot{\omega}_z + (J_y - J_x) \omega_x \omega_y &= m_{tot} (r_{CR,x} g_y - r_{CR,y} g_x) + \tau_{u,z}.
 \end{aligned} \tag{4.3}$$

The disturbance torque due to r_{CM} needs to be perfectly compensated by the controller and is considered to be slowly varying. Only the first two equations can be considered, since $\tau_{u,z}$ is null in the target position. Let $[\phi \ \theta \ \psi]^T$ be the RPY attitude representation, where ϕ is the roll angle, θ is the pitch angle and ψ the yaw angle. We define the output error vector $\mathbf{y}_e = [\phi \ \theta]^T$. The components of gravity vector are computed by:

$$g_x = \|g\| \cos \theta \quad g_y = \|g\| \sin \theta \quad g_z = \sqrt{\|g\|^2 - (g_x)^2 - (g_y)^2}. \tag{4.4}$$

If small angles and rates are assumed, the nonlinear dynamics described by Eq. 4.3 can be linearized. In this case, the control problem can be solved by two controllers PID_x and PID_y , designed to stabilize the following second-order dynamic equations:

$$\begin{aligned}
 J_x \ddot{\phi} &= m_{tot} (r_{CM,y} g_z - r_{CM,z} g_y) + \text{PID}_x(\phi) \\
 J_y \ddot{\theta} &= m_{tot} (r_{CM,z} g_x - r_{CM,x} g_z) + \text{PID}_y(\theta).
 \end{aligned} \tag{4.5}$$

These equations can be asymptotically stabilized by PID controllers. For small-angle approximation, $\theta = \frac{g_x}{\|g\|}$ and $\phi = \frac{g_y}{\|g\|}$, and $\mathbf{y}_e = \left[\frac{g_x}{\|g\|} \ \frac{g_y}{\|g\|} \right]^T$ can be used as feedback. This assumption is reasonable, as tilt angles are restricted due to limited angular excursions of the table-top design. Tilt angle estimation through acceleration feedback is expected to be more accurate (see Section 3.4.4), thus it will be employed in the plane balancing experimental assessment in the following chapter.

At the equilibrium point, $g_x, g_y = 0$:

$$\begin{aligned} 0 &= \frac{1}{J_x} (m_{tot} r_{CM,y} g_z + \text{PID}_x \phi) \\ 0 &= \frac{1}{J_y} (-m_{tot} r_{CM,x} g_z + \text{PID}_y \theta). \end{aligned} \quad (4.6)$$

The above equations show that, in steady state, any plane unbalance ($r_{CM,x}, r_{CM,y}$) results to a constant disturbance torque which must be compensated by the integral action. Since the control action is achieved by balancing masses, the planar balancing is preserved until the balancing masses position holds.

4.2.2 Nonlinear control law for planar balancing

The main limitation of the linear approximation is its potential instability in case the feedback stabilizing effect is overcome by large nonlinearities (Khalil, 1996). To cope with slow actuators and unmodelled dynamics, low gains must be chosen possibly leading to large closed-loop time constants and undesired system trajectories. To overcome these issues, it will be shown that for the considered underactuated system a partial attitude control is still possible, and a novel nonlinear control law with proved asymptotic stability in absence of disturbances is proposed. The practical usefulness in the presence of an unbalance torque will be then verified both through simulations and experiments.

Plane balancing can be regarded as a single-axis pointing problem where the pointing direction is coincident with the under-actuated one, since the objective is driving the system to a pure spin condition with the z body-axis aligned to the local vertical direction.

First, the disturbance free single-axis pointing case will be analyzed, i.e. when $\mathbf{r}_{CM} = \mathbf{0}$. To develop a stabilizing control law, let us define a projection operator:

$$P_p = [I - \hat{\mathbf{g}}\hat{\mathbf{g}}^T]. \quad (4.7)$$

It is then possible to decompose the angular speed vector by means of the projection operator as follows:

$$\boldsymbol{\omega}_p = P_p \boldsymbol{\omega}, \boldsymbol{\omega}_g = \boldsymbol{\omega} - \boldsymbol{\omega}_p. \quad (4.8)$$

We now consider the admissible control feedback:

$$\boldsymbol{\tau}_u = -K_p \hat{\mathbf{g}} \times \hat{\mathbf{e}}_z - K_d \boldsymbol{\omega}_p \quad (4.9)$$

4.2. In-plane balancing

where K_d being a positive scalar. The control torque is defined on the plane orthogonal to $\hat{\mathbf{g}}$, so that the corresponding mass displacement \mathbf{r}_b can always be computed through Eq. 2.24.

Consider the candidate Lyapunov function:

$$V = \frac{1}{2}\boldsymbol{\omega}^T J \boldsymbol{\omega} + \frac{1}{2}K_p (\hat{\mathbf{g}} - \hat{\mathbf{e}}_z)^T (\hat{\mathbf{g}} - \hat{\mathbf{e}}_z) \quad (4.10)$$

where K_p is a positive scalar. V is positive definite and equate zero for the system at rest, with $\hat{\mathbf{e}}_z \parallel \hat{\mathbf{g}}$. Along the trajectories of the system, the time derivative of V is defined as follows:

$$\begin{aligned} \dot{V} &= \boldsymbol{\omega}^T J \dot{\boldsymbol{\omega}} - K_p \hat{\mathbf{e}}_z^T \dot{\hat{\mathbf{g}}} = \boldsymbol{\omega}^T (\boldsymbol{\tau}_u - \boldsymbol{\omega} \times J \boldsymbol{\omega}) + K_p \hat{\mathbf{e}}_z^T \boldsymbol{\omega} \times \hat{\mathbf{g}} = \\ &= \boldsymbol{\omega}^T \boldsymbol{\tau}_u + K_p \boldsymbol{\omega}^T \hat{\mathbf{g}} \times \hat{\mathbf{e}}_z = \boldsymbol{\omega}^T (\boldsymbol{\tau}_u + K_p \hat{\mathbf{g}} \times \hat{\mathbf{e}}_z). \end{aligned} \quad (4.11)$$

In deriving Eq. 4.11, we made use of the vector kinematic equation $\dot{\hat{\mathbf{g}}} = -\boldsymbol{\omega} \times \hat{\mathbf{g}}$.

The feedback proposed in Eq. 4.9 makes \dot{V} semi-definite negative, according to:

$$\dot{V} = -K_d \boldsymbol{\omega}_p^T \boldsymbol{\omega}_p = -K_d (\boldsymbol{\omega}_p + \boldsymbol{\omega}_g)^T \boldsymbol{\omega}_p = -K_d \boldsymbol{\omega}_p^T \boldsymbol{\omega}_p. \quad (4.12)$$

To show \dot{V} is semi-negative defined, we shall inspect the closed-loop dynamics to show that in the convergence set $\hat{\mathbf{g}} \times \hat{\mathbf{e}}_z$ must be null, which is the desired z-axis pointing condition. The closed loop dynamics under Eq. 4.9 and within the convergence set $\boldsymbol{\omega}_p = 0$ is:

$$J \dot{\boldsymbol{\omega}} = -K_p \hat{\mathbf{g}} \times \hat{\mathbf{e}}_z - \boldsymbol{\omega}_g \times J \boldsymbol{\omega}_g. \quad (4.13)$$

The right-hand side of the equation is the sum of two vectors orthogonal to $\hat{\mathbf{g}}$, thus any non-null combination of them would lead to $J \dot{\boldsymbol{\omega}} \perp \hat{\mathbf{g}}$. However, this would lead $\boldsymbol{\omega}$ out of the convergence set, as any non-null $\dot{\boldsymbol{\omega}}$ shall lie parallel to $\hat{\mathbf{g}}$. Thus, in the given set, $\dot{\boldsymbol{\omega}} = \mathbf{0}$. For this to hold, $\hat{\mathbf{g}} \times \hat{\mathbf{e}}_z$ must be parallel to $\boldsymbol{\omega}_g \times J \boldsymbol{\omega}_g$, that is, $\hat{\mathbf{e}}_z \parallel J \boldsymbol{\omega}_g$. If the chosen body axes are principle axes of inertia, J is diagonal, and $\hat{\mathbf{e}}_z \parallel J \boldsymbol{\omega}_g$ may occur only if $\boldsymbol{\omega}_g$ is parallel to $\hat{\mathbf{e}}_z$, leading to:

$$\hat{\mathbf{g}} \times \hat{\mathbf{e}}_z = \boldsymbol{\omega}_g \times J \boldsymbol{\omega}_g = \mathbf{0}. \quad (4.14)$$

which proves the desired pure spin around $\hat{\mathbf{e}}_z \parallel \hat{\mathbf{g}}$.

Eq. 4.9 is suitable for reorienting a balanced platform, but when $\mathbf{r}_{CM} \neq \mathbf{0}$, it fails to lead $\hat{\mathbf{g}} \times \hat{\mathbf{e}}_z$ to zero. It is well known that, when full actuation is available, a system subject to a bounded disturbance torque, such as the static unbalance we want to compensate, can be stabilized by adding an integral feedback (Schaub and Junkis, 2009). To this end, we introduce a new state variable:

$$\mathbf{i}_p = \int_0^t K_p \hat{\mathbf{g}} \times \hat{\mathbf{e}}_z dt, \quad (4.15)$$

and modify the feedback law according to:

$$\boldsymbol{\tau}_u = -K_p \hat{\mathbf{g}} \times \hat{\mathbf{e}}_z - K_d \boldsymbol{\omega}_p - K_d K_I \mathbf{i}_p. \quad (4.16)$$

The rationale lies in that, if one can verify that the feedback control drives the integral variable to a finite limit, then $\hat{\mathbf{g}} \times \hat{\mathbf{e}}_z$ must have settled to zero, which in turn requires also $\boldsymbol{\omega}_p = \mathbf{0}$ due to the kinematics of $\hat{\mathbf{g}}$. If the system converges to a pure spin around $\hat{\mathbf{e}}_z \parallel \hat{\mathbf{g}}$, the only non-zero component of \mathbf{r}_{CM} must lie along the vertical axis, which means that planar balancing is achieved.

The validity of the above assumption and the practical effectiveness of Eq. 4.16 have been checked through simulations and experiments, as detailed in following chapter.

4.2.3 Numerical simulations

The linear feedback defined in Eq. 4.5, and the nonlinear one of Eq. 4.16 were implemented in the Simulink simulation environment for performance assessment. Results obtained with accelerometer measurements feedback only will be presented, as it guarantees greater accuracy (see Section 3.4.4). Actuators and sensors models have been included in the environment used for simulations, described in Section 4.1.

The goal of plane balancing procedure is to compensate $\mathbf{r}_{CM,x}$ and $\mathbf{r}_{CM,y}$ by aligning $\hat{\mathbf{e}}_z, i$ and $\hat{\mathbf{e}}_z, b$ axes, or, equivalently, by driving roll and pitch angles to zero. Residual offset vector depends on mass balancing system design (see Section 3.4.1) and tilt angles estimation error (see Section 3.4.4).

Assuming motor resolution as the only static error source, a lower limit of the offset vector can be computed as $\Delta r_{CM,i,3U} = 3.24 \cdot 10^{-8} m$ and $\Delta r_{CM,i,1U} = 6.96 \cdot 10^{-8} m$ per axis for 3U and 1U platforms respectively. The error introduced by the IMU is slightly more difficult to estimate, and will be evaluated by simulations.

Gain selection for the PID controller was performed exploiting existing MATLAB

4.2. In-plane balancing

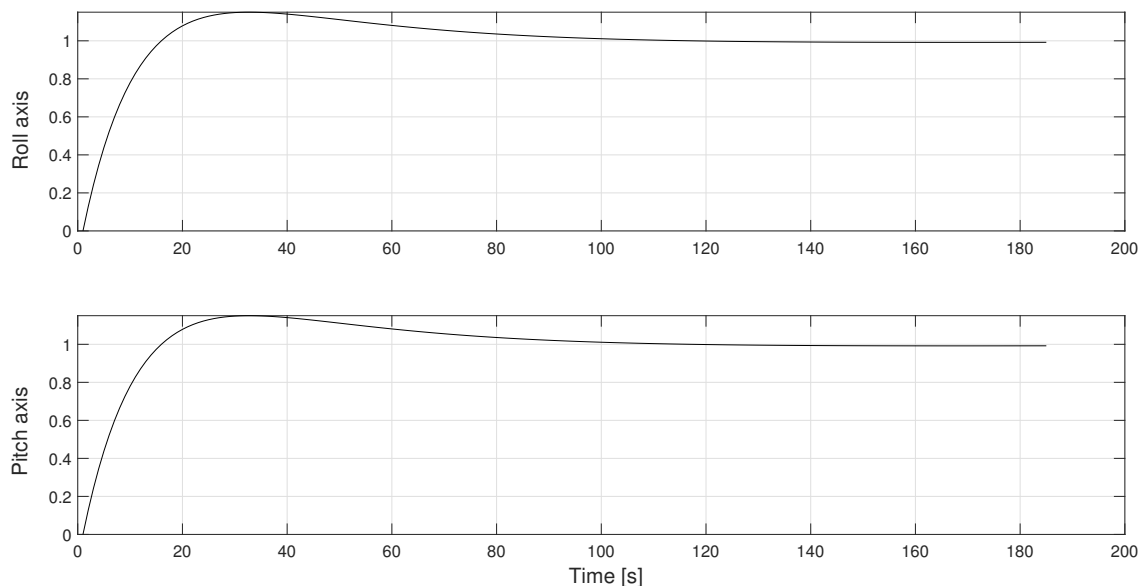


Figure 4.1: Step response of the closed loop linear system.

built-in tools for linear systems tuning. For achieving sufficient disturbance rejection, high phase margin and large settling times are set. Large settling time prevents the motor dynamics, not accounted for by the controller design, to undermine stability. Nonlinear controller gains K_p , K_i , K_d were set equal to the tuned PID controller ones.

By design \mathbf{r}_{CM} is expected to lie within a certain range after manual balancing. Following Tables 3.2 and 3.3, offset vector at time zero $\mathbf{r}_{CM,0} = [1 \ 1 \ -2]^T$ was assumed. Prescribing a negative $\mathbf{r}_{CM,z}$ guarantees a stable pendulum-like motion.

In Table 4.1, gains for a 1 rad/s bandwidth and a phase margin of 80° are summarized. Z-axis gains are reported only for the nonlinear controller, as the third motor is not employed in case the linear one is used. The linear closed loop system response is shown in Figure 4.1. The time constant is ≈ 100 seconds, providing a control input complaint with stepper motor velocity limits.

Simulations were first performed assuming error-free measurements. Initial roll and pitch angles are set to be 30° , which is the maximum allowable excursion for the 3U platform. For small initial angular speed $\|\boldsymbol{\omega}(0)\| < 0.01^\circ/s$, asymptotic stability is provided for both controllers. In Figures 4.2b and 4.2a, attitude errors for 1U and 3U platforms respectively are shown.

Since the qualitative behavior is very similar, in the following only the results for the 3U platform will be presented if not otherwise stated.

Table 4.1: Controllers gains

3U platform gains					
PID and Nonlinear Controller				Nonlinear Controller	
K_{px}	$1.3 \cdot 10^{-2}$	K_{py}	$1.37 \cdot 10^{-2}$	K_{pz}	$2.22 \cdot 10^{-2}$
K_{dx}	$5.62 \cdot 10^{-2}$	K_{dy}	$5.9 \cdot 10^{-2}$	K_{dz}	$9.57 \cdot 10^{-2}$
K_{ix}	$7.53 \cdot 10^{-4}$	K_{iy}	$7.9 \cdot 10^{-4}$	K_{iz}	$13 \cdot 10^{-4}$
1U platform gains					
PID and Nonlinear Controller				Nonlinear Controller	
K_{px}	$2.3 \cdot 10^{-3}$	K_{py}	$2.3 \cdot 10^{-3}$	K_{pz}	$2.1 \cdot 10^{-3}$
K_{dx}	$9.8 \cdot 10^{-3}$	K_{dy}	$10 \cdot 10^{-3}$	K_{dz}	$9.3 \cdot 10^{-3}$
K_{ix}	$1.31 \cdot 10^{-4}$	K_{iy}	$1.33 \cdot 10^{-4}$	K_{iz}	$1.24 \cdot 10^{-4}$

Lower limit of the residual unbalance is in the order of $10^{-8} m$, as expected, and is reached in less than 700 s. RPY angles are shown in Figure 4.3a. The effects of the assumed actuator model are visible in Figure 4.3b where commanded and actual positions of balancing mass are compared on the x axis for both the nonlinear and PID controllers. The difference between the commanded position and the actual one is significant only through the transient, but as soon as the transient expires the error becomes negligible.

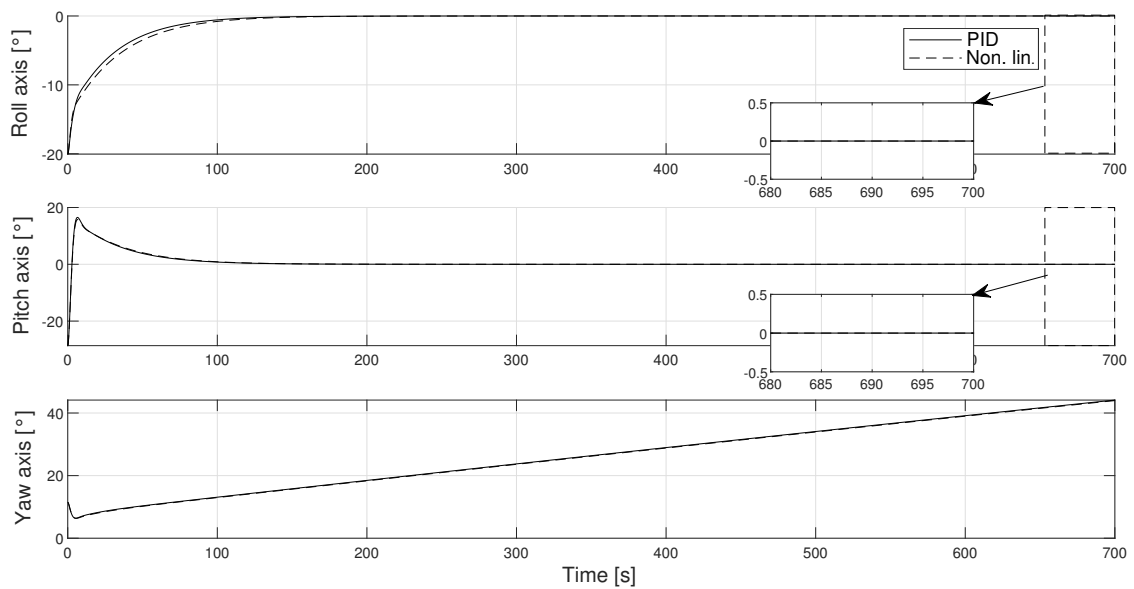
Measurement errors affects mostly static performance. In Figure 4.4a, \mathbf{r}_{CM} evolution is shown. The attitude error is less than 0.5° , with a residual unbalance vector in the order on $10^{-6}m$, equivalent to $10^{-4}Nm$ disturbance torque, too high to guarantee for reliable ADCS testing. By iterating the balancing procedure it is possible to further reduce the residual unbalance: for smaller $\mathbf{r}_{CM,z}$, the attitude error affects less the offset vector compensation. In Figure 4.4b, \mathbf{r}_{CM} evolution is shown in case initial offset $\mathbf{r}_{CM,0} = [1 \ 1 \ -2]^T \cdot 10^{-5}m$ is assumed. For additional balancing iterations, the residual unbalance approach the limit value $\|\mathbf{r}_{CM,i}\| = 2 \cdot 10^{-7}m$. At this point, gyros performance becomes the limiting factor, and even in case of perfect balancing on z axis, disturbance torque is expected to be higher than $2 \cdot 10^{-5}Nm$.

In case slow convergence time is acceptable, nonlinear and PID controllers provides similar performance, although the plane balancing must be repeated several times even for a single balancing procedure, leading to more than 10 minutes of continuous stepper

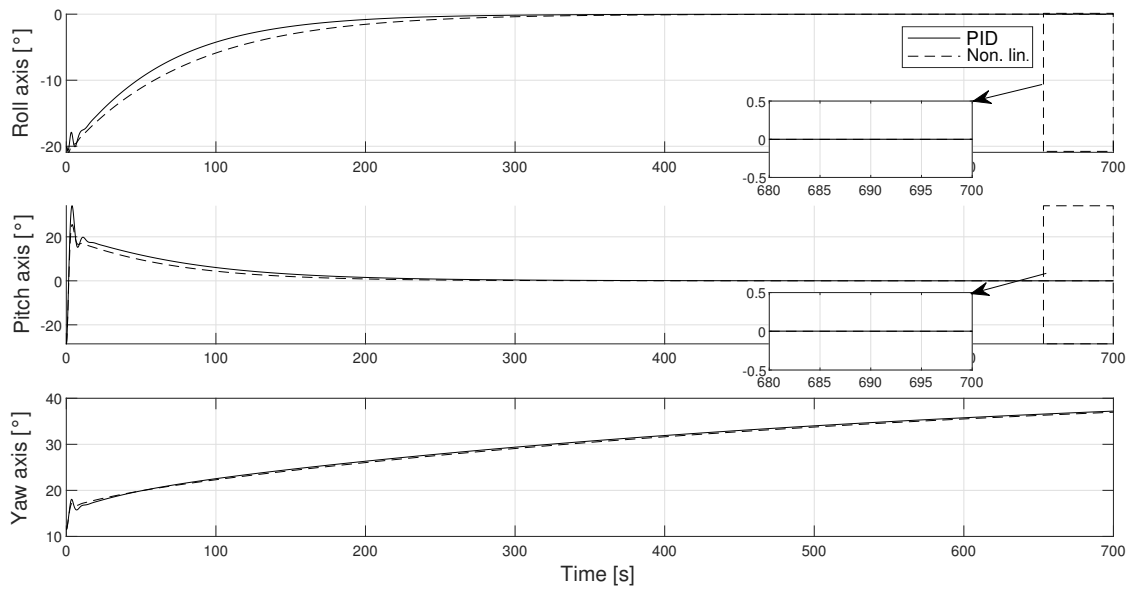
4.2. In-plane balancing

motors operations. With higher gains and lower settling time, stability is provided by the nonlinear controller only. Setting the bandwidth 1.5 rad/s, the steady state is reached in less than 100 seconds in case of nonlinear control, as shown Figures 4.5a and 4.5b. On the other hand, the PID controller leads to system instability, as the motors fails to follow the reference (see Figure 4.5c).

Overall, the nonlinear controller shows better performance for a broad range of initial conditions, therefore, it has been preferred for the subsequent experimental validation phase.

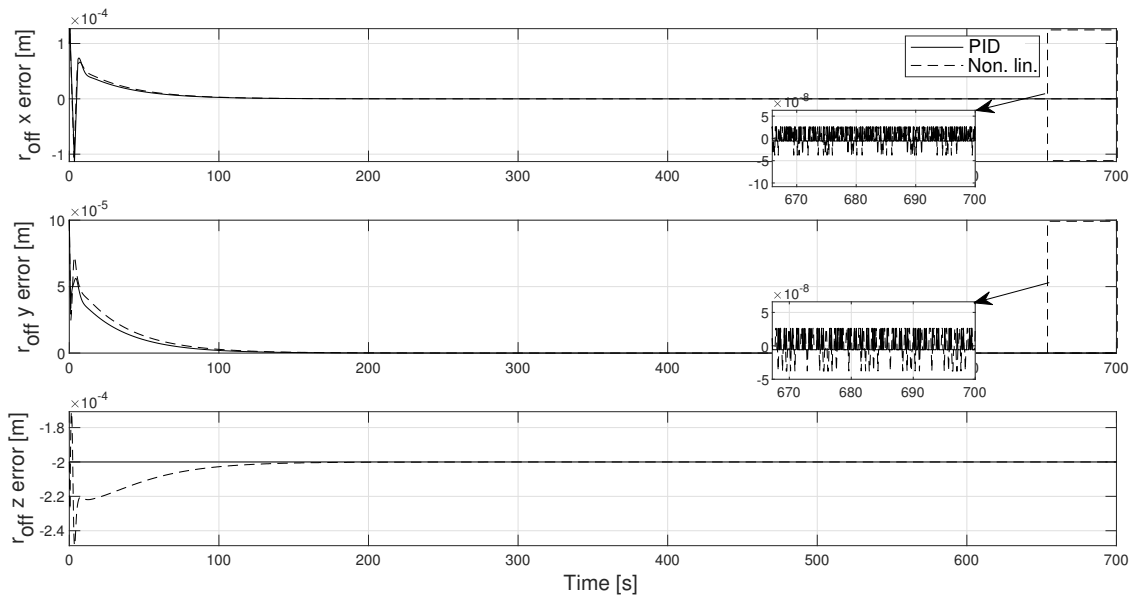


(a) 3U Platform;



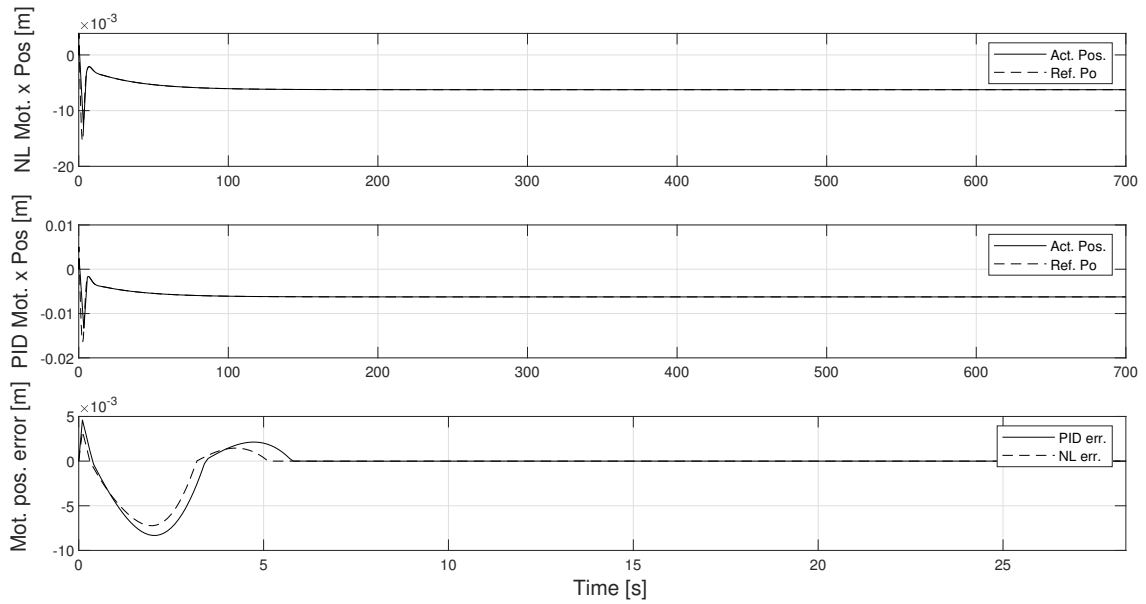
(b) 1U Platform;

Figure 4.2: Plane balancing simulations with ideal measurements



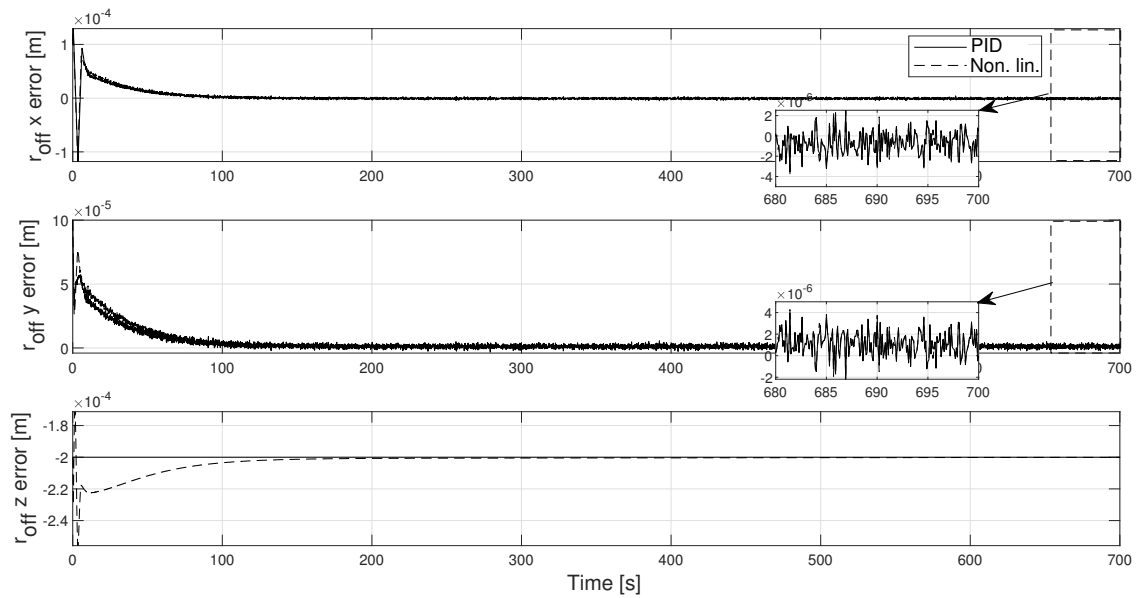
(a) Platform r_{CM} position through plane balancing;

4.2. In-plane balancing

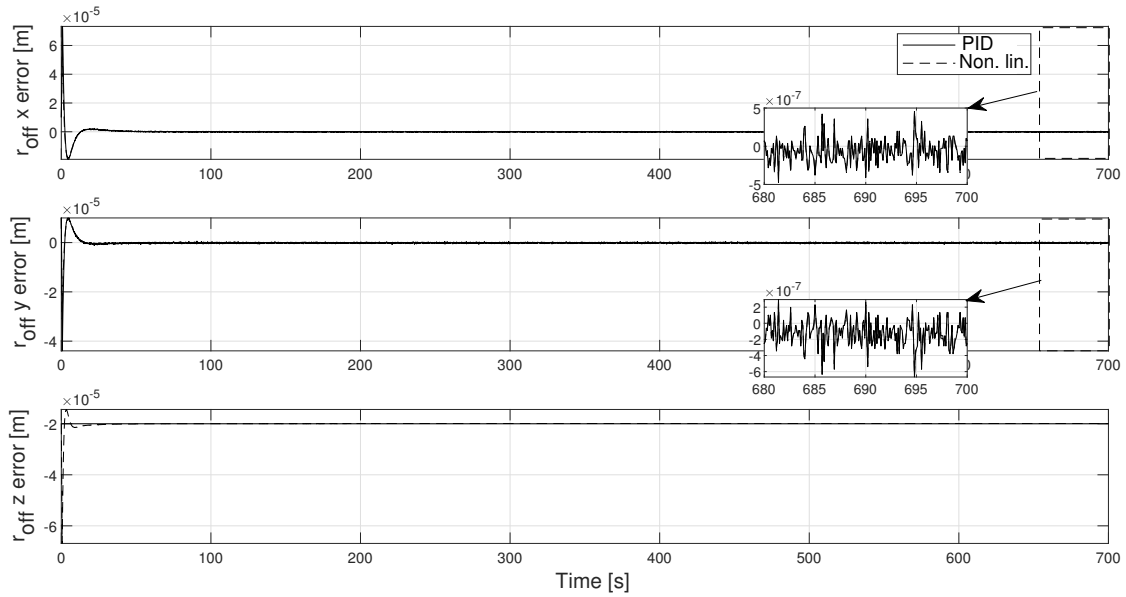


(b) r_b positioning error;

Figure 4.3: Mechanical nonlinearities.

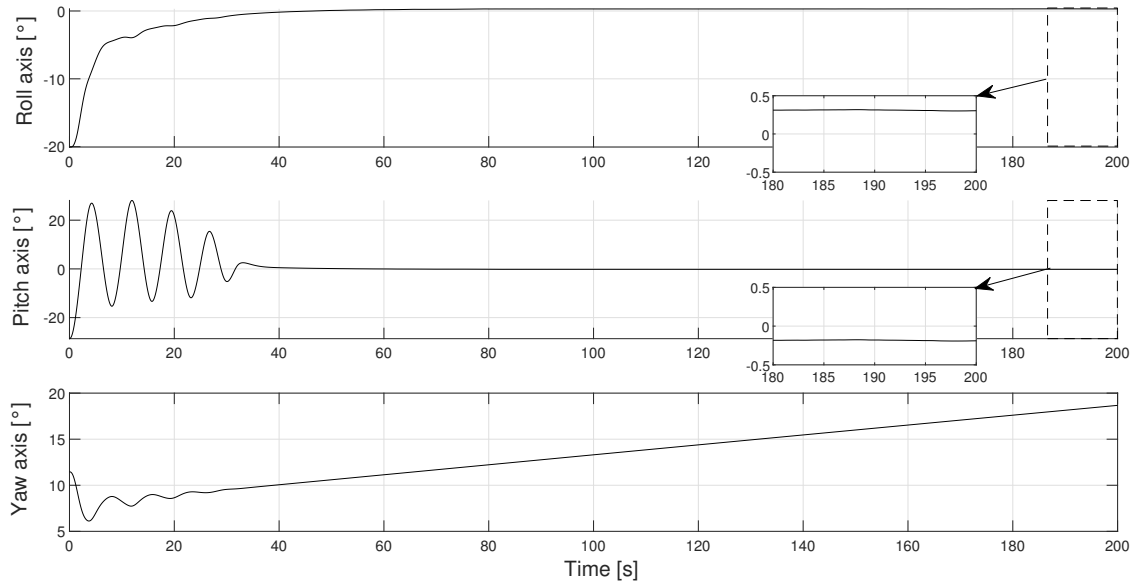


(a) r_{CM} compensation for $r_{CM,0} = [1 \ 1 \ -2]^T \cdot 10^{-4} m$;



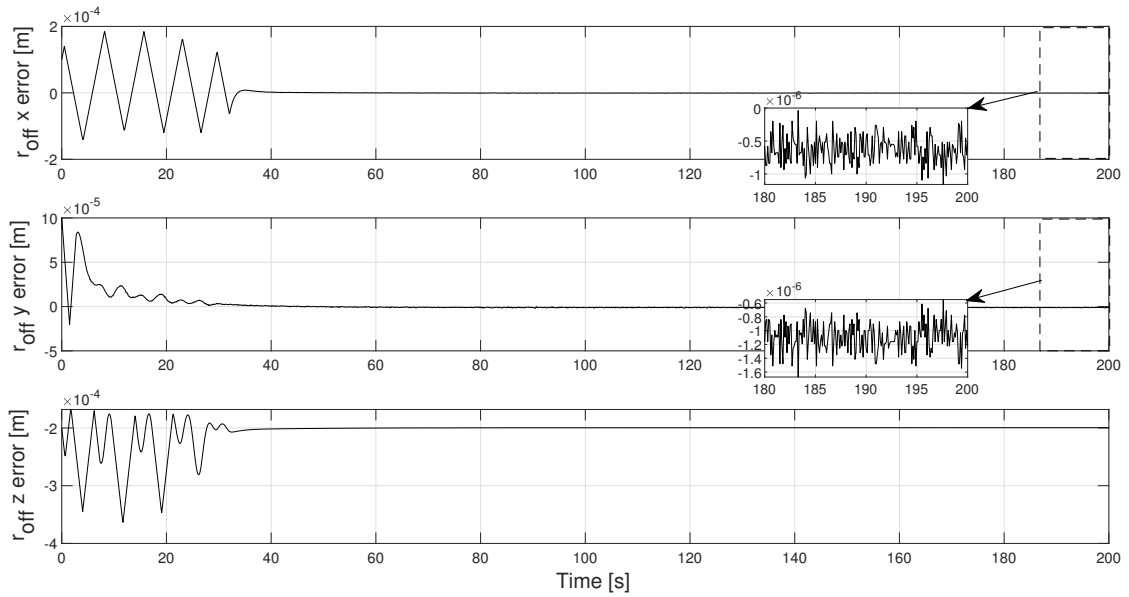
(b) r_{CM} compensation for $r_{CM,0} = [1 \ 1 \ -2]^T \cdot 10^{-5} m$

Figure 4.4: Simulations of plane balancing for 3U platform

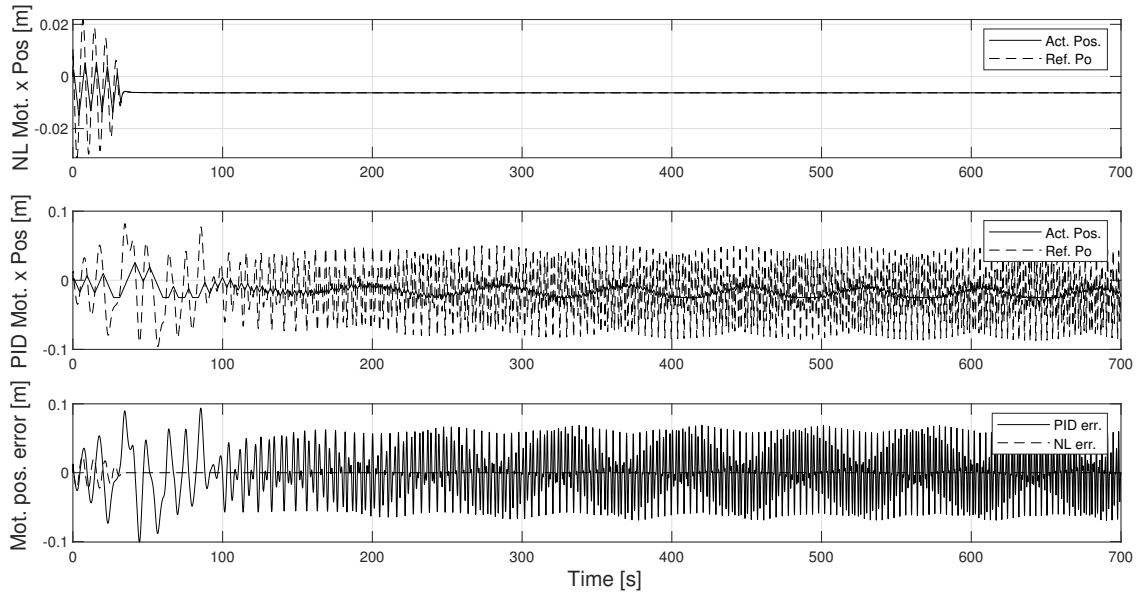


(a) Platform attitude;

4.2. In-plane balancing



(b) r_{CM} compensation;



(c) r_b positioning error;

Figure 4.5: Plane balancing of 3U platform with high gains.

4.3 Estimation of vertical offset and system inertia

The control laws presented in the previous section compensate only two components of the offset vector. The residual unbalance along the local vertical has then to be estimated, jointly with the inertia parameters of the platform as a-priori CAD values could be not sufficiently accurate.

Existing approaches for parameters identification in automatic balancing systems consider whether the joint estimate of the inertia matrix and CR-to-CM offset vector for a one-stage balancing (Xu et al., 2015; Gavrilovich et al., 2015; Kim and Agrawal, 2009), or the estimation of the vertical offset after planar balancing in a dual-stage procedure, assuming the inertia known (Chesi et al., 2014). Our application lies somehow in between those: after the balancing on the x-y plane is achieved, it is possible to rely on the partial knowledge of the unbalance vector for a more accurate estimation of the last component of the offset vector and of the elements of the inertia tensor. Since in our design no external actuation is available other than the shifting masses, the approach used is based on sampling free oscillating rotations. Sampled data are processed offline through a batch least squares (LSQ) algorithm, implemented in MATLAB environment. The only torque acting on the system is therefore supposed to be the gravitational disturbance.

4.3.1 Batch estimation

The identification problem can be cast in a linear least squares estimation framework such as:

$$H\mathbf{x} = \mathbf{b}(\boldsymbol{\tau}_{ext}) \quad (4.17)$$

where $\boldsymbol{\tau}_{ext}$ is the external torque, H is the observation matrix, and \mathbf{x} is the vector of the dynamic parameters to be identified: $\mathbf{x} = [\mathbf{j}^T \mathbf{r}_{CM}^T]^T = [J_{xx} J_{yy} J_{zz} J_{xy} J_{xz} J_{yz} r_{CM,x} r_{CM,y} r_{CM,z}]^T$. However, if no actuation is available, as for a freely oscillating platform, the right-hand side of Eq. 4.17 is identically zero, which would require solving equations for the null space of matrix H . This, in turn, would allow to estimate \mathbf{x} only up to an unknown scaling of all its elements. A possible solution has been proposed in Gavrilovich et al. (2015): the authors show that such a drawback can be overcome when the dynamic parameters are computed with respect to a freely chosen point O , which differs from both CM and CR. Then, the six inertia parameters and three unbalance vector

4.3. Estimation of vertical offset and system inertia

components are estimated jointly. This is not necessary, however, in our case, since we can rely on the partial knowledge of the unbalance vector provided by the planar balancing, after which $r_{CM,x}$ $r_{CM,y}$ are ideally null. As $r_{CM,x}$ $r_{CM,y}$ are known, the estimation problem can be reformulated as a constrained least squares problem:

$$\begin{aligned} H\mathbf{x} &= \mathbf{0} \\ \text{s.t. : } B\mathbf{x} &= \mathbf{c}. \end{aligned} \quad (4.18)$$

This way, the scaling ambiguity is removed. The system dynamics can be written in the matrix framework of Eq. 4.18, as:

$$[\Omega(\dot{\boldsymbol{\omega}}) + [\tilde{\omega}] \Omega(\boldsymbol{\omega})] m_{tot} [\tilde{g}] \begin{bmatrix} \mathbf{j} \\ \mathbf{r}_{CM} \end{bmatrix} = \mathbf{0} \quad (4.19)$$

where Ω is a 3x6 matrix rearranging the elements of $\boldsymbol{\omega}$ or $\dot{\boldsymbol{\omega}}$. The constraints for the known values of $r_{CM,x}$ $r_{CM,y}$ can be enforced by setting:

$$B = \begin{bmatrix} \mathbf{0}_{1 \times 6} & 1 & 0 & 0 \\ \mathbf{0}_{1 \times 6} & 0 & 1 & 0 \end{bmatrix}, \quad \mathbf{c} = \begin{bmatrix} 0 \\ 0 \end{bmatrix}. \quad (4.20)$$

A drawback of this formulation lies in the need of the angular accelerations, which are computed from numerical differentiation of noisy angular rate samples, thus being potentially highly inaccurate. As the dynamics of the free-oscillating body is relatively slow, high frequency random noise can be partially removed by filtering the data through e.g., a SGF. As suggested in [Gavrilovich et al. \(2015\)](#), a different formulation can be obtained by integrating Eq. 4.20. In this case angular accelerations are no more required and data samples integration gives some degree of robustness with respect to random noise:

$$\left[\Omega(\boldsymbol{\omega}^b) + \int [\tilde{\omega}] \Omega(\boldsymbol{\omega}^b) \Big|_{m_{tot}} \int [\tilde{g}] \right] \begin{bmatrix} \mathbf{j} \\ \mathbf{r}_{CM} \end{bmatrix} = \mathbf{0}. \quad (4.21)$$

In collecting data for solving Eq. 4.21 one should trade-off between two counter-opposing requirements: on one side, collecting as many data as possible shall enhance the parameter observability. On the other hand, too long time frame may lead to a degraded

estimate, due to the increasing impact of the unmodeled torques. The performance of the two alternative solutions are compared through simulations in the following section.

4.3.2 Numerical simulations

The estimation of the residual unbalance vector component and inertia parameters relies on data collected from simulation of free oscillations processed through a batch LSQ estimator. The two formulations introduced in previous section, namely the standard formulation with the angular rate filtered through SGF, Eq. 4.19, and the derivative-free, integral formulation, Eq. 4.21, are compared. They are referred to as LSQ-SGF and LSQ-INT, respectively. In general, parameters observability from free oscillations is enhanced when the motion features high accelerations and angular rates, as it guarantee better signal/noise ratio.

Sample outputs from the two algorithms for 3U platform are depicted in Figure 4.6, obtained assuming $\|\mathbf{r}_{CM}\| = 5 \cdot 10^{-5} m$. $r_{CM,x}$ and $r_{CM,y}$ are assumed to be null. The sampling time is of 0.05 seconds. Clearly, LSQ-SGF outperforms LSQ-INT: estimation errors on the principal inertia moments are around 1% for the former, while can be as high as 5% for the latter. Remarkably, both algorithms lead to an estimation error for $r_{CM,z}$ in the order of $10^{-6}m$, which would possibly lead to unacceptably high disturbance torque. This result indicates that, due to the measurement errors and unmodelled dynamics, multiple iterations may be necessary before sufficiently accurate results can be achieved. As shown in Figure 4.7, very similar results are obtained for the 1U platform, hence only the bigger 3U will be considered hereafter.

If the offset estimated with a first iteration is compensated by adjusting accordingly the position of the balancing masses, an additional, refined balancing iteration can be attempted. In doing so, however, we verified that the LSQ estimation as proposed in Eq. 4.19 and in Eq. 4.21 is no more effective when trying to estimate jointly the inertia and the residual unbalance. On the other hand, assuming the inertia known, additional constraints can be included to Eq. 4.20 for improving the estimate of the residual unbalance $r_{CM,z}$ only. An iterated parameter estimation stage can thus be envisaged: in a first iteration, the LSQ batch filter estimates both inertia and unbalance vector; for successive iterations, after the plane balancing is repeated, an LSQ fed with the inertia matrix estimated through the first stage can be employed for refined $r_{CM,z}$ estimation.

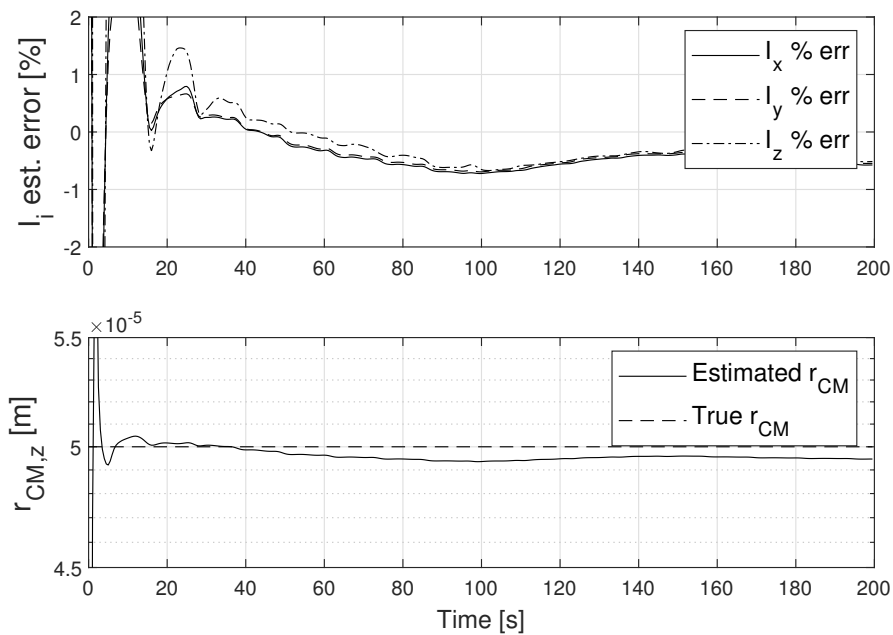
The iterative approach improves the $r_{CM,z}$ estimation accuracy, with an error in the order of $10^{-8} m$, as shown in Figures 4.8a and 4.8b. The inertia matrix is assumed to be

4.3. Estimation of vertical offset and system inertia

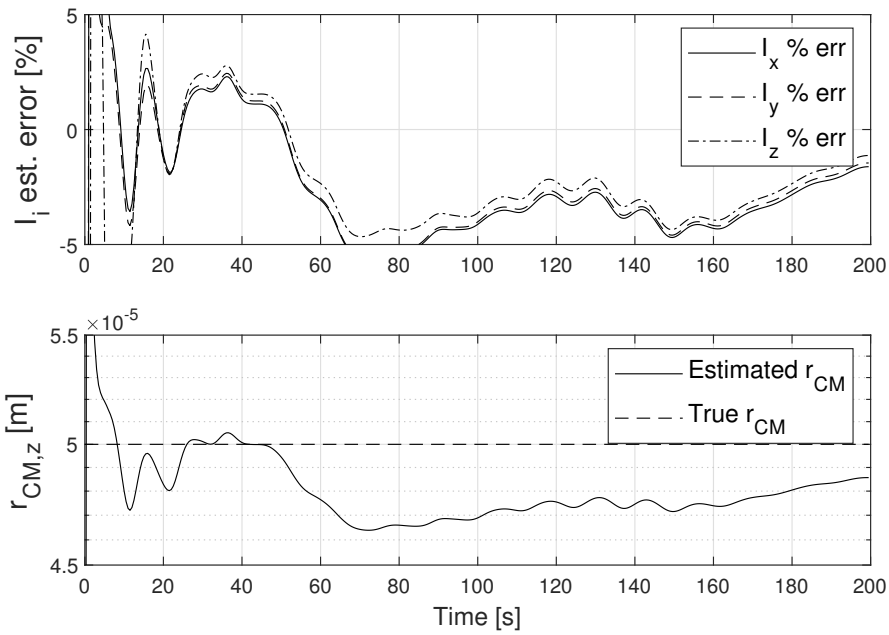
known with an uncertainty of 2 %.

To verify the performance of the whole procedure, for iterative simulations $\|\mathbf{r}_{CM,xy}\| = 2 \cdot 10^{-7} \text{ m}$ is set, as the expected lower limit of the plane balancing. As a result, $r_{CM,z}$ estimation accuracy drops down to $1 \cdot 10^{-7} \text{ m}$ (see Figure 4.8c).

In summary, the outcome of the simulations in Sections 4.3.2 and 4.2.3 suggest that several balancing iterations, from coarser to finer, are necessary for achieving adequate performance: usually after three iterations the disturbance torque due to the unbalance is reduced down to $2 \cdot 10^{-5} \text{ Nm}$, with no further improvements.



(a) LSQ-SGF;



(b) LSQ-INT;

Figure 4.6: 3U parameters LSQ estimation comparison.

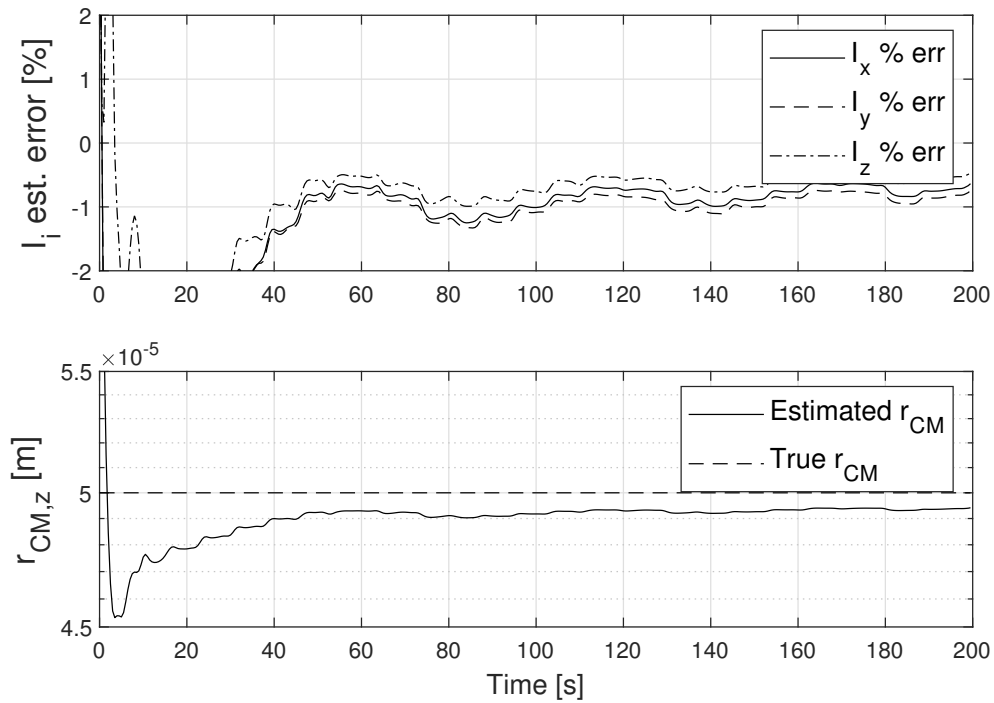
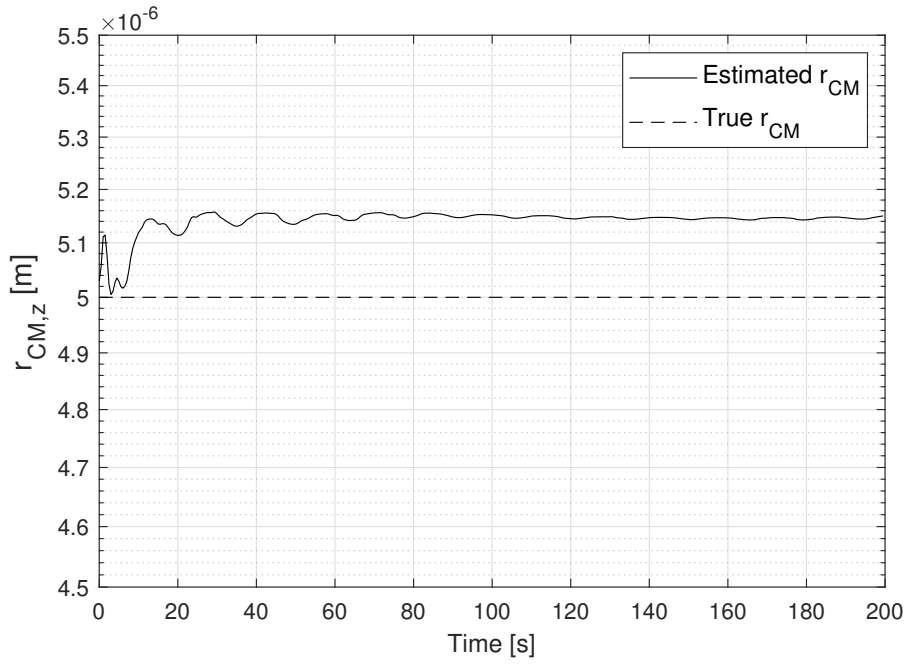
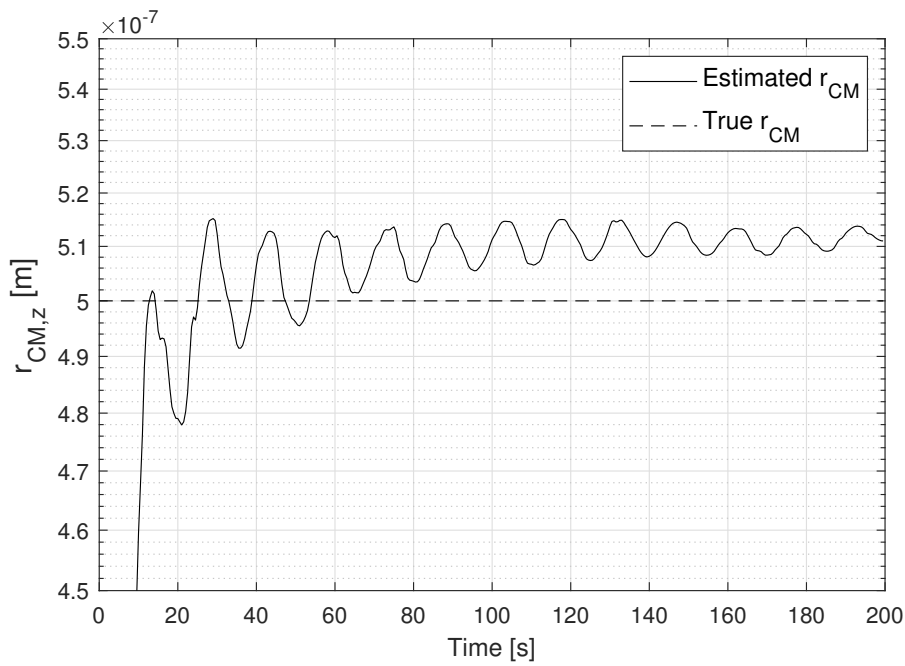


Figure 4.7: 1U parameters estimation by LSQ-SGF

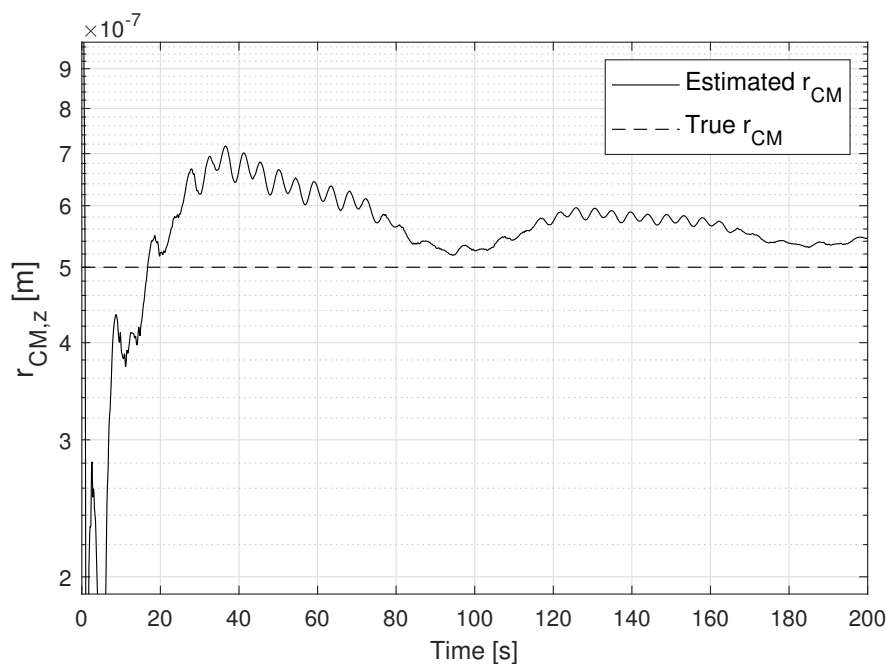
4.3. Estimation of vertical offset and system inertia



(a) Fine estimation for $r_{CM,z} = 5 \cdot 10^{-6} m$;



(b) Fine estimation for $r_{CM,z} = 5 \cdot 10^{-7} m$;



(c) Fine estimation for $r_{CM,z} = 5 \cdot 10^{-7} m$ in case of plane balancing error;

Figure 4.8: Numerical simulation of the $r_{CM,z}$ estimation by constrained LSQ.

4.4 Disturbance estimation

For small angular speed, aerodynamic torque and torque due to air-bearing friction are negligible. The torque due to the interaction between the platform residual magnetic dipole and the Earth magnetic field can be compensated thanks to the available Helmholtz cage. Within these assumptions, unbalance can be considered as the main contributor to the overall disturbance, hence estimating the total torque acting on the platform is equivalent to verify the effectiveness the balancing procedure. However, independently from evaluation approach, accurate inertia matrix estimate must be provided.

To evaluate the torque acting on the platform, one can inspect the variation of the kinetic energy: indeed, for a perfectly balanced and dissipation-free system, the kinetic energy E_{kin} should be constant in time. Kinetic energy can be easily evaluated from the gyroscope measurements, provided the knowledge of the inertia matrix, through the formula $2E_{kin} = \boldsymbol{\omega}^T J \boldsymbol{\omega}$. The periodic variation due to the pendulum-like motion of the platform can be decoupled from the slow exponential decay due to the air-bearing friction. However, the disturbance torque due to the residual unbalance cannot be directly estimated from the kinetic energy variation, and thus can be used only as additional tool

4.4. Disturbance estimation

for fast qualitative balancing accuracy evaluation.

The disturbance torque acting on the system can be instead estimated from the variation of the angular momentum, as per the dynamic equation:

$$\boldsymbol{\tau}_d = J\dot{\boldsymbol{\omega}} + \boldsymbol{\omega} \times J\boldsymbol{\omega}, \quad (4.22)$$

where torque due to the unbalance can be considered as the main contributor to the overall $\boldsymbol{\tau}_d$.

Eq. 4.22 requires differentiation of the angular rate measurements, which we performed using Savitzky-Golay filtering. The choice of data pre-filter is justified by the very slow dynamics which is expected in case of small residual unbalance, so that high frequency measurement noise can be effectively removed.

Numerical simulations showed this approach to be reliable for estimating torques down to the order of $10^{-6} Nm$. In case of smaller torques, the error due to the measurement errors and inertia matrix uncertainty renders the estimation unreliable. As an example, in Figure 4.9 the estimated disturbance torque computed according to Eq. (27) against the true one is compared, for $\mathbf{r}_{CM} = [4 \ 4 \ 14]^T \cdot 10^{-8} m$ and with inertia moments uncertainty of 1%.

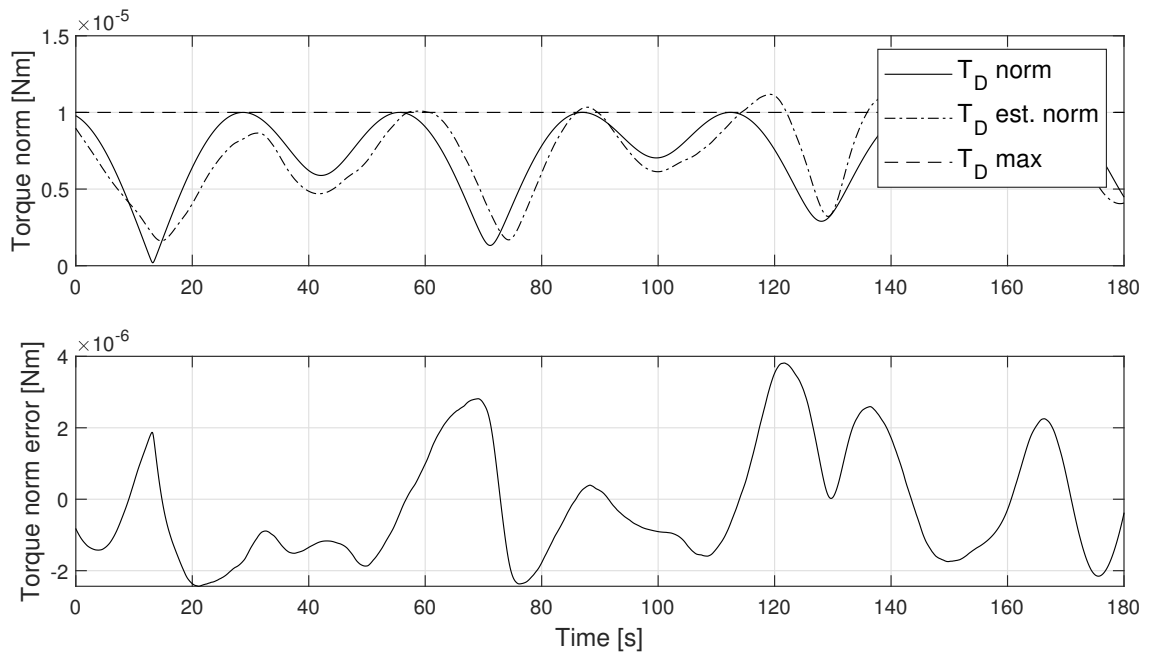


Figure 4.9: Numerical simulation of the residual disturbance estimation after balancing (Bahu and Modenini, 2020).

4.5 Experimental verification

The proposed balancing procedure and disturbance torque estimation algorithm have been verified through experiments using the 3U testbed platform described in Chapter 3. The first step, plane balancing, runs in real-time onboard the microcontroller. The parameter estimation, instead, is performed offline, by collecting the free-oscillation data through the IMU, with sampling frequency 20Hz. Thanks to a Wi-Fi link, the data collected are sent to a desktop computer for processing.

As suggested by the numerical simulations, an iterative procedure has been found to be necessary to guarantee good balancing performance. In our experiments, each balancing iteration consists of an in-plane balancing, followed by a parameter estimation stage.

4.5.1 Platform balancing

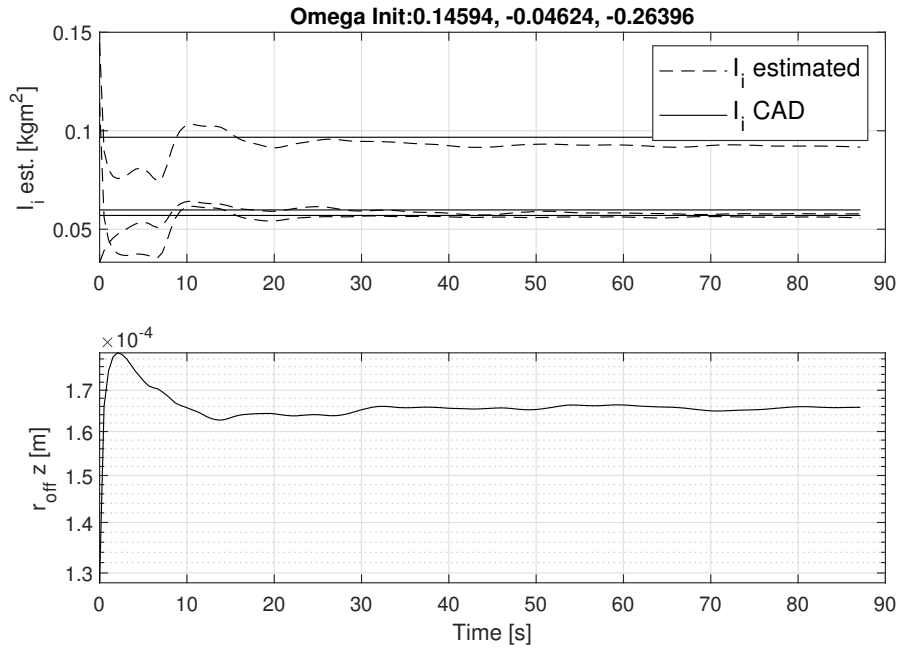
For the in-plane balancing, the nonlinear control law in Eq. 4.9 is employed. Initial conditions for the experiment consist of the platform manually positioned at a rest, hence tilted, attitude. Control gains are the one summarized in Table 4.1.

In the first iteration, inertia parameters estimation is performed through the LSQ-SGF technique. As outlined in Section 4.3, zero unbalance on x-y plane is assumed. This assumption is used as a constraint in the least squares homogeneous equation. Since inertia matrix identification benefits from a high unbalance torque, which excites wide oscillations, a large unbalance on z-axis shall be used. Free oscillations of the platform are then sampled, starting from initial angular speeds applied manually to the platform. Collected data are processed through the LSQ filter, which generally guarantees convergence in less than 100 seconds. Figure 4.10a depicts the estimated principal moments of inertia of the 3U platform, which are compared to their a-priori values computed from the CAD model, showing a mismatching of about 5%.

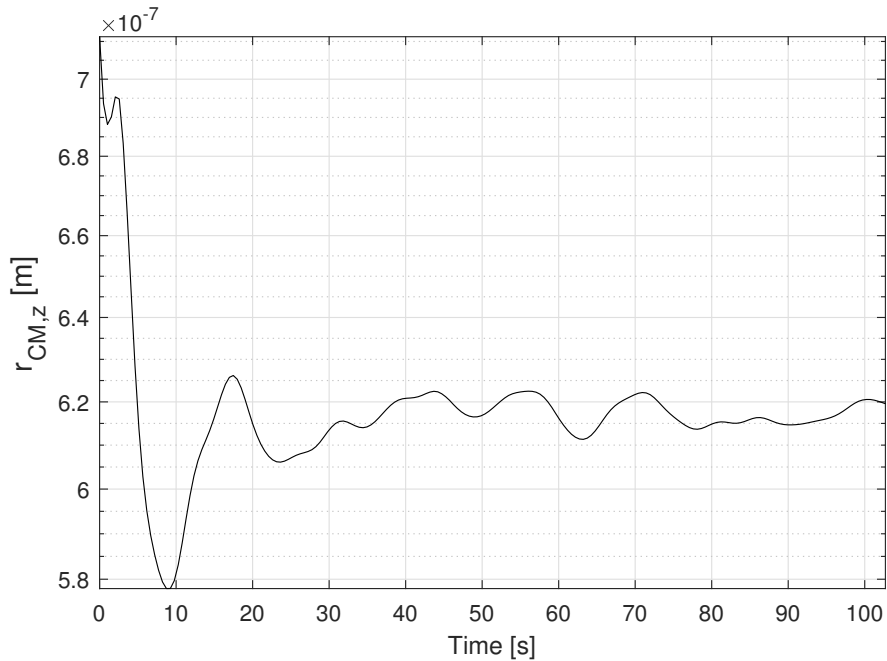
The unbalance vector components are compensated, and a new iteration begins. Plane balancing is repeated and residual $r_{CM,z}$ estimated, this time assuming the inertia known and set equal to the first iteration estimate. The procedure can be further iterated, as long as the i-th $r_{CM,z}$ estimate is smaller than the (i-1)-th one, meaning that the unbalance vector is being reduced. In case no significant difference in the estimated value is found, the balancing is ended, and the residual disturbance torque estimated to validate the balancing procedure. Inertia parameters estimation for the 1U platform is shown in

4.5. Experimental verification

4.11a. In this case no reliable CAD estimation values are available. The overall process is summarized in Fig. 4.12.

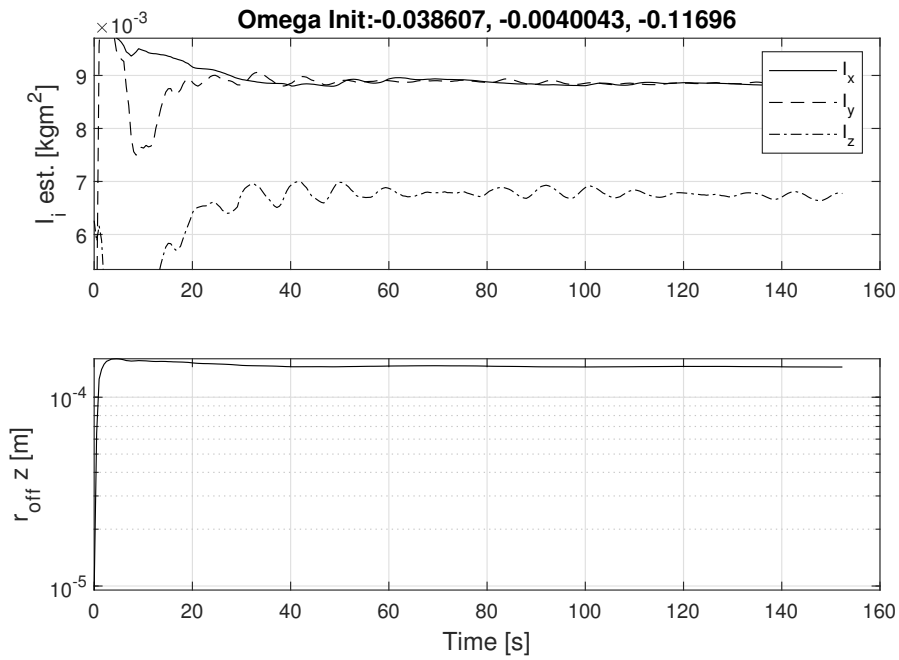


(a) Experimental LSQ estimation of 3U platform parameters (Bahu and Modenini, 2020).;

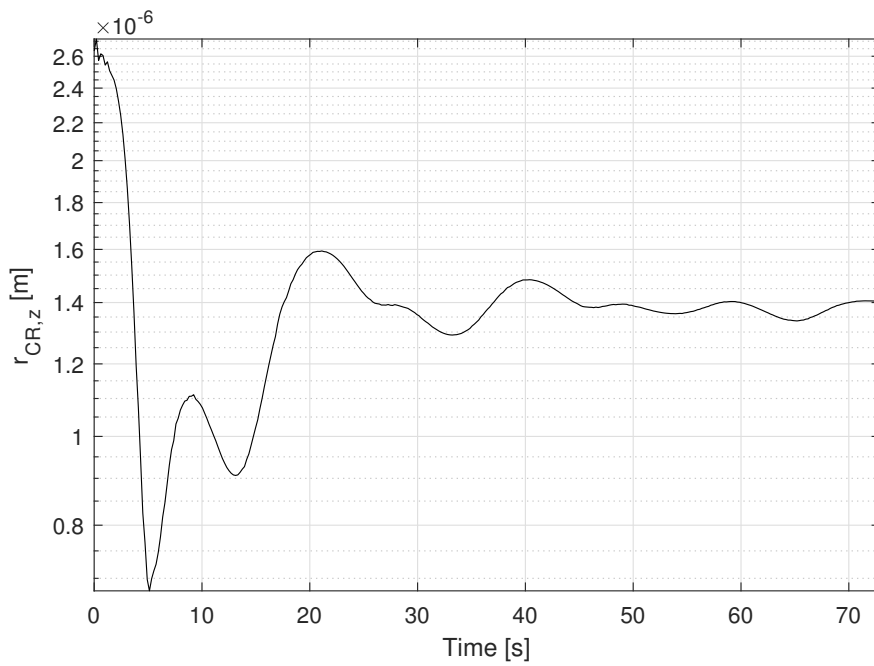


(b) Fine $r_{CM,z}$ 3U platform experimental estimation (Bahu and Modenini, 2020);

Figure 4.10: 3U parameters experimental estimation.



(a) Experimental LSQ estimation of 1U platform parameters;



(b) Fine $r_{CM,z}$ 1U platform experimental estimation;

Figure 4.11: 1U parameters experimental estimation.

4.5. Experimental verification

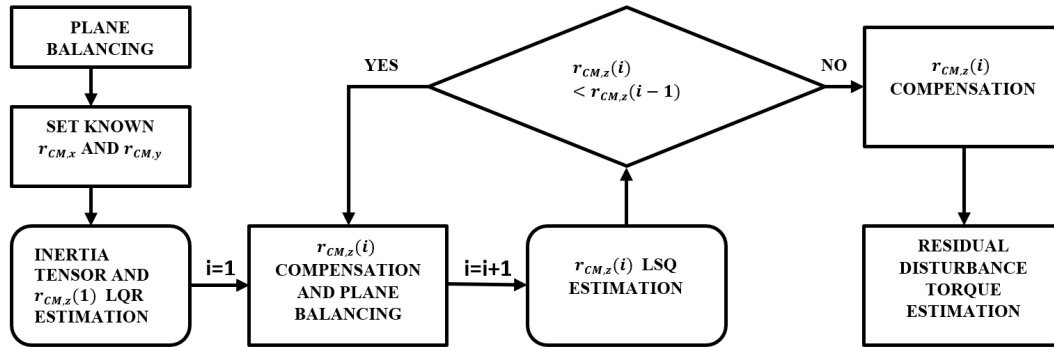


Figure 4.12: Iterative balancing procedure (Bahu and Modenini, 2020).

Table 4.2: Convergence history of the parameters identification step.

Iteration	3U principal inertia moments [kgm^2]	3U es- timated vertical offset [m]	1U principal inertia moments [kgm^2]	1U es- timated Vertical offset [m]
1		$1.66 \cdot 10^{-4}$		$4.15 \cdot 10^{-4}$
2	$[5.57 \ 5.78 \ 9.17] \cdot 10^{-2}$	$2.50 \cdot 10^{-6}$	$[8.84 \ 8.92 \ 6.77] \cdot 10^{-3}$	$7.41 \cdot 10^{-6}$
3		$6.19 \cdot 10^{-7}$		$1.34 \cdot 10^{-6}$

It was found through experiments that after three balancing iterations the oscillation period becomes extremely long and the residual $r_{CM,z}$ estimation does not improve any further below a threshold of $\approx 7 \cdot 10^{-7}m / \approx 2 \cdot 10^{-6}m$. A sample output of the $r_{CM,z}$ estimation during a fine balancing iteration for a 3U and 1U are shown in Figures 4.10b and 4.11b respectively, while the outcome of the identification across the three iterations is summarized in Table 4.2.

4.5.2 Experimental residual disturbance estimation

The effectiveness of the balancing is checked first by comparing the kinetic energy variation during free platform oscillations before and after balancing. As shown in Fig.

4.13, three balancing iterations reduces the kinetic energy variation by about 98% for the 3U platform. Nevertheless, a more convenient indicator is the magnitude of the residual disturbance torque acting on the system after balancing, which can be estimated with the method described in Section 4.4. The outcome of the estimate is shown in Fig. 4.14a for the 3U platform and Fig. 4.14b for the 1U platform. The upper bound of the torque magnitude was found to be about $5 \cdot 10^{-5} Nm$, while its root mean squared value is $2.5 \cdot 10^{-5} Nm$. These values, despite being one order of magnitude higher than the theoretical lower bound of the unbalance torque alone, set by the mass displacement resolution, compares favorably with respect to the outcome from similar studies, see Table 1.1

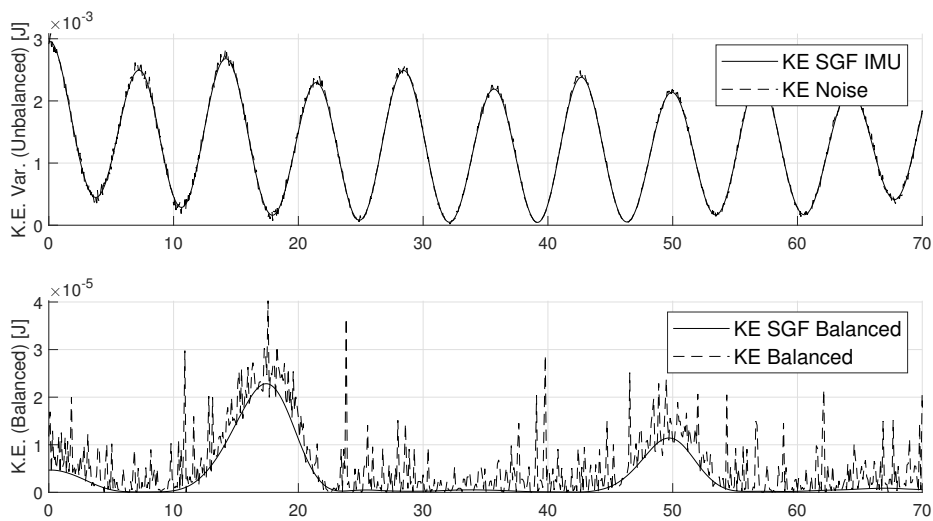
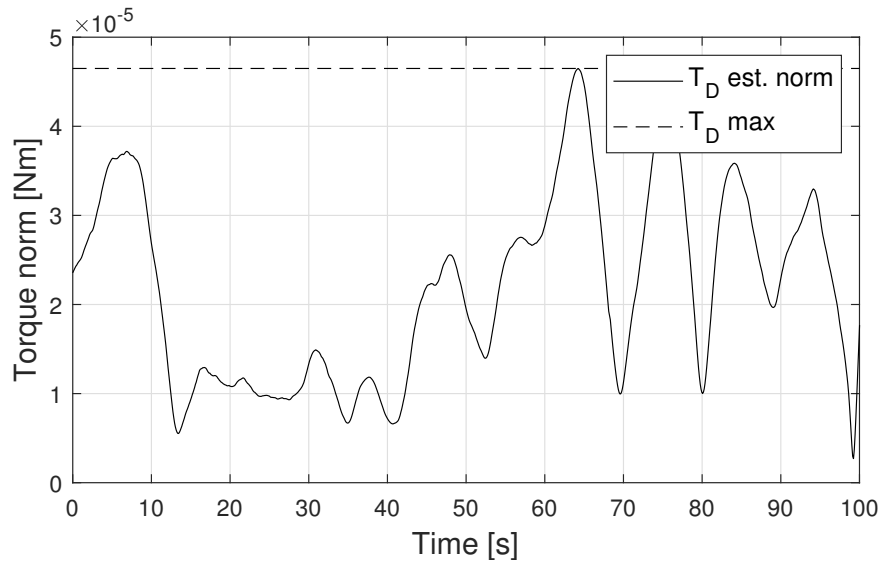
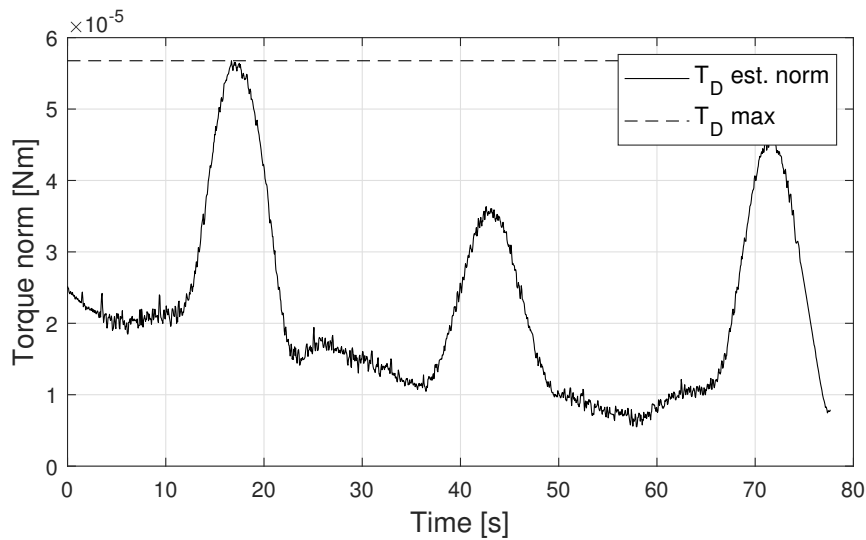


Figure 4.13: Kinetic energy variation of the balanced platform [Bahu and Modenini \(2020\)](#);

4.6. Magnetic detumbling



(a) External torque acting on the balanced 3U platform [Bahu and Modenini \(2020\)](#);



(b) External torque acting on the balanced 1U platform;

Figure 4.14: Balancing effectiveness evaluation.

4.6 Magnetic detumbling

The balancing procedure effectiveness was verified in a HWIL simulation. The COTS CubeSat mockup integrated on the 1U platform was used for a magnetic attitude control experiment. The test case foresees angular speed damping, corresponding to the on-orbit detumbling.

Soon after being separated from the launcher, the spacecraft needs to damp the rotational kinetic energy imparted by the separation system. This operation can be done by magnetic actuation alone through the so called B-dot control law:

$$\mathbf{m}_c = -k \, d\mathbf{b}/dt \quad (4.23)$$

where \mathbf{m}_c is the control dipole and \mathbf{b} is the magnetic field vector measurement. This control law is very simple, needs only magnetic field vector and is robust to measurements biases.

Complete damping by means of magnetic actuation alone is not possible for a static magnetic field, as no torque can be exerted along the \mathbf{b} direction. Hence, time-varying magnetic field experienced by the spacecraft on the orbit was simulated by means of the Helmholtz cage. The magnetic field model for a 500 km polar orbit is computed following the IGRF model. Damping time constant is in the order of hours for this type of orbit. However, in laboratory environment, air-bearing friction torque would dump the angular speed in much smaller time. To provide faster dumping by magnetic actuation, magnetic field time variance was speed up by factor of 50. Angular speed components through the experiment are shown in Fig. 4.15a. The initial angular speed is $\omega(0) = [-0.03, -0.04, 0.7]rad/s^2$, and magnetorquers are activated at $t=10$ s.

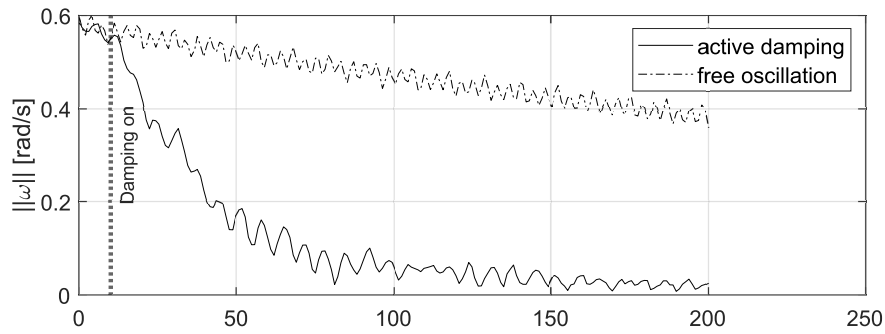
The platform is subjected to the action of other torques. Oscillation on the x- and y-axes are due to the residual disturbance torque. In Fig 4.15b, the action of the air bearing friction and aerodynamic torque can be appreciated by observing the dash-dotted line. For a freely oscillating platform angular speed still slowly decay. However, the action of the damping algorithm is clear, as biggest part of the angular speed is damped in a short time.

4.7 Discussion

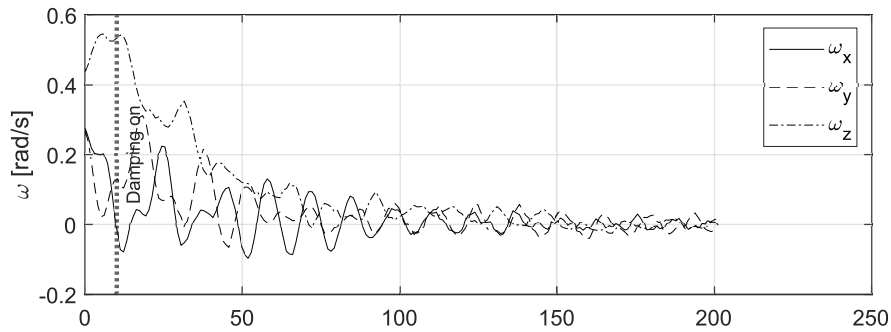
In this chapter, a two-step, iterative procedure for reducing the gravitational torque acting on an attitude dynamic testbed based on air bearing is presented and experimentally tested. Two iterations, at least, are envisaged: a first one, for large unbalance vector compensation and inertia parameters estimation, followed by a fine balancing iteration. Each iteration consists of two stages: a real-time in-plane balancing, followed by an estimation of dynamic parameters.

For the in-plane balancing, real-time feedback control is employed. A novel nonlinear

4.7. Discussion



(a) Angular speed vector;



(b) Angular speed norm in case of free oscillation and damping;

Figure 4.15: Experimental detumbling.

feedback for single axis pointing, robust to unmodeled disturbances, is developed and compared to a linearized PID controller.

Once the plane balancing is performed, two components of the unbalance vector are compensated. After the first plane balancing iteration, the residual center of gravity offset, together with an estimate of the inertia matrix elements, are obtained through a batch LSQ estimator. Pre-processing of the angular rate measurements using a Savitzki-Golay filter was found to be of paramount importance for achieving good estimates. For the following balancing iterations, inertia parameters are used as constraints for accurate residual vertical offset estimation.

For the experimental validation of the balancing procedure, kinetic energy and angular momentum variations were analyzed. A residual disturbance torque smaller than $5 \cdot 10^{-5} Nm$ was retrieved from experimental verification. The experimental results show the facility capabilities in highly demanding magnetic attitude control scenario.

Part III

Nanosatellites attitude control

5

Attitude stabilization of a magnetically actuated spacecraft

In this chapter, a novel approach to the three-axis attitude stabilization of a magnetically actuated spacecrafts is described¹. The proposed control laws is designed within a hybrid framework. Due to the actuators type, the system model described in Section 2.4 is instantaneously underactuated and time-varying, so that low pointing errors and robustness are difficult to achieve at the same time. To provide both properties, two control laws and a supervisor for switching between them are employed. As discussed in Section 2.7.1, the magnetic field affecting the spacecraft can be assumed to be time periodic, allowing a time-independent model to be developed in a hybrid framework in Section 5.1.

For the design of the local control law, the H-inf regulator with guaranteed performance proposed in [Zanchettin et al. \(2013\)](#) is used, as described in Section 5.3. For the global controller in Section 5.4, previous results based on averaged theory proposed in [Lovera and Astolfi \(2004\)](#) are extended to provide ISS properties in Section 5.4.4. The resulting nonlinear controller provides global stability and robustness with respect bounded disturbances.

¹The content of this chapter is largely based on: [Bahu and Modenini \(2021\)](#)

The stabilization is accomplished by uniting two controllers through a hybrid supervisor which governs the switching between the two, see Section 5.5. Analytical results are verified by means of realistic numerical simulations in Section 5.6. The control algorithm advantages and disadvantages are discussed in Section 5.7.

5.1 Magnetically actuated spacecraft model in a hybrid framework

The nonlinear system under analysis is continuous and time-dependent. For an inertially pointing spacecraft travelling on a circular orbit, the experienced geomagnetic field can be approximated as a periodic signal with period equal to half the orbital one, $T_{orb}/2$. This is strictly true only for a magnetic dipole, but can be applied to the geomagnetic field as well after fitting of the IGRF model data (see Section 2.7). Thanks to this assumption, the input matrix can be described as state-dependent with respect to an auxiliary variable ν , and the plant becomes time-independent in the hybrid framework. Then, jumps occur whenever ν equals $T_{orb}/2$. The hybrid plant state is $\mathbf{x}_p = [\mathbf{q}^T, \boldsymbol{\omega}^T, \nu]^T$ whose dynamics reads:

$$\mathcal{H} : \begin{cases} \dot{\mathbf{x}}_p = f_p(\mathbf{x}_p, \mathbf{u}) = \begin{bmatrix} f_c(\mathbf{x}_p) + v(\mathbf{x}_p)\mathbf{u} \\ 1 \end{bmatrix} & (\mathbf{q}, \boldsymbol{\omega}, \nu, \mathbf{u}) \in C_p =: \mathbb{R}^{n_p} \times [0, T_{orb}/2] \times \mathbb{R}^m \\ \mathbf{x}_p^+ = g_p(\mathbf{x}_p) & (\mathbf{q}, \boldsymbol{\omega}, \nu, \mathbf{u}) \in D_p =: \mathbb{R}^{n_p} \times [T_{orb}/2] \times \mathbb{R}^m \end{cases} \quad (5.1)$$

where \mathcal{H}_p is the hybrid plant, C_p and D_p are the flow and jump set of the plant, $\mathbf{q}, \boldsymbol{\omega}, \mathbf{u}$ are defined as before and $n_p = 7, m = 3$. From Section 2.4, the continuous part of the system is defined by:

$$f_c(\mathbf{x}_p) = \begin{bmatrix} -\frac{1}{2}(\boldsymbol{\omega} \times \mathbf{q}_e) + \frac{1}{2}q_4\boldsymbol{\omega} \\ -\frac{1}{2}\boldsymbol{\omega}^T \mathbf{q}_e \\ -J^{-1}\boldsymbol{\omega} \times J\boldsymbol{\omega} \end{bmatrix} \quad v(\mathbf{x}_p) = \begin{bmatrix} \mathbf{0}_{3 \times 3} \\ B_h(\nu) \end{bmatrix}. \quad (5.2)$$

where $B_h(\nu)$ is a singular matrix defined as:

$$B_h(\nu) = J^{-1}\Gamma(\nu) = J^{-1} \left(\frac{[\mathbf{b}(\nu)]^\times [\mathbf{b}(\nu)]^{\times,T}}{\|\mathbf{b}(\nu)\|^2} \right), \quad (5.3)$$

with $\Gamma(\nu)$ being a projection matrix and $[\mathbf{b}(\nu)]^{\times,T}$ is the transpose of the skew-symmetric matrix $[\mathbf{b}(\nu)]^\times$.

The jump map is designed as:

$$g_p(\mathbf{x}_p) = \begin{bmatrix} \mathbf{q} \\ \boldsymbol{\omega} \\ 0 \end{bmatrix}. \quad (5.4)$$

5.2 Attitude stabilization control problem

The goal in attitude stabilization is to drive $[\mathbf{q}^T, \boldsymbol{\omega}^T]^T$ to $[[0 \ 0 \ 0 \ 1]^T, [0 \ 0 \ 0]^T]^T$. The control problem in hybrid framework is summarized in the following proposition:

Proposition 1. Given a target set $\mathcal{A}_p = [[0 \ 0 \ 0 \ 1]^T, [0 \ 0 \ 0]^T, [0, T]]^T$, design a hybrid supervisor \mathcal{H}_K such that:

1. the set \mathcal{A}_p is Globally Asymptotically Stable in case of no external disturbances;
2. maximal solutions of closed the loop system are complete and converge to a neighborhood of \mathcal{A}_h in the presence of small measurement noise, unmodelled dynamics and external disturbances with guaranteed level of performance.

A supervisor \mathcal{H}_K designed as above, makes \mathcal{A}_p globally robustly stable.

In the proposed approach, the task is accomplished by uniting two controllers $\kappa_0 : \mathbb{R}^{n_c} \rightarrow \mathbb{R}^m$ and $\kappa_1 : \mathbb{R}^{n_c} \rightarrow \mathbb{R}^m$, where n_c is the controller state dimension. The two controllers are chosen such that:

- κ_0 guarantees local asymptotic stability of the origin of \mathcal{H}_p and local optimality.
- κ_1 guarantees global asymptotic stability of the origin of \mathcal{H}_p and robustness.

Then, Proposition 1 can be solved by supervising control technique described in Section 5.5, through a hybrid supervisor which governs the switching between the two. The supervisors relies on a hysteresis region to avoid undesirable switching and chattering.

5.3 Local linear control law

For linearized dynamics described in Section 2.4.1, we adopt a local robust controller with guaranteed H_∞ performance that have been proposed in [Zanchettin et al. \(2013\)](#), which is briefly recalled hereafter. It consists of a projection-based feedback $\mathbf{u} = K\mathbf{x}_r$, where the constant-gain matrix K is designed so as to provide a guaranteed level of disturbance attenuation. To this end, a performance index is defined as the H_∞ norm of the input/output transfer function \mathcal{F}_{yw} . In time domain and for the considered class of systems, the H_∞ norm is equivalent to the \mathcal{L}_2 gain of \mathcal{F}_{yw} :

$$\|\mathcal{F}_{yw}\|_\infty = \sup_{\mathbf{w} \in L_2} \frac{\|\mathbf{y}\|_2}{\|\mathbf{w}\|_2} \quad (5.5)$$

where \mathbf{w} is the input of interest, assumed be equal to total disturbance τ_d in the considered case, and \mathbf{y} is the performance output measure:

$$\mathbf{y} = \begin{bmatrix} \mathbb{I}_{3 \times 3} \\ \mathbf{0}_{3 \times 3} \\ \sigma K \end{bmatrix} \mathbf{x}_r = C\mathbf{x}_r \quad (5.6)$$

where σ being a design parameter introduced to limit the control effort and \mathbf{x}_r is the state of linearized dynamics, defined in Section 2.4.1.

The operator \mathcal{F}_{yw} represents the closed-loop transfer function:

$$\mathcal{F}_{yw} = \begin{bmatrix} A + BK & \mathbb{I}_{3 \times 3} \\ C & \mathbf{0}_{3 \times 3} \end{bmatrix}. \quad (5.7)$$

Provided the LTP system is stable, a frequency domain representation of \mathcal{F}_{yw} can be obtained by expanding the dynamic matrices in complex Fourier series and computing their Toeplitz transformations, see [Zhou et al. \(1999\)](#). A frequency domain operator \mathcal{F}_{yw}^σ can then be defined, similarly to the frequency analysis of LTI systems.

First, define the Exponentially Modulate Periodic (EMP) signal $e_{mp}(t)$ of period $T = 2\pi/\Omega_T$ and modulation s :

$$e_{mp}(t) = \sum_{k \in \mathbb{Z}} e_{mp,k} e^{s_k t}, \quad s_k = s + jk\Omega_T, \quad (5.8)$$

equivalently represented by $E_{mp} = [\dots e_{mp,-2} e_{mp,-1} e_{mp,0} e_{mp,1} e_{mp,2} \dots]^T$, where $e_{mp,k}$ is the k -th harmonic coefficient. The EMP signals are a general form of periodic ones, which are the a special case with $s = 0$.

For a stable LTI system (A, B, C, D) , complex Fourier series expansions is defined by means of EMP representation. For a dynamical matrix A (and similarly for B, C, D):

$$A(t) = \sum_{m \in \mathbb{Z}} A_m e^{jm\Omega_T t} \quad (5.9)$$

where A_m are the Fourier coefficients and $\Omega_T = \frac{2\pi}{T}$. Define a Toeplitz transformation of $A(t)$:

$$\mathcal{A} = \mathcal{T}\{(A(t))\} = \begin{bmatrix} \ddots & \vdots & \vdots & \vdots & \\ \cdots & A_0 & A_2 & A_2 & \cdots \\ \cdots & A_1 & A_0 & A_1 & \cdots \\ \cdots & A_2 & A_1 & A_0 & \cdots \\ & \vdots & \vdots & \vdots & \ddots \end{bmatrix}. \quad (5.10)$$

Define Toeplitz transformations of B, C, D as \mathcal{B}, \mathcal{C} and \mathcal{D} and the input/output Harmonic Transfer Function (HTF):

$$\mathcal{F}_{yw}(s) = \mathcal{C}(s\mathcal{I} - (\mathcal{A} - \mathcal{N}))^{-1} \mathcal{B} + \mathcal{D} \quad (5.11)$$

where $\mathcal{N} = \text{blkdiag}\{in\Omega_T \mathbb{I}\}$, $n \in \mathbb{Z}$, i is the imaginary unit and $\Omega_T = \frac{4\pi}{T}$. For practical purpose, truncation of double-infinite, time-invariant operator \mathcal{F}_{yw} can be considered for approximated input/output H_∞ norm transfer function. Eq. 5.5 is valid also for a LTP system (Zhou et al., 1999), and it's possible to find an approximated value by analyzing asymptotically equivalent LTI representation. See Zhou and Hagiwara (2005) for more details.

To minimize $\|\mathcal{F}_{yw}(s)\|_\infty$, the gain matrix K needs to be tuned, under stability constraints on the characteristics multipliers of the monodromy matrix. These can be computed as described in Section 2.5. The control problem is formalized as:

$$\min_K \|\mathcal{F}_{yw}(s)\|_\infty \quad \text{subject to} \quad \rho(\psi_{A+B(t)K}) < 1. \quad (5.12)$$

Since the resulting cost function is non-smooth, a randomized iterative optimization algorithm is employed to solve the minimization problem, as described in [Zanchettin et al. \(2013\)](#).

5.4 Global nonlinear control law

The global stability for a magnetically actuated spacecraft can be achieved, in a disturbance-free case, through a projected, PD-like, nonlinear control law. This result was proved in [Lovera and Astolfi \(2004\)](#) by means of the averaging technique. We will extend the result and show the input-to-state stability for the averaged nonlinear dynamics described in Section 2.4 with respect to bounded disturbances, starting from the ISS properties of a fully actuated system as provided in [Hu and Zhang \(2018\)](#).

Once ISS of the nonlinear averaged system subject to a PD-like feedback is provided, semi-global practical asymptotic stability of the actual system will be shown recalling the results in [Nešić and Teel \(2001\)](#).

5.4.1 Averaging of the nonlinear systems

Averaging theory applies to systems with system dynamics which can be divided in different time scales, i.e when time-variance period is small with respect to the dynamics. If the system can be expressed as functions of a small parameter $\varepsilon > 0$:

$$\dot{\mathbf{x}} = f(t, \mathbf{x}, \varepsilon), \quad (5.13)$$

and continuity of solutions with respect the initial conditions holds, the following theorem applies ([Khalil, 1996](#)).

Theorem 5.4.1. Let $f(t, \mathbf{x}, \varepsilon)$ and its partial derivatives with respect to $(\mathbf{x}, \varepsilon)$ up to the second order be continuous and bounded for $f(t, \mathbf{x}, \varepsilon) \in [0, \infty) \times D_0 \times [0, \varepsilon_0]$, for every compact set $D_0 \in D$, where $\varepsilon > 0$ and $D \in \mathbb{R}^n$ is a domain. If there exists a limit:

$$f_{av}(\mathbf{x}) = \lim_{T \rightarrow \infty} \frac{1}{T} \int_t^{t+T} f(s, \mathbf{x}, \varepsilon)|_{\varepsilon=0} ds, \quad (5.14)$$

and a function $\beta_{av} \in \mathcal{KL}$, $\forall T > T^* > 0$, for some T^* :

$$\left| \frac{1}{T} \int_t^{t+T} f(t, \mathbf{x}, 0) - f_{av}(\mathbf{x}) \right| < \beta_{av}(\max(|\mathbf{x}|, 1), T), \quad (5.15)$$

then $f_{av}(\mathbf{x})$ is called a time invariant average of $f(t, \mathbf{x}, \varepsilon)$.

If the origin $\mathbf{x} = 0 \in D$ is an exponentially stable equilibrium point of the averaged system and the initial condition of the system lies in the compact subset of the region of attraction, then there exists ε^* such that for all $0 < \varepsilon < \varepsilon^*$, $\mathbf{x}(t, \varepsilon)$ is defined and for a function $\alpha \in \mathcal{K}$:

$$\mathbf{x}(t, \varepsilon) - \mathbf{x}_{av}(\varepsilon t) = O(\alpha(\varepsilon)) \quad \forall t \in [0, \infty). \quad (5.16)$$

Moreover, if $f(t, 0, \varepsilon) = 0$ for all $(t, \varepsilon) \in [0, \infty) \times [0, \varepsilon_0]$, the origin is an exponentially stable equilibrium point of the actual system.

The closeness of trajectories of the averaged and actual systems follows after rearranging the former so as to differ from the latter by a small perturbation (in parameter ε), see [Khalil \(1996\)](#). The general result is that GAS of the averaged system implies uniform semi-global practical stability of the actual system:

Definition 5.4.1. The system $\dot{\mathbf{x}} = f(t, \mathbf{x}, \varepsilon)$ is semi-globally asymptotically practically stable in ε if there exists $\beta \in \mathcal{KL}$ and for each pair of strictly positive real ρ, Ω_x there exists ε^* s.t for all $\varepsilon \in (0, \varepsilon^*)$ the solution satisfy $|\mathbf{x}(t)| \leq \beta(\mathbf{x}(0), t - t_0) + \rho$ whenever $\mathbf{x}(0) < \Omega_x$.

However, in case of an exogenous signal, such as input disturbance, no results on the performance are provided by the above theorem. To provide performance index in case of disturbances, Input-to-State notion for \mathcal{L}_∞ stability analysis presented in Section 2.5 has been extended in the context of averaging ([Nešić and Teel, 2001](#)).

Let us extend the average definition presented in Theorem 5.4.1, rearranged with respect to a time variable $s = \varepsilon t$:

Definition 5.4.2. A locally Lipschitz function $f_{sa} : R^n \times R^m \rightarrow R^n$ is said to be a strong average of $f(s, \mathbf{x}, \mathbf{w})$ if there exists a class \mathcal{KL} function β_{av} and a $T^* > 0$ such that $\forall t \geq 0, \forall \mathbf{w} \in L_\infty, \forall T \geq T^*$, the following holds:

$$\left| \frac{1}{T} \int_t^{t+T} [f_{sa}(\mathbf{x}, \mathbf{w}(s)) - f(s, \mathbf{x}, \mathbf{w}(s))] ds \right| \leq \beta_{av}(\max\{|\mathbf{x}|, \mathbf{w}, 1\}, T), \quad (5.17)$$

and is defined as $\dot{\mathbf{x}} = f_{sa}(\mathbf{x}, \mathbf{w}(s))$.

Assume system Eq. 5.13 can be rearranged in presence of input \mathbf{w} with respect to a

5.4. Global nonlinear control law

time variable s as follows:

$$\frac{\delta \mathbf{x}}{\delta s} = F(s, \mathbf{x}) + g(\mathbf{x}, \mathbf{w}). \quad (5.18)$$

It was shown by [Teel et al. \(1998\)](#) that, if there exists an average of $F(s, \mathbf{x})$, denoted by $F_{av}(\mathbf{x})$, then $f_{sa}(\mathbf{x}, \mathbf{w}) = F_{av}(\mathbf{x}) + g(\mathbf{x}, \mathbf{w})$ satisfies the above definition of the strong average. In this case computing the strong average is as difficult as computing the average for a system without disturbances.

The concept of Lyapunov-ISS gain can now be introduced.

Definition 5.4.3. Let $\tilde{\gamma} \in \mathcal{G}$. A time-invariant system $\dot{\mathbf{x}} = f(\mathbf{x}, \mathbf{w})$ is said to be *Lyapunov-ISS* with gain $\tilde{\gamma}$ if there exists a function $V : \mathbb{R}^n \rightarrow \mathbb{R}_{\geq 0}$, $\alpha_1, \alpha_2, \alpha_3 \in \mathcal{K}_{\infty}$, $\gamma \in \mathcal{G}$ s.t. $\alpha_1^{-1} \circ \alpha_2 \circ \gamma(s) \leq \tilde{\gamma}(s)$ for all $s \geq 0$ and, for all (x, w) :

$$\begin{aligned} \alpha_1(|\mathbf{x}|) &\leq V(\mathbf{x}) \leq \alpha_2(|\mathbf{x}|) \\ |\mathbf{x}| \geq \gamma(|\mathbf{w}|) &\Rightarrow \frac{\delta V}{\delta \mathbf{x}} f(\mathbf{x}, \mathbf{w}) \leq -\alpha_3(|\mathbf{x}|). \end{aligned} \quad (5.19)$$

As a time invariant system is Lyapunov-ISS if and only if it is ISS, the following theorem implies ISS with gain $\tilde{\gamma}$ for the actual system:

Theorem 5.4.2. If the strong average of Eq. 5.18 exists and is Lyapunov-ISS with gain $\tilde{\gamma}$, then there exists a \mathcal{KL} class function β_{sa} and there exist any strictly positive real numbers $\Omega_x, \Omega_d, \iota$, there exists $\varepsilon^* > 0$ such that for all $\varepsilon \in (0, \varepsilon^*)$ the solutions of the system satisfy:

$$|\mathbf{x}(t)| = \max\{\beta_{sa}(\mathbf{x}(t_0), t), \tilde{\gamma}(\|\mathbf{w}\|_{\infty})\} + \iota, \forall t \geq t_0 = 0. \quad (5.20)$$

Whenever $|\mathbf{x}(t)| \leq \Omega_x, \|\mathbf{w}\|_{\infty} \leq \Omega_d$, the system is semi-globally practically (in the parameter ε) ISS with gain $\tilde{\gamma}$.

The above theorem states that ISS of a strong average implies semi-global practical ISS of the actual system.

5.4.2 Nonlinear averaged controller

Spacecraft dynamics can be casted in form of Eq 5.13 by a coordinate change $\boldsymbol{\xi} = [\boldsymbol{\xi}_1^T, \boldsymbol{\xi}_2^T]^T = [\mathbf{q}^T, \boldsymbol{\omega}^T/\varepsilon]^T$:

$$\dot{\boldsymbol{\zeta}}_1 = \varepsilon W(\boldsymbol{\xi}_1) \boldsymbol{\xi}_{2r} \quad (5.21)$$

$$\mathbf{J} \dot{\boldsymbol{\xi}}_2 = \varepsilon (-\boldsymbol{\xi}_2 \times \mathbf{J} \boldsymbol{\xi}_2) + 3 \varepsilon \omega_o^2 (\hat{\mathbf{e}}_{z,b} \times \mathbf{J} \hat{\mathbf{e}}_{z,b}) - \varepsilon \Gamma(t) \Gamma_{av}^{-1} \mathbf{u}$$

where

$$\dot{\hat{\Gamma}}_{av} = \frac{1}{t} \Gamma - \frac{1}{t} \hat{\Gamma}_{av} \text{ and } \hat{\Gamma}_{av}(0) = \Gamma(0), \hat{\Gamma}_{av} = \frac{1}{t} \int_0^T \Gamma(t) dt. \quad (5.22)$$

It was shown in [Lovera and Astolfi \(2004\)](#) that the controllability of the original system is provided if the following condition is satisfied:

$$\bar{\Gamma} = \lim_{T \rightarrow \infty} \frac{1}{T} \int_0^T S(\tilde{\mathbf{b}}(t)) S^T(\tilde{\mathbf{b}}(t)) dt > 0 \quad (5.23)$$

where $\tilde{\mathbf{b}}(t) = \frac{A(\mathbf{q})^T \mathbf{b}(t)}{\|\mathbf{b}(t)\|}$, and that the closed loop system can be rendered GAS for some ε^* , $0 < \varepsilon < \varepsilon^*$, by the following feedback control law:

$$\mathbf{u} = -J^{-1}(\varepsilon k_v \boldsymbol{\omega} + \varepsilon^2 k_p \mathbf{q}), \quad (5.24)$$

with k_v and k_p positive constants.

For the proof, authors' of [Lovera and Astolfi \(2004\)](#) considered the following Lyapunov function:

$$V_1 = \frac{1}{2} k_p \left(\boldsymbol{\xi}_1^T \boldsymbol{\xi}_1 + (\xi_{14} - 1)^2 \right) + (J_0 \boldsymbol{\xi}_2)^T A(\boldsymbol{\xi}_1)^T \bar{\Gamma}^{-1} A(\boldsymbol{\xi}_1) (J_0 \boldsymbol{\xi}_2) \quad (5.25)$$

where $J_0 = A(\mathbf{q})^T J A(\mathbf{q})$, whose derivative was shown to become negative semidefinite using the feedback Eq. 5.24 and in the absence of disturbances.

However, the continuous feedback Eq. 5.24 has two drawbacks, namely a) it is not robust with respect to arbitrarily small measurement noise due to the unwinding phenomenon, and b) in case of a disturbance torque $\boldsymbol{\tau}_d$ different from zero, the asymptotic stability is no longer guaranteed. These two drawbacks will be addressed in Section 5.4.3 and 5.4.4 respectively.

5.4.3 Hybrid nonlinear averaged controller

Due to topological obstruction of the attitude representation space $SO(3)$, there is no continuous feedback providing GAS, as robustness with respect arbitrarily small external disturbances and measurement noise cannot be provided. In practice, semi-global

5.4. Global nonlinear control law

asymptotic stability is provided. The issue have been solved in [Mayhew et al. \(2011\)](#), through adding an auxiliary parameter h , and defining the following hybrid feedback:

$$\begin{aligned} \mathbf{u} &= -J^{-1}(\varepsilon k_v \boldsymbol{\omega} + \varepsilon^2 k_p h \mathbf{q}_e) \quad \text{if } (\mathbf{q}, \boldsymbol{\omega}, h) \in C \\ h^+ &= g_h(h) = -h \quad \text{if } (\mathbf{q}, \boldsymbol{\omega}, h) \in D \end{aligned} \quad (5.26)$$

with the flow and jump sets defined as $C = \{(\mathbf{q}, \boldsymbol{\omega}, h) \in \mathcal{S}^3 \times \mathbb{R}^3 \times H : h q_4 > -\delta\}$ and $D = \{(\mathbf{q}, \boldsymbol{\omega}, h) \in \mathcal{S}^3 \times \mathbb{R}^3 \times H : h q_4 \leq -\delta\}$, for all $0 < \delta < 0.4, h \in H = [-1, 1]$. The h parameter provides a hysteresis region, so as to avoid so called unwinding phenomena. Logical hysteresis is shown in Fig. 5.1. For a rising signal, the output value change at input value of 0.4. For a falling signal, the output value change at input value 1.

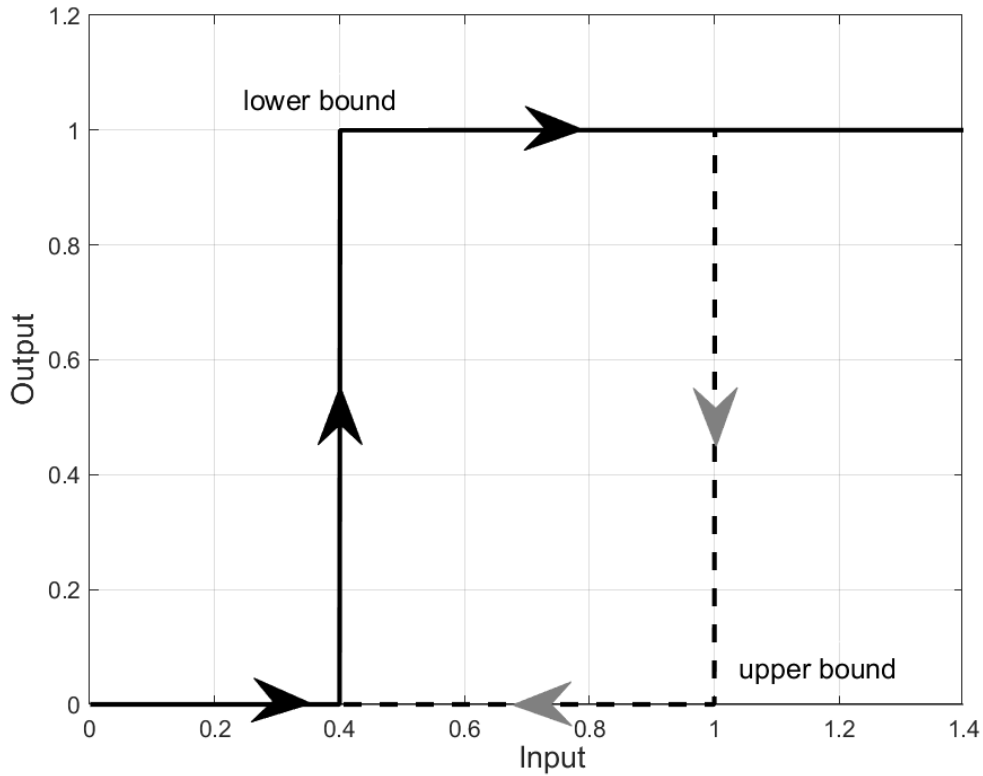


Figure 5.1: Logical hysteresis switching

5.4.4 ISS of the averaged non-linear dynamics

Since the averaged system is fully actuated, robustness by ISS property can be shown as in [Hu and Zhang \(2018\)](#). By Theorem 5.4.2, ISS of the average provides practical stability of the nominal system, hence a performance index for the actual system.

Theorem 5.4.3. Consider the averaged, fully actuated system. Suppose the disturbance is bounded with $\|\tau_d\|_\infty \geq \tau_{d,max}$, then the system is forward-complete and there exist functions $\beta_h \in \mathcal{KL}$, $\gamma_h \in \mathcal{G}$ such that the system is Input-To-State stable with respect τ_d with gain function:

$$\gamma_h = \sqrt{\frac{\lambda_{max}(P_2)}{\lambda_{min}(P_1)}} \left(\frac{\sqrt{3(1+c_l^2)}}{\lambda_{min}(Q)} + c_\gamma \right) \quad (5.27)$$

where λ_{max} and λ_{min} denote, respectively, the maximum and minimum eigenvalues of the matrix argument, c_γ is an arbitrarily small constant and c_l must be small enough to guarantee that the Lyapunov function:

$$V_2 = (\varepsilon^2 k_p + c_l \varepsilon k_v) \left[(1 - h q_4)^2 + \mathbf{q}_e^T \mathbf{q}_e \right] + c_l h \mathbf{q}_e^T J \boldsymbol{\omega} + \frac{1}{2} \boldsymbol{\omega}^T J \boldsymbol{\omega} \quad (5.28)$$

is positive definite. P_1 and P_2 are matrix bounds on V_2 :

$$\begin{aligned} \mathbf{x}_r^T \begin{bmatrix} (\varepsilon^2 k_p + c_l \varepsilon k_v) \mathbb{I}_{3 \times 3} & -0.5 \varepsilon c_l \lambda_{max}(J) \mathbb{I}_{3 \times 3} \\ -0.5 \varepsilon c_l \lambda_{max}(J) \mathbb{I}_{3 \times 3} & 0.5 \varepsilon^2 \lambda_{min}(J) \mathbb{I}_{3 \times 3} \end{bmatrix} \mathbf{x}_r &= \\ = \mathbf{x}_r^T P_1 \mathbf{x}_r \leq V \leq \mathbf{x}_r^T P_2 \mathbf{x}_r &= \\ \mathbf{x}_r^T \begin{bmatrix} 4(\varepsilon^2 k_p + c_l \varepsilon k_v) \mathbb{I}_{3 \times 3} & 0.5 \varepsilon c_l \lambda_{max}(J) \mathbb{I}_{3 \times 3} \\ 0.5 \varepsilon c_l \lambda_{max}(J) \mathbb{I}_{3 \times 3} & 0.5 \varepsilon^2 \lambda_{max}(J) \mathbb{I}_{3 \times 3} \end{bmatrix} \mathbf{x}_r & \end{aligned} \quad (5.29)$$

and Q is defined as:

$$Q = \begin{bmatrix} c_l \varepsilon^2 k_p & 0 \\ 0 & \varepsilon k_v - \frac{3}{2} c_l \lambda_{max}(J) \end{bmatrix}. \quad (5.30)$$

Remark 5.4.1. The constants c_γ , c_l are necessary for the analysis and do not affect the controller definition

Remark 5.4.2. the arbitrarily small constant c_γ guarantees the region defined by gain γ_h can be reached in finite time.

Proof 5.4.3.1. Only a sketch will be outlined here, see [Hu and Zhang \(2018\)](#) for details. First, global boundness of ω is proved, by showing that the Lyapunov function derivative reads $\dot{V}_2 = -\omega^T J \omega$ when the system is given the feedback Eq. 5.24. Next, \mathbf{x}_r is shown to enter in finite time a small region Ω_{x_r} , which depends on $\tau_{d,max}$. The Lyapunov function is shown to decrease in the jump set D , and is shown that its derivative is negative definite on the flow set C for all \mathbf{x}_r outside Ω_{x_r} and for all Q defined as in Theorem 5.4.3. Since V_2 is monotonically decreasing both in the flow and jump sets as long as $\mathbf{x}_r \notin \Omega_{x_r}$, Ω_{x_r} is reached in a finite time and with a finite number of jumps.

Theorem 5.4.3 provides a bound on the state norm of the averaged system valid after some time t^* , through computation of the gain function γ_h . This bound is a function of the disturbance L-infinity norm, the principal moments of inertia of the spacecraft, and the controller parameters k_p, k_v, ε . For the actual system, semi-globally practical asymptotic stability is guaranteed if the strong average of the system exists, as shown in Section 5.4.1.

5.5 Hybrid supervisor design

To solve the unifying problem, a supervisor must be designed. The supervisor selects the most appropriate controller depending on the value of the plant state so as the feedback \mathbf{u} renders the target set robustly GAS. The choice of the controller is governed by a discrete, auxiliary variable $z \in \{0, 1\} \equiv Z$. A block diagram of the resulting closed loop system is depicted in Figure 5.2.

The resulting controller is hybrid, since it has continuous and discrete dynamics, and is defined as:

$$\mathcal{H} : \begin{cases} \dot{z} = 0 & (z, \mathbf{x}_p) \in C_s := \bigcup_{z \in Z} (C_{S_z} \times \{z\}) \\ z^+ = g_s(z, \mathbf{x}_p) & (z, \mathbf{x}_p) \in D_s := \bigcup_{z \in Z} (D_{S_z} \times \{z\}) \end{cases} \quad (5.31)$$

where $g_s(z, \mathbf{x}_p)$ is the supervisor jump map. The definition of the flow and jump sets for each controller C_{S_z}, D_{S_z} and of the jump map g_s shall guarantee that $(g_s(z, \mathbf{x}_p) \times \mathbf{x}_p) \subset C_s \cup D_s$ for each $(z, \mathbf{x}_p) \in D_s$. D_{s_1} and C_{s_0} have to be defined so as to guarantee that the

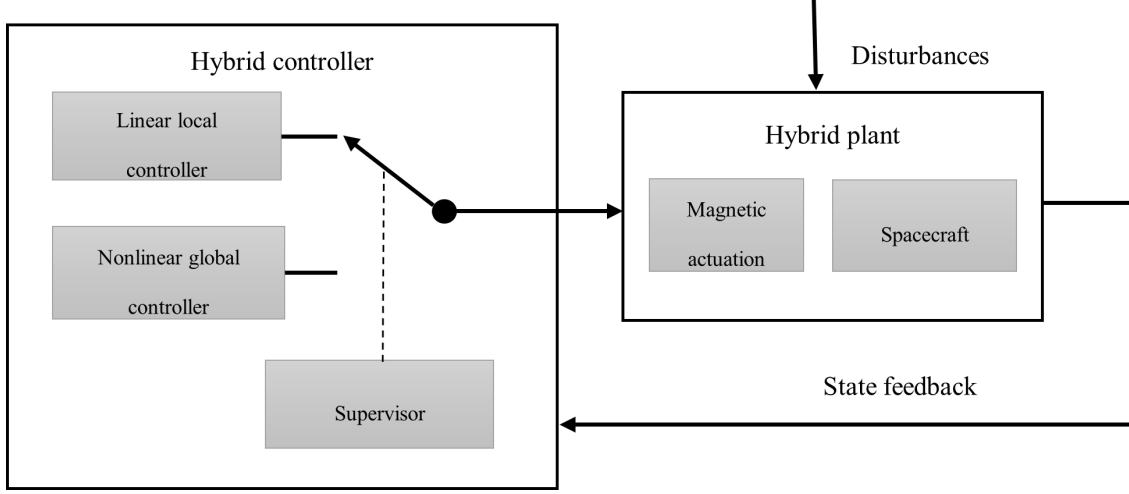


Figure 5.2: Supervisory control closed loop system.

solutions starting inside D_{s_1} with $z = 0$ remain in a closed set that is a strict subset of C_{s_0} . To guarantee asymptotic stability, C_{s_0} must be a sufficiently small neighbourhood of the origin and D_{s_1} have to be small neighbourhood of the origin strictly contained in C_{s_0} . Then, the first part of Proposition 1, i.e. GAS of the origin, is satisfied if the following assumption on the existence of Lyapunov functions holds.

Assumption 5.5.1. For the control laws κ_0, κ_1 , there exist two continuous differentiable functions $W_z : \mathbb{R}^n \rightarrow \mathbb{R}_{\geq 0}$ and $\alpha_1, \alpha_2 \in \mathcal{K}_\infty$ such that, for $z = 0, 1$ $\alpha_1(|\mathbf{x}_p|_{\mathcal{A}}) \leq W_z(\mathbf{x}_p) \leq \alpha_2(|\mathbf{x}_p|_{\mathcal{A}}) \forall \mathbf{x}_p \in \mathbb{R}^n$ satisfying the following properties:

- There exists an open neighbourhood \mathcal{U}_0 of the origin and a function $\rho_0 \in \mathcal{PD}$ such that $\langle \nabla W_0(\mathbf{x}_p), f(\mathbf{x}_p, \kappa_0(\mathbf{x}_p)) \rangle \leq -\rho_0(|\mathbf{x}_p|_{\mathcal{A}}) \forall \mathbf{x}_p \in \mathcal{U}_0$.
- There exists a function $\rho_1 \in \mathcal{PD}$ such that $\langle \nabla W_1(\mathbf{x}_p), f(\mathbf{x}_p, \kappa_1(\mathbf{x}_p)) \rangle \leq -\rho_1(|\mathbf{x}_p|_{\mathcal{A}}) \forall \mathbf{x}_p \in \mathbb{R}^n$.

To provide GAS, the supervisor is designed as follows. Consider a constant c_0 such that $L_{W_0}(c_0) := \{\mathbf{x}_p \in \mathbb{R}^{n_p} : W_0(\mathbf{x}_p) \leq c_0\} \subset \mathcal{U}_0$. Let the jump set of the global controller $D_{S_1} \subset L_{w_0}(c_0)$ be a compact set containing the origin on its interior. Take the flow set of the global controller $C_{S_1} = \mathbb{R}^n / D_{S_1}$, the flow set of the local controller $C_{S_0} = \mathcal{U}_0$ and the jump set of local controller $D_{S_0} = \mathbb{R}^{n_p} / \mathcal{U}_0$.

Theorem 5.5.1. Take the supervisor of the form eq. 5.31 defined by the flow and jump

5.5. Hybrid supervisor design

sets and by dynamics:

$$C := \{(z, \mathbf{x}_p) : z \in \{0, 1\}, \mathbf{x}_p \in C_{S_z}\}, D_s := \{(z, \mathbf{x}_p) : z \in \{0, 1\}, \mathbf{x}_p \in D_{S_z}\}$$

$$\mathcal{H}_s : \begin{cases} \dot{z} = 0 \\ z^+ = 1 - z. \end{cases} \quad (5.32)$$

Proof 5.5.1.1. See Theorem 3.18 and Proposition 3.30 in [Goebel et al. \(2012\)](#).

If Assumption 5.5.1 is satisfied, the supervisor \mathcal{H}_s makes set \mathcal{A}_p globally pre-asymptotically stable (see the definition of GpreAS in Section 2.6)

Before addressing how Assumption 5.5.1 can be satisfied, we first need to design the supervisor so that switching occurs at most once for every initial condition. This can be ensured by an appropriate choice of the flow and jump sets, C_{S_z} and D_{S_z} , for $z = 0, 1$, as follows. Set C_{S_1} is chosen to be the entire state space since the nonlinear controller κ_1 is globally stable. Set C_{S_0} is defined as the region of stability of the linear controller κ_0 which, in this work, has been estimated via numerical simulations. Define the jump set $D_{S_1} = \{\mathbf{x}_r : \left\| [\mathbf{q}_e^T \ \boldsymbol{\omega}^T]^T \right\|_2 \leq \gamma_h \cdot \tau_{d,max} + \rho\}$. For an arbitrarily small ρ , it was shown previously that there exist ε^* s.t the spacecraft driven by the controller κ_1 will eventually reach this region for all $\varepsilon \in (0, \varepsilon^*)$. The jump set D_{S_0} must contain D_{S_1} and can be selected as large as the region of stability of the linear controller C_{S_0} . The difference between D_{S_0} and D_{S_1} determines the hysteresis region. To guarantee that the disturbances will not drive the system to a switching when the linear controller active, D_{S_0} must contain the region defined by $\|\mathcal{F}_{yw}\|_\infty \cdot \tau_{d,max}$.

To prove that Assumption 5.5.1 is satisfied, assume no disturbances affect the system. For the local controller, the existence of Lyapunov function W_0 is guaranteed by the stability condition on the characteristics multipliers of the monodromy matrix, see Section 2.5. On the other hand, W_1 is simply equal to the Lyapunov function defined in Theorem 5.4.3. Since both Lyapunov functions are bounded by constants multiplied by a square of the state norm, common bounds k_1, k_2 can always be found such that $k_1 \|\mathbf{x}_p\|^2 \leq W_i(\mathbf{x}) \leq k_2 \|\mathbf{x}_p\|^2, \forall \mathbf{x} \in \mathbb{R}^n$ with $k_1, k_2 > 0$. To show that all the maximal solutions of the hybrid closed loop system \mathcal{H}_{cl} are complete, we notice that the supervisor defined by Theorem 5.5.1 guarantees that every maximal solution ends up in C_{S_0} and no maximal solution starting in C_{S_0} ends up in \mathbb{R}^n/C_{S_0} . The closed loop system with $z = 0$ is locally (asymptotically) stable with unbounded $\text{dom } \mathbf{x}_p$, flowing in between jumps of

ν . It follows that every maximal solution is complete.

Robustness is provided for any $\|\boldsymbol{\tau}_d\|_\infty \leq \tau_{d,max}$ and any $\boldsymbol{x}_p(0, 0)$ since:

- The global controller guarantees practical global stability with region of attraction $D_{S_1} \subset L_{w_0}(c_1)$.
- The local controller guarantees stability over a region $L_{w_0}(c_0)$, with $L_{w_0}(c_1) \subset L_{w_0}(c_0)$.
- All trajectories starting inside $L_{w_0}(c_1)$ are ensured to remain inside \mathcal{U}_0 .

In practice, thanks to the hysteresis region the system will stabilize within maximum two jumps. By design, trajectories starting in D_{S_1} cannot reach D_{S_0} in presence of bounded disturbances and Proposition 1 is thus satisfied.

5.6 Simulations of hybrid magnetic attitude control law

To address the performance of the magnetic hybrid controller, a Matlab-based simulation environment was developed. Attitude and orbit dynamics of a spacecraft traveling on a nearly polar, circular low Earth orbit, are modeled as in [Invernizzi and Lovera \(2019\)](#) and [Rodríguez-Vazquez et al. \(2015\)](#).

Main spacecraft, orbit and disturbances properties are summarized in Table 5.1. The total disturbance $\boldsymbol{\tau}_d$ acting on the spacecraft is the sum of the torques due to gravity gradient, aerodynamic drag, residual magnetic dipole and solar radiation pressure, which have been computed according to the models described in Section 2.7.

The spacecraft inertia properties are known, the gravity gradient torque magnitude is estimated by Eq. 2.37 and is $\approx 1.25 \cdot 10^{-6} Nm$. The residual magnetic dipole, induced mainly by the internal current loops, is expected to be of the order of $\boldsymbol{m}_{res} = m_{tot} \cdot 10^{-3} Am^2/kg$ ([Cortiella et al., 2016](#)). As the maximum intensity of the earth magnetic field is $\boldsymbol{b}_{mean} = [0.0734 \ 0.2107 \ 0.2145]^T \cdot 10^{-4} T$, following Eq. 2.39 the magnitude of the disturbance torque can be estimated by $\|\boldsymbol{\tau}_{res}\|_\infty = 1.38 \cdot 10^{-6} Nm$. Relatively high, it could become dominating disturbance at nominal conditions; however, it is matched by the control input and hence can be compensated almost perfectly.

It is assumed that the distance of the geometric center to the gravity center does not exceed $\boldsymbol{c}_{aero}/\boldsymbol{c}_{srp} \leq 0.1m$, a valid assumption for the considered class of satellites ([Cortiella et al., 2016](#)). The aerodynamic properties influence the stability properties of the satellite, and could be the very limiting factor for underactuated control design ([Sutherland](#)

et al., 2017). In the following, the effects of different aerodynamic designs of the spacecraft will be studied by means of Monte-Carlo simulations. The maximum aerodynamic torque can be computed by Eq. 2.43: the air density at solar maximum is expected to be $\rho = 1 \cdot 10^{-12} \text{kg/m}^3$ (Montenbruck et al., 2002; Wertz, 1978). Similarly, maximum solar radiation torque is computed by Eq. 2.45: it has almost negligible effect.

The maximum control torque depends on the on-board magnetorquers: it is assumed a maximum dipole of 2.5 Am^2 . The magnitude of the maximum control torque is therefore $\|\mathbf{u}\|_{max} \approx 8 \cdot 10^{-5} \text{ Nm}$. The matched disturbance is one order of magnitude smaller, and does not affect static error. The unmatched disturbance effect can be estimated by means of the analysis done in the previous sections.

The magnetic field along the orbit is computed through the IGRF model. Angular rates, attitude angles and geomagnetic field data fed to the controller are corrupted by zero-mean white noise having standard deviations respectively equal to $0.01^\circ/\text{s}$, 0.1° deg and 6 nT . The sampling time is set to one second. Inertia moments uncertainty of 1% has also been simulated. Note that very conservative assumptions have been adopted in modelling the disturbances, leading to high magnitudes of the unmatched torques, i.e. the aerodynamic and solar radiation pressure ones.

The gain matrix K for the local controller κ_0 was computed following the procedure described in Section 5.3, yielding to:

$$K = \begin{bmatrix} -0.183 & 0.002 & 0.004 & -22.24 & 0.183 & 0.473 \\ 0.004 & -0.019 & 0.182 & 0.314 & -1.592 & 15.383 \\ -0.002 & -0.182 & -0.019 & -0.187 & -17.911 & -1.85 \end{bmatrix}. \quad (5.33)$$

Parameters used for the nonlinear controller κ_1 are:

$$\varepsilon = 0.001; k_p = 5; k_d = 10; \delta = 0.1; \quad (5.34)$$

which, according to Eq. 5.27, lead to $\gamma_h \cdot \|\boldsymbol{\tau}_d\|_\infty = 0.351$ for $c_\gamma = 0, \rho = 0$. We chose $D_{S_1} = \mathbf{x}_p : \|\mathbf{x}_{cr}\| \leq 0.4$. This bound guarantee the local region can be reached in finite time. The rationale of this choice is twofold: a low value provides a large hysteresis region and stability of the linear controller. It was verified through simulations that local controller attraction region \mathcal{U}_0 is larger than the chosen set D_{S_1} .

Table 5.1: Simulation parameters

Spacecraft and orbit properties	
Inertia matrix	$J = \text{diag}([1.28 \ 1.12 \ 0.57]) \text{ kgm}^2$
Orbit inclination	88 degree
Orbit height	$\approx 600 \text{ km}$
Maximum control dipole	2.5 Am^2
Onboard residual dipole	0.1 Am^2
Magnitude of centre of pressure offset	0.1 m

Disturbances parameters	
Disturbance type	Maximum norm
Gravity gradient	$1.25 \cdot 10^{-6} \text{ Nm}$
Residual magnetic torque	$2.38 \cdot 10^{-6} \text{ Nm}$
Aerodynamic drag torque	$1.65 \cdot 10^{-6} \text{ Nm}$
Solar radiation pressure torque	$8.51 \cdot 10^{-7} \text{ Nm}$
Total disturbance	$6.13 \cdot 10^{-6} \text{ Nm}$

Set D_{S_0} must be larger than $\mathcal{U}_0 = \mathbf{x}_p : \|\mathbf{x}_r\| \leq \|\mathcal{F}_{yw}\|_\infty \cdot \|\boldsymbol{\tau}_d\|_\infty = 0.514$. Starting from this assumption, it was found through the simulations that the linear controller performs better than the nonlinear one in the following region $\mathbf{x}_p : \|\mathbf{x}_r\| \leq 1$, which is chosen as the jump set D_{S_0} . In Fig. 5.3 (a), the attitude response of the hybrid controller for the disturbance-free case is shown, with initial angular speed $\boldsymbol{\omega}(0) = (0.1 \ 0.1 \ 0.1) \text{ rad/s}$. As expected, asymptotic stability is achieved in the absence of disturbances. In Fig. 5.3 (b), the norm of the reduced state is shown. When the state norm threshold of 0.4 (dash-dot line) is crossed, the supervisor switches to controller κ_0 .

Fig. 5.4 depicts the attitude of the system driven by the supervising controller in presence of disturbances, starting from the same initial conditions. In this case, the hybrid controller maintains the roll-pitch-yaw error angles below $\approx 25^\circ$. As expected, the switching time is almost unaffected, as it mainly depends on the initial angular rate.

In Fig. 5.5 a comparison of the pure nonlinear (solid line) and supervised (dashed

5.6. Simulations of hybrid magnetic attitude control law

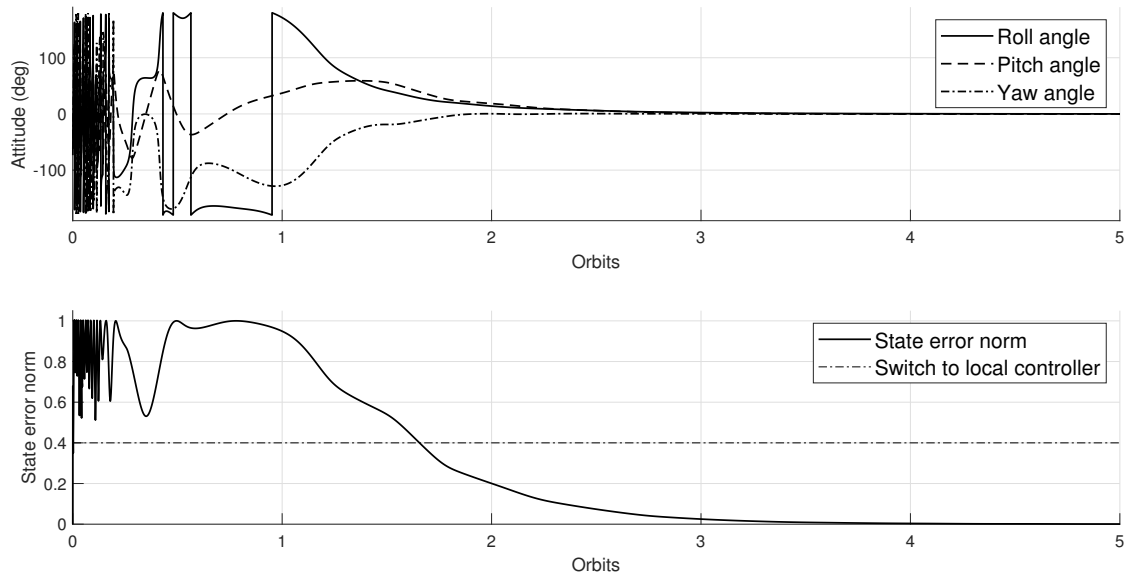


Figure 5.3: Disturbance-free case (a) attitude (b) reduced state norm

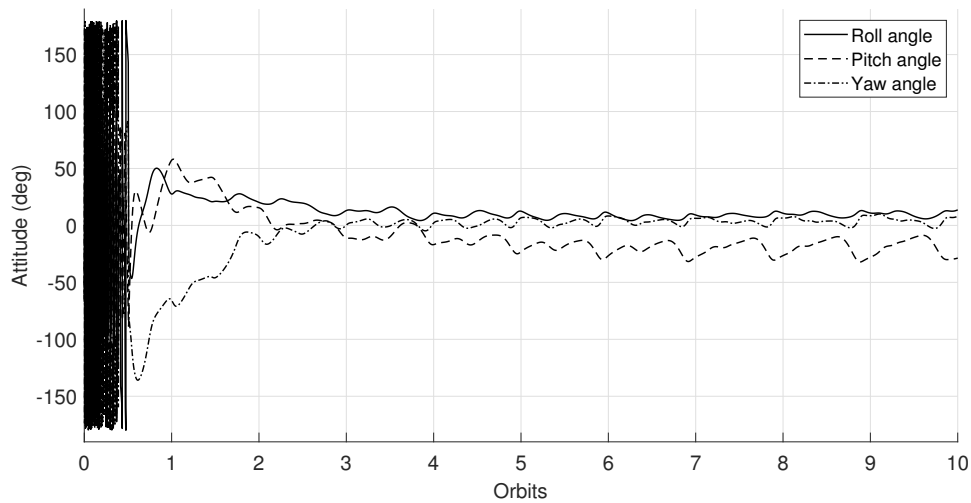


Figure 5.4: Attitude evolution of the spacecraft in case of disturbances

line) controllers is shown. The trajectory is the same until D_{S_1} boundary (dash-dot line) is reached, when the hybrid controller switches from κ_1 to κ_0 . After switching, the local controller outperforms the pure non-linear one in maintaining the state closer to the origin, thereby confirming the rationale behind the use of united controllers.

The time history of the control magnetic dipole along the same simulation, computed by the Eq. 2.28, is shown in Fig. 5.6. In the first part all the available torque is em-

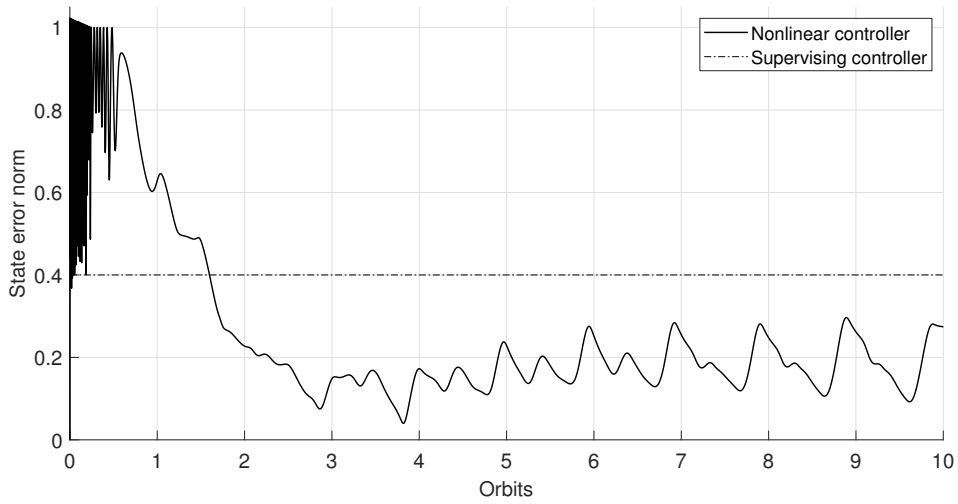


Figure 5.5: Comparison of reduced state norm of the spacecraft in case of disturbances for different controllers

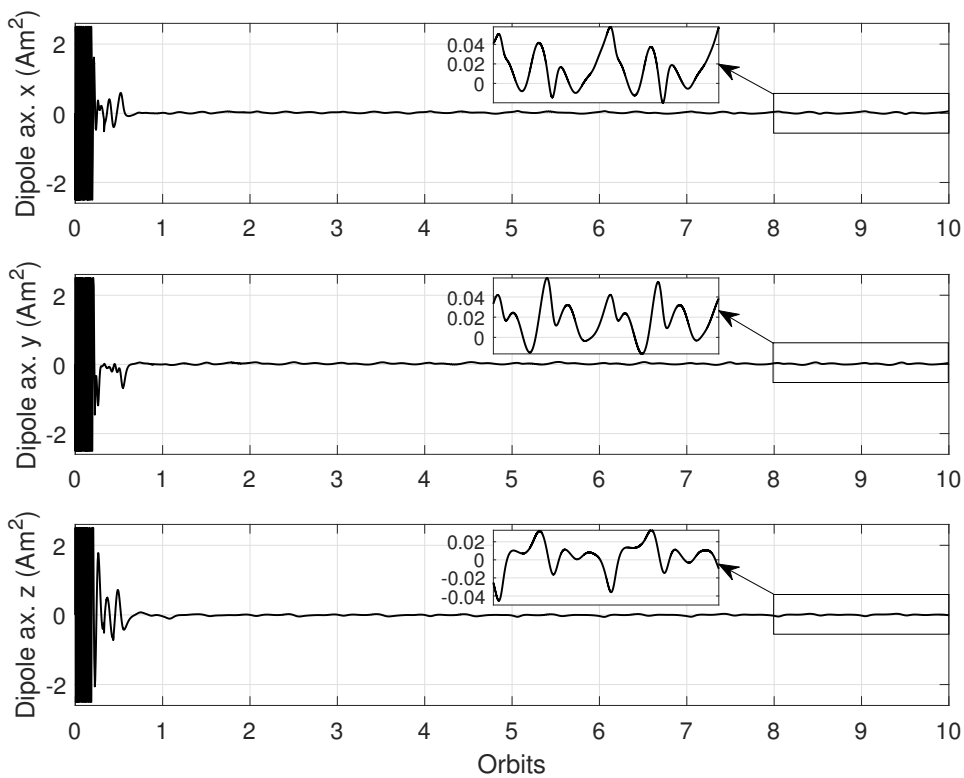


Figure 5.6: Control dipole moments

ployed by the nonlinear controller to dissipate the spacecraft kinetic energy, saturating the dipole. This behaviour guarantees the fastest possible angular speed damping. The transient is followed by a steady-state, where the linear controller is active. In steady-state, magnetorquers are maintained far from saturation: this outcome is to be expected, since the control effort of κ_0 is limited by design within the definition of the performance index, Eq. 5.5.

To investigate how the system performance is affected by disturbances, a sensitivity analysis was done by analysing the system trajectories with respect to random variations in the direction of the aerodynamic and solar radiation pressure centers, magnetic dipole and initial angular speed. The maximum disturbance norm and control gains are kept constant throughout the simulations. Results of a series of 1000 Monte Carlo runs, expressed in terms of maximum attitude error angle after the transient, are shown in Fig. 5.7 with random aerodynamic center and solar pressure center by the histogram distribution of such angle. For all simulations, only one switching from κ_1 to κ_0 occurs, as required by the design of the supervisor.

Overall, the performance of the hybrid controller proved to comply with the design objectives: for all simulations, pointing errors remain bounded, and the state norm remains inside region \mathcal{U}_0 , according to the bounds predicted by the H_∞ norm of the input/output operator for κ_0 . When compared to existing solutions for the purely magnetic spacecraft attitude control, the hybrid controller developed herein compares favourably. It leads to pointing errors in line with those of existing locally optimal controllers (Ovchinnikov and Roldugin, 2019; Chasset et al., 2013), which are in turn better than those of typical nonlinear controllers (Invernizzi and Lovera, 2019). As far as convergence time is concerned, it largely depends on the magnitude of the initial angular speed. In our simulations, convergence is achieved in about one orbit, soon after the switching from κ_1 to κ_0 occurs. Note that, in existing implementations, local magnetic controllers are usually enabled following a detumbling phase (Silani and Lovera, 2005), which therefore assumes a role similar to the one played by κ_1 in our hybrid controller. In such case, however, the angular velocity bound is set heuristically.

5.7 Discussion

Robust and global three-axis attitude control of inertial-pointing satellite by means of solely magnetic actuation is proposed. The control goal is achieved thanks to a uniting

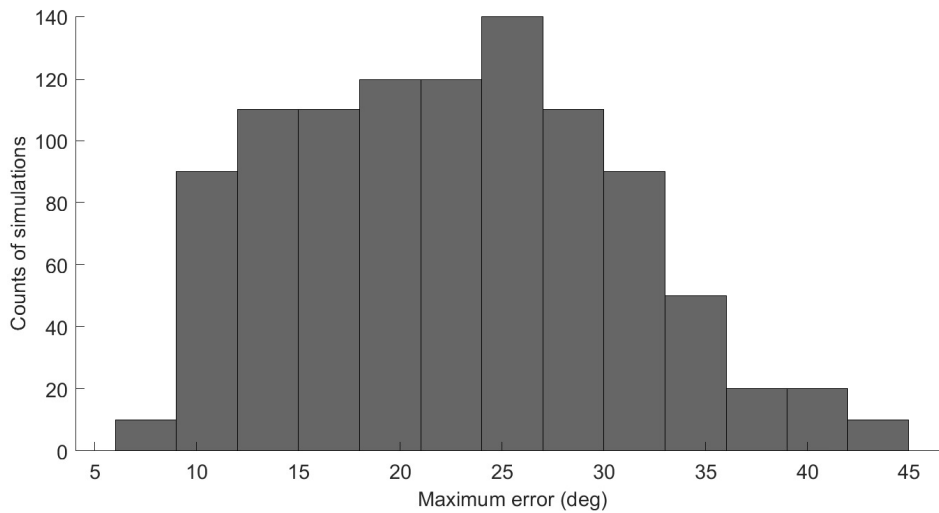


Figure 5.7: Pointing errors with random aerodynamic center and solar pressure center

control design: a local optimal and or global robust controllers are implemented together with a hybrid supervisor. Hybrid framework aims at overcoming topological obstructions and time dependence.

Controllers domains are designed according to appropriate input-output functions and to the magnitude of disturbances affecting the system. Averaged control theory is applied to the nonlinear controller to find Input-to-State gain. H-inf norm of the linear controller provides respective performance index for local control law.

Numerical simulations results shows that robustness and performance requirements are satisfied. The hybrid controller brings remarkable advantages: GAS is provided, along with a systematic approach for solving the uniting controllers problem, analytical tools for robustness analysis and guaranteed performance for a known disturbance level.

6

Conclusions and Perspectives

The rising popularity of the small- and nano-satellites poses new challenges in front of the scientific community. The low-cost nanosatellites development philosophy may undermine their reliability. The reliability of the ADCS, an inherently complex and often underdeveloped subsystem in the considered satellites class, was addressed in this work.

In the first part of the manuscript, design of a dynamic testbed for ADCS verification is described. The development was done with CubeSat form-factor in mind. However, the facility is quite flexible in terms of ADCS applications testability, as it can host nanosatellite mock-up of different size and control modes (such as zero momentum, momentum bias, spinning bus), while allowing for variable sunlight and magnetic field intensity.

Budget constraints led the design choices towards a low hardware complexity. These includes, for example, employing a customized LED studio light rather than a COTS Sun simulator, and opting for a simpler monocular vision system, rather than a COTS multi-camera solution. In doing so, the hardware cost of the entire facility was kept within the budget constraints, yet obtaining adequate performances. These were achieved, in turn, by developing:

- a custom designed rotating platforms, with reduced structural deformation, for 1U and 3U CubeSats testing;
- feedback controlled, magnetic field simulator;

- a collimation system for the LED light for sun simulations, whose divergence and spatial uniformity have been experimentally verified;
- a custom monocular vision system for ground truth attitude-generation;
- an automatic balancing system.

A novel balancing procedure was designed and implemented on the testbed. Performance assessment of the automatic mass balancing system has been addressed both by numerical simulations and experimentally. Through the simulations, effects of main sources of measurement noise, system uncertainties, and unmodelled disturbances have been analyzed, allowing to identify the algorithms combination leading to the most effective balancing. This was then implemented on embedded real-time hardware, requiring no actuators other than simple linear stages, and experimentally tested, providing a residual torque of less than $5 \cdot 10^{-5} Nm$.

The experimental subsystems verification results confirm that adequate performance for nanosatellite ADCS ground-based simulators can be reached even with low-cost hardware, with the automatic balancing system being effective in reducing the disturbance torque down to the hardware-dependent limit.

In the second part of the thesis, attitude control by means of solely magnetic actuation is addressed. The control problem is inherently complex: instantaneous underactuation and time variance threaten the stability properties of the closed loop system. At the same time, due to unmatched time-varying disturbances which cannot be compensated, low pointing errors are difficult to achieve.

To solve this problem, a novel control law was developed: by means of a hybrid supervisor, uniting of an optimal local regulator and a robust global control law was performed. Global attitude stability is ensured, while achieving local optimality and robustness against bounded disturbances, both matched and unmatched by the control action, and measurement noise. Global asymptotic stability was proved thanks to the properties of the designed supervising algorithm and then verified through Monte Carlo simulations.

Starting from the research work described in this thesis, possible future developments are identified. Several improvements of the facility are ongoing:

- integration of higher-end sensors, as a first step towards further reduction of the residual disturbance torque;

- further structural optimization of the rotational support for reducing its weight without impacting the flexural rigidity;
- development and implementation of new control laws for planar balancing to enhance the robustness against system uncertainties;
- development of simulator software and hardware, for attitude control and determination algorithms HIL testing.

As the described facility is now fully commissioned, the proposed hybrid attitude control law can be implemented on-board of the simulator and experimentally tested. Further analysis on the proposed algorithm is ongoing, in particular the selection of the switching bounds can be done in an optimal way by analyzing the input-output functions.

Since the proposed approach shows the great potential that hybrid control theory has in solving challenging problems, such as the one of the underactuated spacecraft attitude control, it can be employed to design attitude control laws based on different actuators. Indeed, supervised control allows combining multiple controllers, thus exploiting their respective benefits, and provides tools for handling efficiently the discrete dynamics which arises from such a combination. In addition, the developed facility makes possible to test new algorithms experimentally, thus providing better understanding of their performance and capabilities.

Bibliography

- ASTM. ASTM E927 - 10 : Specification for Solar Simulation for Photovoltaic Testing-tle, 2010. URL <https://www.astm.org/DATABASE.CART/HISTORICAL/E927-10.htm>.
- G. Avanzini and F. Giuliatti. Magnetic detumbling of a rigid spacecraft. *Journal of Guidance, Control, and Dynamics*, 35(4):1326–1334, 2012. ISSN 15333884. doi: 10.2514/1.53074.
- G. Avanzini, E. L. De Angelis, and F. Giuliatti. Spin-axis pointing of a magnetically actuated spacecraft. *Acta Astronautica*, 94(1):493–501, 2014. ISSN 00945765. doi: 10.1016/j.actaastro.2012.10.035. URL <http://dx.doi.org/10.1016/j.actaastro.2012.10.035>.
- B. Bachofer and L. Seaman. One-arc-second simulator for orbiting astronomical observatory. American Institute of Aeronautics and Astronautics (AIAA), jun 1964. doi: 10.2514/6.1964-205. URL <https://arc.aiaa.org/doi/abs/10.2514/6.1964-205>.
- A. Bahu and D. Modenini. Automatic mass balancing system for a dynamic CubeSat attitude simulator: development and experimental validation. *CEAS Space Journal*, (0123456789), 2020. ISSN 18682510. doi: 10.1007/s12567-020-00309-5.
- A. Bahu and D. Modenini. Hybrid controller for global, robust, attitude stabilization of a magnetically actuated spacecraft. *CEAS Space Journal*, 2021. doi: 10.1007/s12567-020-00340-6.
- S. Bandyopadhyay, G. P. Subramanian, R. Foust, D. Morgan, S. J. Chung, and F. Y. Hadaegh. A review of impending small satellite formation flying missions. *53rd AIAA Aerospace Sciences Meeting*, (January 2016), 2015. doi: 10.2514/6.2015-1623.
- S. P. Bhat. Controllability of nonlinear time-varying systems: Applications to spacecraft attitude control using magnetic actuation. *IEEE Transactions on Automatic Control*, 50(11):1725–1735, 2005. ISSN 00189286. doi: 10.1109/TAC.2005.858686.

- S. P. Bhat and D. S. Bernstein. A topological obstruction to continuous global stabilization of rotational motion and the unwinding phenomenon. *Systems and Control Letters*, 39(1):63–70, jan 2000. ISSN 01676911. doi: 10.1016/S0167-6911(99)00090-0.
- C. B. Bok, A. Comeau, A. Dolgoplov, T. Halt, C. Juang, and P. Smith. SmallSats by the Numbers. Technical report, Bryce and Space Technology, 2020. URL <https://brycetech.com/reports/report-documents/Bryce{ }Smallsats{ }2020.pdf>.
- J. Bouwmeester and J. Guo. Survey of worldwide pico- and nanosatellite missions, distributions and subsystem technology. *Acta Astronautica*, 67(7-8):854–862, 2010. ISSN 00945765. doi: 10.1016/j.actaastro.2010.06.004. URL <http://dx.doi.org/10.1016/j.actaastro.2010.06.004>.
- F. Celani. Acta Astronautica Robust three-axis attitude stabilization for inertial pointing spacecraft using magnetorquers. *Acta Astronautica*, 107:87–96, 2015. ISSN 0094-5765. doi: 10.1016/j.actaastro.2014.11.027. URL <http://dx.doi.org/10.1016/j.actaastro.2014.11.027>.
- G. Cervettini, H. Park, D. Y. Lee, and S. Pastorelli. Development and Experimentation of a CubeSat Magnetic Attitude Control System Testbed. *IEEE Transactions on Aerospace and Electronic Systems*, 2020. doi: 10.1109/TAES.2020.3040032.
- C. Chasset, R. Noteborn, P. Bodin, R. Larsson, and B. Jakobsson. 3-Axis magnetic control: Flight results of the TANGO satellite in the PRISMA mission. *CEAS Space Journal*, 5(1-2):1–17, 2013. ISSN 18682502. doi: 10.1007/s12567-013-0034-9.
- N. A. Chaturvedi, F. Bacconi, D. Bernstein, N. H. Mcclamroch, and A. Arbor. Stabilization of a 3D Axially Symmetric Rigid Pendulum. pages 5287–5292, 2005.
- S. Chesi, Q. Gong, V. Pellegrini, R. Cristi, and M. Romano Prof. Automatic mass balancing of a spacecraft three-axis simulator: Analysis and experimentation. *Journal of Guidance, Control, and Dynamics*, 37(1):197–206, 2014. ISSN 15333884. doi: 10.2514/1.60380.
- S. Chesi, O. Perez, and M. Romano. A Dynamic Hardware-in-the-Loop Three-Axis Simulator of Nanosatellite Dimensions. *Journal of Small Satellites*, 4(1):315–328, 2015.

- M. Cho, H. Masui, T. Hatamura, K. Date, S. Horii, and S. Obata. Overview of Nano-satellite Environmental Tests Standardization Project : Test Campaign and Standard Draft. In *Proceedings of the 26th Small Satellites Conference, Technical Session VII: Growing the Community*, 2012. ISBN 0362688818.
- A. Cortiella, D. Vidal, J. Jané, E. Juan, R. Olivé, A. Amézaga, J. F. Munoz, P. V. H. Carreno-Luengo, and A. Camps. 3CAT-2: Attitude determination and control system for a GNSS-R earth observation 6U cubesat mission. *European Journal of Remote Sensing*, 49:759–776, 2016. ISSN 22797254. doi: 10.5721/EuJRS20164940.
- N. H. Crisp, K. Smith, and P. Hollingsworth. Launch and deployment of distributed small satellite systems. *Acta Astronautica*, 114:65–78, 2015. ISSN 00945765. doi: 10.1016/j.actaastro.2015.04.015.
- E. U. S. N. A. Culton, J. T. U. S. N. A. King, and W. U. S. N. A. Paige. Design and Development of an Unrestricted Satellite Motion Simulator. *31st Annual AIAA/USU Conference on Small Satellites*, pages SSC17–V–03, 2017. URL <https://digitalcommons.usu.edu/cgi/viewcontent.cgi?article=3553&context=smallsat>{%}0Ahttps://digitalcommons.usu.edu/smallsat/2017/all2017/22/.
- R. C. Da Silva, I. S. K. Ishioka, C. Cappelletti, S. Battistini, and R. A. Borges. Helmholtz Cage Design and Validation for Nanosatellites HWIL Testing. *IEEE Transactions on Aerospace and Electronic Systems*, 55(6):3050–3061, 2019. ISSN 15579603. doi: 10.1109/TAES.2019.2898309.
- F. Davoli, C. Kourogorgas, M. Marchese, A. Panagopoulos, and F. Patrone. Small satellites and CubeSats: Survey of structures, architectures, and protocols. *International Journal of Satellite Communications and Networking*, 37(4):343–359, jul 2019. ISSN 1542-0973. doi: 10.1002/sat.1277. URL <https://onlinelibrary.wiley.com/doi/abs/10.1002/sat.1277>.
- E. L. De Angelis, F. Giuliatti, A. H. De Ruiter, and G. Avanzini. Spacecraft attitude control using magnetic and mechanical actuation. *Journal of Guidance, Control, and Dynamics*, 39(3):564–573, 2016. ISSN 15333884. doi: 10.2514/1.G000957.
- C. de Ruiter, Anton H.J.; Damaren and J. R. Forbes. *Spacecraft Dynamics and Control*. 2013. ISBN 9781118342367. doi: 10.1017/cbo9780511815652.

- M. A. Desouky and O. Abdelkhalik. A new variant of the B-dot control for spacecraft magnetic detumbling. *Acta Astronautica*, 171(November 2019):14–22, 2020. ISSN 00945765. doi: 10.1016/j.actaastro.2020.02.030. URL <https://doi.org/10.1016/j.actaastro.2020.02.030>.
- P. Domain. CubeSat Design Specification Rev. 14. Technical report, 2009.
- H. Fornoff. Air bearing platform, T50-2 Final report, 1967.
- I. Gavrilovich. *Development of a robotic system for CubeSat Attitude Determination and Control System ground tests*. Phd thesis, Université de Montpellier, 2018. URL <https://tel.archives-ouvertes.fr/tel-01816985>.
- I. Gavrilovich, S. Krut, M. Gouttefarde, F. Pierrot, and L. Dusseau. Robotic test bench for CubeSat ground testing: Concept and satellite dynamic parameter identification. *IEEE International Conference on Intelligent Robots and Systems*, 2015-Decem:5447–5453, 2015. ISSN 21530866. doi: 10.1109/IROS.2015.7354148.
- D. Gerhardt, M. Bisgaard, L. Alminde, R. Walker, M. A. Fernandez, A. Latiri, and J.-L. Issler. GOMX-3: Mission Results from the Inaugural ESA In-Orbit Demonstration CubeSat. In *In Proceedings of the 30th Annual AIAA/USU Conference on Small Satellites*, Logan, UT, USA, aug 2016.
- R. Goebel, R. R. Sanfelice, and A. R. Teel. *Hybrid dynamical systems: Modeling, stability, and robustness*. Princeton University Press, mar 2012. ISBN 9780691153896.
- A. Gregorio and F. Alimenti. CubeSats for Future Science and Internet of Space: Challenges and Opportunities. *2018 25th IEEE International Conference on Electronics Circuits and Systems, ICECS 2018*, pages 169–172, 2019. doi: 10.1109/ICECS.2018.8617947.
- O. Han, D. Kienholz, P. Janzen, and S. Kidney. Gravity-Off-loading System for Large-Displacement Ground Testing of Spacecraft Mechanisms. *Proceedings of the 40th Aerospace Mechanisms Symposium*, page 14, 2010. URL <https://ntrs.nasa.gov/search.jsp?R=20100021948>.
- J. Hu and H. Zhang. On input-to-state stability of rigid-body attitude control with quaternion representation. *International Journal of Robust and Nonlinear Control*, 28(4): 1334–1349, 2018. ISSN 10991239. doi: 10.1002/rnc.3957.

- P. C. . Hughes. *Spacecraft Attitude Dynamics*. 1986. ISBN 0486439259. doi: 10.1016/b978-0-08-102133-0.00012-x.
- D. Invernizzi and M. Lovera. Attitude stabilization of inertial pointing spacecraft using magnetic actuators. In *IFAC-PapersOnLine*, volume 52, pages 442–447. Elsevier Ltd, 2019. doi: 10.1016/j.ifacol.2019.11.283. URL <https://doi.org/10.1016/j.ifacol.2019.11.283>.
- H. W. Jones. The Recent Large Reduction in Space Launch Cost. *48th International Conference on Environmental Systems*, (July 2018):81, 2018. URL <https://ttu-ir.tdl.org/handle/2346/74082>.
- N. Jovanovic and J. M. Pearce. Design and Testing of a Low-Cost , Open Source , 3-D Printed Air-Bearing-Based Attitude Simulator for CubeSat Satellites. *Journal of Small Satellites*, 8(2):859–880, 2019.
- T. Kato, A. Heidecker, M. Dumke, and S. Theil. Three-Axis Disturbance-Free Attitude Control Experiment Platform : FACE. *Transactions of the Japan Society for Aeronautical and Space Sciences*, 12(ists29):Td_1–Td_6, 2014. ISSN 1884-0485. doi: 10.2322/tastj.12.td_1.
- H. K. Khalil. *Nonlinear Systems*, 1996.
- J. J. Kim and B. N. Agrawal. Automatic mass balancing of air-bearing-based three-axis rotational spacecraft simulator. *Journal of Guidance, Control, and Dynamics*, 32(3): 1005–1017, 2009. ISSN 15333884. doi: 10.2514/1.34437.
- A. Kramer, P. Bangert, and K. Schilling. UWE-4: First electric propulsion on a 1U cubesat-in-orbit experiments and characterization. *Aerospace*, 7(7):98, jul 2020. ISSN 22264310. doi: 10.3390/AEROSPACE7070098. URL www.mdpi.com/journal/aerospace.
- E. Kulu. Nanosats Database, 2020. URL <https://www.nanosats.eu>.
- T. H. Kwan, K. M. B. Lee, J. Yan, and X. Wu. An air bearing table for satellite attitude control simulation. *Proceedings of the 2015 10th IEEE Conference on Industrial Electronics and Applications, ICIEA 2015*, pages 1420–1425, 2015. doi: 10.1109/ICIEA.2015.7334330.

- M. Langer and J. Bouwmeester. Reliability of CubeSats – Statistical Data , Developers ’ Beliefs and the Way Forward. In *Proceedings of the AIAA/USU Conference on Small Satellites*, pages 1–12, 2016.
- D. Y. Lee, H. Park, M. Romano, and J. Cutler. Development and experimental validation of a multi-algorithmic hybrid attitude determination and control system for a small satellite. *Aerospace Science and Technology*, 78:494–509, 2018. ISSN 12709638. doi: 10.1016/j.ast.2018.04.040. URL <https://doi.org/10.1016/j.ast.2018.04.040>.
- D. Liberzon. *Systems and control: Foundations & Applications Switching in systems and control*, 2003.
- M. Lovera. Periodic H-inf Attitude Control for Satellites with Magnetic Actuators. *IFAC Proceedings Volumes*, 33(14):631–636, 2000. ISSN 14746670. doi: 10.1016/s1474-6670(17)36300-0. URL [http://dx.doi.org/10.1016/S1474-6670\(17\)36300-0](http://dx.doi.org/10.1016/S1474-6670(17)36300-0).
- M. Lovera and A. Astolfi. Global magnetic attitude control of spacecraft. *Proceedings of the IEEE Conference on Decision and Control*, 1:267–272, 2004. ISSN 01912216. doi: 10.1109/cdc.2004.1428641.
- M. Lovera, E. De Marchi, and S. Bittanti. Periodic attitude control techniques for small satellites with magnetic actuators. *IEEE Transactions on Control Systems Technology*, 10(1):90–95, 2002. ISSN 10636536. doi: 10.1109/87.974341.
- J. Lygeros, K. H. Johansson, S. N. Simić, J. Zhang, and S. S. Sastry. Dynamical properties of hybrid automata. *IEEE Transactions on Automatic Control*, 48(1):2–17, jan 2003. ISSN 00189286. doi: 10.1109/TAC.2002.806650.
- S. Martin. Modern Small Satellites - Changing the Economics of Space. *Proceedings of the IEEE*, 106(3):343–361, 2018.
- C. G. Mayhew, R. G. Sanfelice, and A. R. Teel. Quaternion-based hybrid control for robust global attitude tracking. *IEEE Transactions on Automatic Control*, 56(11):2555–2566, nov 2011. ISSN 00189286. doi: 10.1109/TAC.2011.2108490.
- B. Mero, K. Quillien, M. McRobb, S. Chesi, R. Marshall, A. Gow, C. Clark, M. Anciaux, P. Cardoen, J. D. Keyser, P. Demoulin, D. Fussen, D. Pieroux, and S. Ranvier.

- PICASSO: A State of the Art CubeSat. *Small Satellite Conference*, aug 2015. URL <https://digitalcommons.usu.edu/smallsat/2015/all2015/15>.
- D. Modenini, A. Bahu, G. Curzi, and A. Togni. A dynamic testbed for nanosatellites attitude verification. *Aerospace*, 7(3), 2020. ISSN 22264310. doi: 10.3390/aerospace7030031.
- O. Montenbruck, E. Gill, and F. Lutze. Satellite Orbits: Models, Methods, and Applications. *Applied Mechanics Reviews*, 55(2):B27, 2002. ISSN 00036900. doi: 10.1115/1.1451162.
- Y. K. Nakka, R. C. Foust, E. S. Lupu, D. B. Elliott, I. S. Crowell, S. J. Chung, and F. Y. Hadaegh. A six degree-of-freedom spacecraft dynamics simulator for formation control research. *Advances in the Astronautical Sciences*, 167:3367–3386, 2018. ISSN 00653438.
- D. Nešić and A. R. Teel. Input-to-state stability for nonlinear time-varying systems via averaging. *Mathematics of Control, Signals, and Systems*, 14(3):257–280, 2001. ISSN 09324194. doi: 10.1007/PL00009885.
- M. Y. Ovchinnikov and D. S. Roldugin. Progress in Aerospace Sciences A survey on active magnetic attitude control algorithms for small satellites. *Progress in Aerospace Sciences*, (March):0–1, 2019. ISSN 0376-0421. doi: 10.1016/j.paerosci.2019.05.006. URL <https://doi.org/10.1016/j.paerosci.2019.05.006>.
- H. C. Polat, J. Virgili-Llop, and M. Romano. Survey, Statistical Analysis and Classification of Launched CubeSat Missions with Emphasis on the Attitude Control Method. *JoSS*, 5(3):513–530, 2016. URL www.jossonline.com.
- J. Prado, G. Bisiacchi, L. Reyes, E. Vicente, F. Contreras, M. Mesinas, and A. Juárez. Three-axis air-bearing based platform for small satellite attitude determination and control simulation. *Journal of Applied Research and Technology*, 3(03):222–237, 1998. ISSN 1665-6423. doi: 10.22201/icat.16656423.2005.3.03.563.
- J. Prado-Molina, H. Hernández-Arias, D. Vera-Mendoza, J. A. Reyes-González, and J. Prado-Morales. Frictionless spacecraft simulator with unrestricted three-axis movement for Nanosats. *International Journal of Scientific and Technology Research*, 7(8): 84–95, 2018. ISSN 22778616.

- C. Prieur. Uniting local and global controllers with robustness to vanishing noise. *Mathematics of Control, Signals, and Systems*, 14(2):143–172, 2001. ISSN 09324194. doi: 10.1007/PL00009880.
- M. L. Psiaki. Magnetic torquer attitude control via asymptotic periodic linear quadratic regulation. *AIAA Guidance, Navigation, and Control Conference and Exhibit*, 24(2), 2000. doi: 10.2514/6.2000-4043.
- J. Puig-suari, C. Turner, and R. J. Twiggs. CubeSat: The Development and Launch Support Infrastructure for Eighteen Different Satellite Customers on One Launch. In *15th Annual AIAA/USU Conference on Small Satellites Proceedings*, pages 1–5, 2001. ISBN 6507238651.
- A. L. Rodriguez-Vazquez, M. A. Martin-Prats, and F. Bernelli-Zazzera. Spacecraft magnetic attitude control using approximating sequence riccati equations. *IEEE Transactions on Aerospace and Electronic Systems*, 51(4):3374–3385, 2015. ISSN 00189251. doi: 10.1109/TAES.2015.130478.
- G. Rufino, D. Accardo, M. Grassi, G. Fasano, A. Renga, and U. Tancredi. Real-Time Hardware-in-the-Loop Tests of Star Tracker Algorithms. *International Journal of Aerospace Engineering*, 2013:505720, 2013. ISSN 1687-5966. doi: 10.1155/2013/505720. URL <https://doi.org/10.1155/2013/505720>.
- T. Rybus and K. Seweryn. Planar air-bearing microgravity simulators: Review of applications, existing solutions and design parameters, mar 2016. ISSN 00945765.
- N. Saeed, A. Elzanaty, H. Almorad, H. Dahrouj, T. Y. Al-Naffouri, and M. S. Alouini. CubeSat Communications: Recent Advances and Future Challenges. *IEEE Communications Surveys and Tutorials*, 22(3):1839–1862, 2020. ISSN 1553877X. doi: 10.1109/COMST.2020.2990499.
- R. G. Sanfelice, A. R. Teel, and R. Goebel. Supervising a family of hybrid controllers for robust global asymptotic stabilization. *Proceedings of the IEEE Conference on Decision and Control*, pages 4700–4705, 2008. ISSN 01912216. doi: 10.1109/CDC.2008.4739481.
- K. Saulnier, D. Pérez, R. C. Huang, D. Gallardo, G. Tilton, and R. Bevilacqua. A six-degree-of-freedom hardware-in-the-loop simulator for small spacecraft. *Acta Astro-*

- nautica*, 105(2):444–462, 2014. ISSN 00945765. doi: 10.1016/j.actaastro.2014.10.027. URL <http://dx.doi.org/10.1016/j.actaastro.2014.10.027>.
- H. Schaub and J. L. Junkis. *Analytical Mechanics of Space Systems*. AIAA EDUCATUIN SERIES, Virginia, USA, second edi edition, 2009.
- J. L. Schwartz and C. D. Hall. Comparison of system identification techniques for a spherical air-bearing spacecraft simulator. *Advances in the Astronautical Sciences*, 116:1725–1741, 2004. URL <http://citeseerx.ist.psu.edu/viewdoc/download?doi=10.1.1.103.3175{&}rep=rep1{&}type=pdf>.
- J. L. Schwartz, M. A. Peck, and C. D. Hall. Historical review of spacecraft simulators. *Advances in the Astronautical Sciences*, 114(SUPPL.):405–423, 2003. ISSN 00653438.
- E. Silani and M. Lovera. Magnetic spacecraft attitude control : a survey and some new results. *Control Engineering Practice*, 13:357–371, 2005. doi: 10.1016/j.conengprac.2003.12.017.
- R. C. D. Silva, F. C. Guimarães, J. V. L. D. Loiola, R. A. Borges, S. Battistini, and C. Cappelletti. Tabletop Testbed for Attitude Determination and Control of Nanosatellites. *Journal of Aerospace Engineering*, 32(1):1–10, 2019. ISSN 08931321. doi: 10.1061/(ASCE)AS.1943-5525.0000952.
- G. A. Smith. DYNAMIC SIMULATORS FOR TEST OF SPACE VEHICLE ATTITUDE CONTROL SYSTEMS. In *Proceedings of the Conference on the Role of Simulation in Space Technology*, pages XV– 1–XV–30, 1964.
- A. Sofyal, D. Ph, E. M. Jafarov, D. Ph, and D. Sc. New Sliding Mode Attitude Controller Design Based on Lumped Disturbance Bound Equation. 31(1):1–15, 2018. doi: 10.1061/(ASCE)AS.1943-5525.0000791.
- E. D. Sontag. *Input to State Stability : Basic Concepts 2*. 2014.
- T. Space. Theia Space Webpage, 2020. URL <https://www.theia.eusoc.upm.es/esat/>.
- D. C. Sternberg, C. Pong, N. Filipe, S. Mohan, S. Johnson, and L. Jones-Wilson. Jet propulsion laboratory small satellite dynamics testbed simulation: On-orbit perfor-

- mance model validation. *Journal of Spacecraft and Rockets*, 55(2):322–334, 2018. ISSN 15336794. doi: 10.2514/1.A33806.
- A. Stickler and K. Alfried. An elementary magnetic attitude control system. *Journal of Spacecraft and Rockets*, 13(5):282–287, 1974. doi: 10.2514/6.1974-923.
- R. Sutherland, I. Kolmanovsky, and A. Girard. LQ attitude control of a 2U cubesat by magnetic actuation. *Advances in the Astronautical Sciences*, 160:3845–3864, 2017. ISSN 00653438.
- M. Swartwout. The first one hundred CubeSats : A statistical look. *Journal of Small Satellites*, 2(2):213–233, 2013.
- L. Tavernini. Differential automata and their discrete simulators. *Nonlinear Analysis*, 11(6):665–683, jan 1987. ISSN 0362546X. doi: 10.1016/0362-546X(87)90034-4.
- A. Teel, J. Peuteman, and D. Aeyels. Global asymptotic stability for the averaged implies semi-global practical asymptotic stability for the actual. (January):1458–1463, 1998. doi: 10.1109/cdc.1998.758492.
- D. Thomas, A. Wolosik, and J. Black. CubeSat attitude control simulator design. *AIAA Modeling and Simulation Technologies Conference, 2018*, (209959), 2018. doi: 10.2514/6.2018-1391.
- M. L. Tibbs. *Design and Test of an Attitude Determination and Control System for a 6U CubeSat using AFIT 's CubeSat Testbed*. PhD thesis, Air Force Institute of Technology, 2015.
- S. P. Timoshenko and S. Woinowsky-Krieger. Symmetrical Bending of Circular Plates, 1959.
- S. R. Trout. Use of Helmholtz Coils for Magnetic Measurements. *IEEE Transactions on Magnetics*, 24(4):2108–2111, 1988. ISSN 19410069. doi: 10.1109/20.3411.
- T. Ustrzycki, R. Lee, and H. Chesser. Spherical air bearing attitude control simulator for nanosatellites. *AIAA Modeling and Simulation Technologies Conference 2011*, (August):90–98, 2011. doi: 10.2514/6.2011-6272.
- D. Vallado. *Fundamentals of Astrodynamics and Applications*. 2000.

- A. van der Schaft and H. Schumacher. *An introduction to hybrid dynamical systems*, volume 251 of *Lecture Notes in Control and Information Sciences*. Springer London, London, 2000. ISBN 978-1-85233-233-4. doi: 10.1007/BFb0109998. URL <http://link.springer.com/10.1007/BFb0109998>.
- T. Villela, C. A. Costa, A. M. Brandão, F. T. Bueno, and R. Leonardi. Towards the thousandth CubeSat: A statistical overview. *International Journal of Aerospace Engineering*, 2019, 2019. ISSN 16875974. doi: 10.1155/2019/5063145.
- P. K. Wang, J. Yee, and F. Y. Hadaegh. Experimental study of synchronized rotation of multiple autonomous spacecraft with rule-based controls. *JOURNAL OF GUIDANCE, CONTROL, AND DYNAMICS*, 24(2):352–360, 2001. doi: 10.2514/6.1999-4150.
- N. Werner, J. Řípa, A. Pál, M. Ohno, N. Tarcai, K. Torigoe, K. Tanaka, N. Uchida, L. Mészáros, G. Galgóczi, Y. Fukazawa, T. Mizuno, H. Takahashi, K. Nakazawa, Z. Várhegyi, T. Enoto, H. Odaka, Y. Ichinohe, Z. Frei, and L. Kiss. CAMELOT: Cube-sats Applied for MEasuring and LOCALising Transients - Mission Overview. *arXiv*, jun 2018. URL <http://arxiv.org/abs/1806.03681>.
- J. R. Wertz. *Spacecraft Attitude Determination and Control*. 1978. ISBN 9027709599.
- B. Wie. *Space Vehicle Dynamics and Control*. AIAA EDUCATUIN SERIES, Ames, Iowa, second edi edition, 2008. ISBN 9781563479533.
- M. Wilde, C. Clark, and M. Romano. Historical survey of kinematic and dynamic spacecraft simulators for laboratory experimentation of on-orbit proximity maneuvers. *Progress in Aerospace Sciences*, 110(July):100552, 2019. ISSN 03760421. doi: 10.1016/j.paerosci.2019.100552. URL <https://doi.org/10.1016/j.paerosci.2019.100552>.
- R. Wiśniewski. Linear time-varying approach to satellite attitude control using only electromagnetic actuation. *Journal of Guidance, Control, and Dynamics*, 23(4):640–647, 2000. ISSN 07315090. doi: 10.2514/2.4609.
- A. T. Wolosik. *Advancements in the Design and Development of CubeSat Attitude Determination and Control Testing at the Virginia Tech Space Systems Simulation Laboratory*. PhD thesis, Virginia Polytechnic Institute and State University, 2018.

- Y. H. Wu, Y. Gao, J. W. Lin, R. Raus, S. J. Zhang, and M. Watt. Low-cost, high-performance monocular vision system for air bearing table attitude determination. *Journal of Spacecraft and Rockets*, 51(1):66–75, feb 2014. ISSN 15336794. doi: 10.2514/1.A32465. URL <https://arc.aiaa.org/doi/abs/10.2514/1.A32465>.
- X. Xia. NanoSats/CubeSats ADCS survey. *Chinese Control and Decision Conference*, pages 5151–5158, 2017.
- D. Xiang, Q. Yang, D. Zhu, C. Liu, and S. Cheng. Research on elastic deformation compensation system for three axis air bearing platform. *International Conference on Fluid Power and Mechatronics Research*, pages 431–434, 2015.
- Y.-c. Xie, H. Huang, Y. Hu, and G.-q. Zhang. Applications of advanced control methods in spacecrafts :. *Frontiers of Information Technology & Electric Engineering*, 17(9): 841–861, 2016.
- Z. Xu, N. Qi, and Y. Chen. Parameter estimation of a three-axis spacecraft simulator using recursive least-squares approach with tracking differentiator and Extended Kalman Filter. *Acta Astronautica*, 117:254–262, 2015. ISSN 00945765. doi: 10.1016/j.actaastro.2015.08.010. URL <http://dx.doi.org/10.1016/j.actaastro.2015.08.010>.
- V. A. Yakubovich and V. M. Starzhinskii. *Differential Equations with Periodic Coefficients*, volume 2. Wiley, Jerusalem-London, jan 1975. doi: 10.1002/zamm.19760560516. URL <http://doi.wiley.com/10.1002/zamm.19760560516>.
- Y. Yang. Analytic LQR Design for Spacecraft Control System Based on Quaternion Model. pages 448–453, 2012. doi: 10.1061/(ASCE)AS.1943-5525.0000142.
- Y. Yang. Controllability of spacecraft using only magnetic torques. *IEEE Transactions on Aerospace and Electronic Systems*, 52(2):954–961, 2016. ISSN 00189251. doi: 10.1109/TAES.2015.150520.
- J. Young. Balancing of a Small Satellite Attitude Control Simulator on an Air Bearing. In *Proceedings of the Utah Space Grant Consortium Symposium*, pages 1–7, 1998.

- A. M. Zanchettin and M. Lovera. *H-inf attitude control of magnetically actuated satellites*, volume 44. IFAC, 2011. ISBN 9783902661937. doi: 10.3182/20110828-6-IT-1002.02751. URL <http://dx.doi.org/10.3182/20110828-6-IT-1002.02751>.
- A. M. Zanchettin, A. Calloni, and M. Lovera. Robust magnetic attitude control of satellites. *IEEE/ASME Transactions on Mechatronics*, 18(4):1259–1268, 2013. ISSN 10834435. doi: 10.1109/TMECH.2013.2259843.
- J. Zhou and T. Hagiwara. Finite-dimensional models in evaluating the H2 norm of continuous-time periodic systems. In *IFAC Proceedings Volumes (IFAC PapersOnline)*, volume 16, pages 260–265. IFAC Secretariat, jan 2005. ISBN 008045108X. doi: 10.3182/20050703-6-cz-1902.00614.
- K. Zhou, J. C. Doyle, and K. Glover. *Robust and Optimal Control*. 1999. ISBN 0134565673. URL <http://www.ulb.tu-darmstadt.de/tocs/109091736.pdf>.